Design and fabrication of mid-infrared devices for IoT applications

(Article begins on next page)

31 December 2024

Department of Electrical and Information Engineering

ELECTRICAL AND INFORMATION ENGINEERING
Ph.D. Program

SSD: IINF-02/A –ELECTROMAGNETIC FIELDS

Final Dissertation

Design and Fabrication of Mid-Infrared Devices for IoT Applications

by

Anelli Francesco

Supervisor:

Prof. Francesco Prudenzano

Coordinator of Ph.D. Program:

Prof. Mario Carpentieri

Course n°37, 01/11/2021-31/10/2024

Department of Electrical and Information Engineering

ELECTRICAL AND INFORMATION ENGINEERING
Ph.D. Program

SSD: IINF-02/A –ELECTROMAGNETIC FIELDS

Final Dissertation

_____

Design and Fabrication of Mid-Infrared Devices for IoT Applications

_____

by

Anelli Francesco

_____

Referees: Supervisor:

Prof. Costantino De Angelis   Prof. Francesco Prudenzano

Prof. Gino Sorbello   _____

Coordinator of Ph.D Program:

Prof. Mario Carpentieri

_____

_____

Course n°37, 01/11/2021-31/10/2024

Abstract

The advancement of photonics has transformed the fields of communication and sensing, allowing for outstanding improvements in transmission speed, accuracy, miniaturization, and scalability. This Ph.D. thesis reports the design and fabrication of Mid-InfraRed (Mid-IR) devices tailored for Internet of Things (IoT) applications, focusing on the use of optical fibers based on soft glasses. The research encompasses various optical components, including Bragg gratings inscribed on flat fibers and planar substrates, and optical fiber devices based on stretching and heating fabrication technique such as combiners, couplers, photonic lanterns, long period gratings (LPGs), non-adiabatic tapers, and S-tapers. Additionally, the modelling and design of a Praseodymium-doped laser is explored to enhance Mid-IR light generation.

The initial section of this thesis concentrates on the design, fabrication, and characterization of innovative Bragg gratings. These are wavelength-selective mirrors, essential for the construction of laser cavities. Moreover, they can be used as sensors exploiting the Bragg wavelength shift to measure various physical parameters, such as strain, curvature, and temperature. These results were achieved in collaboration with the University of Southampton (Optoelectronic Research Centre - ORC, UK) and the University of Bristol (School of Civil, Aerospace and Design Engineering, UK).

Considering the increasing interest in the Mid-IR spectral range, the second part of the thesis investigates the design, fabrication, and characterization of

Mid-IR optical fiber components based on soft glasses, mainly operating within the wavelength range from $\lambda = 0.5\ \mu m$ to $\lambda = 5.5\ \mu m$. Optical fiber combiners and couplers are key building blocks in communication and sensing systems, serving for spectral splitting/combining and the increasing of optical power. Photonic lanterns offer an efficient interface between multi-mode and single-mode waveguides, proving beneficial in astrophotonics where *"every photon counts"*. LPGs and tapers enable sensing capabilities in the Mid-IR, spectral range that allows to identify the typical bonds of many molecules. In collaboration with Le Verre Fluoré (Bruz, France), the development of a specialized manufacturing process for soft glasses permitted the fabrication and characterization of these devices.

Finally, Bragg gratings in combination with some of the developed building blocks allow the fabrication of all-in-fiber Mid-IR amplifiers, and lasers systems. In this context, optical fiber lasers, emitting in the Mid-IR wavelengths, can be employed for novel communication and sensing schemes. Therefore, the design and optimization of a Mid-IR continuous wave (CW) laser based on Praseodymium, is reported in the last part of the Ph.D. research work.

Some of the findings from this research have been published in International Journals and presented at National and International Conferences, as detailed in the list at the end of the thesis.

Contents

Introduction

Mid-IR technology is increasingly being recognized for its potential in novel communication schemes and IoT applications. The unique properties of Mid-IR wavelengths, particularly in the wavelength range from $\lambda = 3\ \mu m$ to $\lambda = 5\ \mu m$, make them highly suitable for various communication and sensing applications, exploiting the low-loss atmospheric window [1]. This capability is particularly advantageous in environments with natural or artificial obscurants, as Mid-IR wavelengths can penetrate these barriers effectively, enhancing communication range and reliability. Systems utilizing Mid-IR wavelengths are also characterized by eye-safe operation, high bandwidth, and resistance to jamming, making them ideal for secure communications in hostile environments [1]. The ability to operate effectively in various weather conditions makes Mid-IR an attractive option for IoT devices deployed in diverse environments [2]. Furthermore, in spectroscopy, the Mid-IR wavelength range is garnering considerable scientific attention because most molecules exhibit rotational-vibrational absorption lines within this spectrum, resulting in a distinctive fingerprint [3]. Mid-IR sensors can detect specific gases and pollutants by identifying their unique absorption fingerprints. This capability is essential for environmental monitoring applications, where real-time data on air quality and other parameters are crucial for public health and safety [4]. Mid-IR sensing is useful in other applications, which include imaging, medical diagnosis, and therapy [5], [6], [7]. Consequently, there is a strong demand for the development of Mid-IR components.

Despite the growing interest and potential of Mid-IR technology, its maturity remains inadequate due to the lack of sufficiently developed building blocks required for laser and amplifier systems operating in this spectral range. Components such as couplers, combiners, and splitters, which are fundamental for Mid-IR applications, are still in the early stages of development and require further advancements to enable widespread adoption of this technology [8]. Mid-IR optical fibers are typically produced using chalcogenide glasses, which include elements such as sulfur, selenium, and tellurium, as well as fluoride glasses, such as zirconium fluoride and indium fluoride. These materials are usually employed for their superior transmission properties in the Mid-IR spectrum, contrary to the commonly used silica glass which is not continuously transparent beyond the wavelength $\lambda = 2\,\mu m$ [9]. Chalcogenide optical fibers have been extensively studied due to their broad range of low-attenuation, high nonlinear coefficient, and the potential to create active optical fibers by doping with rare-earth elements [9]. Fluoride optical fibers share some advantages with chalcogenide fibers and offer extremely low Rayleigh scattering and attenuation. Additionally, they can guide light continuously within the transmission windows of $\lambda = 0.3\,\mu m$ to $\lambda = 4.5\,\mu m$ for zirconium fluoride glass and $\lambda = 0.3\,\mu m$ to $\lambda = 5.5\,\mu m$ for indium fluoride glass [10], [11]. Moreover, fluoride optical fibers show lower Fresnel losses than chalcogenide ones at the interface with air or silica [12]. In contrast to silica glass, fluoride glasses present several challenges due to their significantly lower glass transition temperatures, i.e. approximately $T_g = 275°C$ for indium fluoride (InF3) and around $T_g = 265°C$ for zirconium fluoride (ZBLAN). Additionally, these materials have a steep viscosity-temperature profile near the glass transition temperature and are brittle. These characteristics can lead to thermal instabilities during fabrication processes such as splicing and tapering, complicating the production of high-quality optical fibers

devices [13]. Optical fiber devices with Mid-IR transparent glasses, such as combiners and couplers, have been designed, fabricated, and characterized to efficiently combine or split optical signals into and from a single optical fiber. The integration of these devices eliminates the need for bulk optics, facilitating the development of industrial all-fiber lasers operating in the Mid-IR. Moreover, photonic lanterns made from fluoride glass have been fabricated to serve as effective interfaces between multi-mode and single-mode waveguides in the Mid-IR spectral range, where stars are bright. The fabrication procedure has been then optimized to fabricate LPGs via micro-tapering technique. These are fundamental for equalization in amplifiers, suppression of unwanted lasing emissions, and sensing applications. Lastly, all-fiber Mach-Zehnder interferometers have been proposed, based on non-adiabatic taper and S-taper geometries. The research activity on Mid-IR fiber baser components lies in the framework of the European project H2020-ICT-37-2020 "Photonic Accurate and Portable Sensor Systems Exploiting Photo-Acoustic and Photo-Thermal Based Spectroscopy for Real-Time Outdoor Air Pollution Monitoring – PASSEPARTOUT" n. 101016956, with a strict collaboration with the company Le Verre Fluoré (Bruz, France).

Bragg gratings are essential components for the development of laser sources. This Ph.D. research has investigated their operating mechanism, particularly with reference to sensing applications using innovative optical fiber geometries. In other words, the research has explored the employment of Bragg gratings in unconventional optical platforms, such as flat optical fibers and all-glass flexible planar platforms. Flat optical fibers can be manufactured adopting the same technique of standard cylindrical optical fiber, making them more cost-effective compared to traditional planar waveguides. Furthermore, the research focused on developing all-glass flexible photonic platforms, demonstrating the feasibility of fabricating ultra-thin and conformable sensors for bending detection

applications. These novel solutions were developed through a collaborative effort with the University of Southampton (Optoelectronic Research Centre (ORC), UK) and the University of Bristol (School of Civil, Aerospace and Design Engineering, UK).

As already mentioned, Bragg gratings are wavelength-selective structures that can be utilized for multiplexing optical signals or for constructing laser cavities. In this context, a CW laser has been designed and optimized using praseodymium-doped indium fluoride optical fiber to achieve Mid-IR emission at the wavelength $\lambda = 4 \, \mu m$ with a low pump power threshold. This laser has the potential to be applied in optical communication systems and in novel sensing applications.
The obtained results are illustrated by following this organization:

- Chapter 1 introduces the state of the art about fiber Bragg gratings, Mid-IR optical fiber devices, and optical fiber lasers.
- Chapter 2 reports the operating principles, and the theory employed for the designs of: i) Bragg grating sensors, ii) Mid-IR optical fiber components, and iii) Mid-IR optical fiber laser.
- Chapter 3 focuses on Bragg gratings in non-conventional optical platforms. In particular, Section 3.1 describes the design of an embedded microstructured flat optical fiber in composite materials for triaxial stress monitoring; Section 3.2 describes the curvature response of a flexible Bragg grating with off-axis core, including theoretical and experimental details; Section 3.3 describes the design, fabrication and characterization of a few-mode flexible photonic sensor which has the advantage to exploit also ratiometric power (in addition to Bragg wavelength shift), making it possible to achieve

multi-parameter monitoring, inferring, for instance, curvature and temperature simultaneously.

- Chapter 4 describes Mid-IR optical components developed via fused tapering. In particular, Section 4.1 describes the design, fabrication and characterization of an end-pump optical fiber combiner based on indium fluoride optical fibers and capillaries; Section 4.2 describes the design, fabrication and characterization of a 2×2 fluoride optical fiber coupler and reports the excess losses/coupling ratios obtained for symmetrical coupler fabricated with single-mode, few-mode and multimode fibers; Section 4.3 describes the design, fabrication and characterization of an indium fluoride photonic lantern, capable of mode-group selectivity; Section 4.4 describes the design, fabrication and characterization of LPGs inscribed in zirconium fluoride optical fiber via micro-tapering technique; Section 4.5 describes the design, fabrication and characterization of all-fiber-interferometers based on non-adiabatic taper and S-taper geometries.

- Chapter 5 focuses on a Mid-IR CW optical fiber source. In particular, the design of the Mid-IR laser based is based on a Pr^{3+}-doped indium fluoride optical fiber emitting up to $\lambda = 4 \ \mu m$.

1   Optical fiber devices for Mid-IR applications

This chapter introduces the state-of-the-art about all the topics considered in the Ph.D. research activity, i.e. Bragg gratings based on flat optical fibers, and ultra-thin glass substrates for real-time monitoring of strains, Mid-IR optical fiber devices as combiners, couplers, photonic lanterns, sensors, and Mid-IR optical fiber lasers for environmental sensing or novel communication systems.

1.1   Fiber Bragg gratings

Fiber Bragg gratings (FBGs) are structures inscribed within optical fibers that reflect specific wavelengths of light while transmitting others, typically adopting fabrication techniques based on ultraviolet (UV) light [14]. The grating is usually accomplished by inducing periodic refractive index changes in the optical fiber core, creating a dielectric mirror with selective reflectivity [14]. FBGs are extensively used in various applications, such as sensing, multiplexing optical signals, filtering, and for building laser cavities. Their ability to accurately measure physical parameters like temperature and strain makes them relevant in structural health monitoring applications [15]. Indeed, they are characterized by i) high sensitivity, capable of detecting minute changes of the considered physical parameters, ii) lightweight and compact size, iii) multiplexing capability, allowing for the simultaneous monitoring of multiple parameters over long distances, and

iv) durability and resistance, as FBGs are resistant to electromagnetic interference and can function in harsh environments [16]. The Bragg wavelength λ_B is defined as the specific wavelength of light that is reflected by the grating. This wavelength is determined by the periodic structure of the grating. The relationship between the Bragg wavelength, the effective refractive index of the reflected mode n_{eff}, and the grating period Λ can be approximated by the equation $\lambda_B = 2n_{eff}\Lambda$ [17]. This equation shows that the Bragg wavelength is proportional to the effective refractive index guided in the optical fiber and to the grating period of the periodic refractive index change. Therefore, any external factors that change either the refractive index or the grating period will cause a shift in the Bragg wavelength λ_B [18]. In this way, the signal reflected from the grating can undergo a red- or blue-shift, depending on the type of external perturbation. Systems utilizing tunable lasers or broadband light as optical sources and spectrometers or optical spectrum analyzers as detectors can be used as FBGs interrogation schemes [19]. In this way, the Bragg wavelength shift can be precisely detected, allowing for accurate monitoring of strain, temperature and surrounding refractive index variations (if the evanescent field of the interacting modes is sensitive to the environment) [20].

1.1.1 Fiber Bragg gratings embedded in CFRP

FBGs are increasingly employed in structural health monitoring applications, especially surface-mounted or embedded in carbon fiber reinforced polymers (CFRP). CFRP materials are broadly used in aerospace, automotive, and civil engineering because of their high strength-to-weight ratio and superior mechanical properties [21]. However, the challenge is effectively monitoring the structural integrity of these materials, particularly under dynamic loading conditions

[22]. Integrating FBGs into CFRP offers an effective method for real-time strain measurement and damage detection, while having a negligible effect on the structural integrity due to the compact size of the FBGs. Optical fiber sensor technology stands out as a fundamental approach for assessing the internal strain conditions of composite materials like CFRP [23], utilizing a non-destructive sensing method for identifying failures in CFRP like cracks and delamination [24], [25], [26], [27], [28]. It is worthwhile noting that CFRP is generally brittle in the transverse direction and embedded FBG sensors are capable of detecting both static and dynamic strain fields [29], [30].

Regarding multiparameter detection, especially in the context of multiaxial strain monitoring, high birefringent FBGs (such as microstructured, panda, or bow-tie designs) have been suggested as viable options [31], [32]. Birefringence disrupts the circular symmetry of the optical fiber, resulting in two principal transmission axes, referred to as the fast and slow axes. Each polarization of the fundamental mode guided in the optical fiber travels with different velocity, i.e. possesses a different effective refractive index n_{eff}. This phenomenon generates two reflection peaks in the FBG, each characterized by different sensitivities that can be used to measure distinct parameters. Although high birefringent FBGs are suitable for multiparameter detection, they necessitate precise alignment with the composite material structure. Consequently, any errors in the orientation assessment may result in inaccurate estimations of the strain field [33]. Using flat optical fibers, instead of the standard cylindrical optical fibers, for embedding is more suitable, as it helps address issues related to resin-rich regions and fiber orientation within the composite material, due to its peculiar cross-section geometry. A flat optical fiber is primarily composed of a slab waveguide and a surrounding cladding layer [34]. Generally, it allows multimode propagation in two lateral elliptical core areas, referred to as "eyelets," while allowing single-

mode propagation in the central core region, thanks to the presence of a thin, flat core layer [35]. Single-mode waveguides can be fabricated by introducing additional refractive index changes, through direct UV writing (DUW) or femtosecond laser inscription, in both the eyelets and the central core layer of the flat optical fiber [36]. Numerous passive devices have been developed for flat optical fibers, including gratings, interferometers, microfluidic channels, resonators, and splitters [37]. Flat optical fiber sensors can detect damage resulting from impacts, delamination, or debonding by comparing the spectrum before and after such events and employing detection algorithms for pattern recognition [38], [39].

In this thesis, an innovative microstructured flat optical fiber has been designed for multiparameter monitoring [40]. Specifically, this sensor is intended to perform triaxial strain monitoring with high precision. To facilitate the fabrication, an alternative methods have been suggested, based on grooved/sloping cladding region [41], [42].

1.1.2 Fiber Bragg gratings for flexible photonics

Flexible photonics is a promising research field contributing to the development of optical devices and systems that can bend, stretch, or adapt to different shapes and surfaces. This technology is beneficial in scenarios where conventional rigid optical components are not employable. Applications include enabling minimally invasive medical procedures, improving soft robotic systems, and detecting shape changes in composite materials [43], [44]. Various materials, both organic and inorganic, can be utilized to create flexible substrates. The incorporation of materials such as polymers, hydrogels, and other flexible substrates has facilitated the development of lightweight and adaptable photonic devices.

While the focus in flexible photonics has largely been on polymers and other soft materials, all-silica substrates are gaining reputation due to their distinctive properties. Indeed, silica glasses are recognized for their excellent optical performance (e.g. possibility to obtain high core/cladding index contrast), low loss, high thermal stability, and compatibility with FBGs. Recent advancements have produced flexible silica substrates that retain these aspects while also improving bendability. It is worthwhile noting that the maximum curvature of these substrates is influenced by the thickness of the glass and the presence of surface defects, associated with the fabrication process [45]. Various operational principles have been proposed for designing one-dimensional curvature sensors: Bragg gratings in off-axis core [46], eccentric Bragg gratings [47], [48], tilted Bragg gratings [49], [50], long period gratings [51], [52] and in-line interferometers [53], [54], [55]. Multidimensional curvature monitoring is also investigated, and multicore fibers are crucial in this context [56], [57], [58]. To achieve this, three non-aligned cores that are positioned off-axis relative to the curvature have been utilized, with each core containing a Bragg grating. The presence of multiple cores enhances the reliability of the measurements [59]. The shape change monitoring relies on the strain measurements obtained from each Bragg grating.

In this thesis, the curvature effect on the reflection spectrum for an off-axis few-mode core has been investigated and reported for an ultra-thin silica planar Bragg grating [60]. Moreover, a new method has been proposed to monitor the degree of bending using this platform, relying on ratiometric power variation in a few-mode optical waveguide [61]. To demonstrate the feasibility of the latter, three Bragg gratings on a single planar platform, slightly offset from the neutral axis, have been designed, fabricated, and characterized.

1.2 Optical fiber devices for Mid-IR based on stretching and heating fabrication technique

The development of Mid-IR optical systems is accompanied by challenges, primarily due to the lack of standard components readily available for silica fibers. While silica optical fibers benefit from a robust infrastructure that includes various components like couplers, combiners, and splitters optimized for the visible and near-infrared ranges, comparable components for fluoride/chalcogenide glasses operating in the Mid-IR range are still immature. This gap highlights the need for significant research and innovation to create compatible optical elements for Mid-IR applications. Fluoride glasses were first discovered in 1974 and have undergone extensive research and development. Today, fluoride glasses are recognized as a well-established technology capable of transmitting light across a wide spectral range, including UV, visible, near-infrared (NIR), and Mid-IR regions [62]. As a result, research efforts have concentrated fiber components specifically designed for the Mid-IR spectrum, ensuring their effective integration into future optical systems and applications. However, fluoride glasses are susceptible to devitrification, a process in which the amorphous glass structure converts to a crystalline state [11]. Crystallization can happen during processing or at high temperatures, resulting in a decrease in optical transparency and performance. The propensity for crystallization is linked to the heavy metal content and the specific composition of the glass, which can create conditions conducive to the nucleation and growth of crystalline phases. The typical method for assessing devitrification involves measuring the crystalline fraction x. If $x < 10^{-5}$, the glass remains largely transparent with minimal scattering losses and can be categorized as vitreous [63]. If the glass becomes excessively softened, it can develop a grainy appearance due to crystallization [11]. To address this

problem, precise control of the glass composition and processing conditions is crucial. In addition, fluoride glasses are more susceptible to moisture and environmental degradation compared to silica glasses [64]. The presence of fluoride ions can make the glass more prone to hydrolysis, which can compromise the structure and impact optical performance. The glass transition temperature T_g of fluoride glasses is considerably low if compared to the widely employed silica glass. For instance, for indium fluoride (InF$_3$) glass $T_g = 275°C$, while for zirconium fluoride (ZBLAN) glass, it is approximately $T_g = 265°C$. [10]. In contrast, the glass transition temperature of silica glass is much higher, typically around $T_g = 1200°C$. Furthermore, fluoride glasses exhibit a steep viscosity-temperature relationship close to the transition point. This indicates that even a slight change in temperature can lead to a significant variation in viscosity, making the material more sensitive to thermal fluctuations. As the temperature nears T_g, the viscosity decreases sharply, resulting in greater mechanical fragility and thermal instability. This steep viscosity-temperature profile complicates the fabrication of fluoride glass optical fibers, especially during splicing and tapering [65]. Custom fusion workstations operating at low temperatures have been employed to manufacture a limited number of components, such as optical couplers and combiners, for chalcogenide glasses [11], [66], [67], [68], [69], [70]. Regarding fluoride glass, couplers based on single-mode and multimode optical fibers have been recently introduced, with excess losses as low as $EL = 0.35$ dB; additionally, optical fiber combiners utilizing end-pumping and side-pumping configurations have been developed for fluoride glass [71], [72], [5], [73], [74]. LPGs and FBGs have been inscribed on fluoride optical fibers using various techniques involving femtosecond lasers, either through the use of phase masks or through line-by-line direct inscription [75], [76], [77]. Finally, sensors

utilizing non-adiabatic tapered and side-polished fluoride optical fibers have also been reported recently [78], [79].

1.2.1 Optical fiber combiners and couplers

Optical fiber combiners can be designed according to different operating principles: i) combining the optical beams from several input fibers into a single output fiber, ii) splitting the optical beam from one input fiber into multiple output fibers, and iii) coupling the optical beam from a tapered fiber that is laterally spliced with a signal fiber. The operation of optical fiber combiners can be categorized into three distinct types: i) end-pump combiners, ii) end-pump and signal combiners, and iii) photonic lanterns [80], [81], [82], [83], [84]. The first two categories are used for power delivery in rare-earth doped optical fibers, while the third category fits well in application in which it is necessary to combine the signal of N single mode fibers into a single multimode output and viceversa [85], [86]. In the end-pump configuration, N multimode pump fibers are fused together, and typically, the waist region of the device is spliced with an output multimode optical fiber or with a double-cladding rare-earth doped fiber [87], [88]. The end-pump and signal combiner consists of a signal optical fiber encircled by N pump multimode optical fibers. All the fibers are fused together, allowing the pump power to be coupled with the signal optical fiber, resulting in a (N+1)×1 combiner [89]. The photonic lantern is composed of N single-mode (or few-mode) optical fibers fused together to produce a single multimode output. This device can be utilized for spatial division multiplexing (SDM) applications and in astronomy and spectroscopy applications, to perform spectral filtering in single mode optical fibers [90], [86]. Side-pumping involves directly coupling a pump optical fiber with a signal optical fiber through side power

coupling. Typically, coreless optical fibers or thin cladding optical fibers are pre-tapered (to reduce the confinement of the electromagnetic field) and side-spliced with the signal optical fiber with the final goal to deliver high optical power into an activated medium [91]. The 2×2 optical fiber coupler is a key component in many optical fiber systems, commonly utilized for multiplexing and demultiplexing, combining signals and pumps, as well as in ring cavities and filters [92]. In the 1990s, experiments were carried out on couplers that utilized optical fibers made from soft glasses for the first time [93]. Following that, research primarily concentrated on chalcogenide couplers for broadband, nonlinear, and wavelength-dependent applications [8], [70], [94], [95]. Fused biconical tapering and side-polished bonding techniques have been employed as fabrication techniques for zirconium fluoride couplers [72], [5]. The fused biconical tapering technique is thought to be better than side-etching and side-polishing in terms of reliability and repeatability when fabricating optical fiber couplers [66].

In this thesis, a 3×1 end-pump optical fiber combiner based on indium fluoride optical fibers has been designed, fabricated and broadband characterized in the Mid-IR spectral range [73]. Moreover, different 2×2 optical fiber couplers based on multi-mode, few-mode, and single-mode indium fluoride optical fibers have been developed and tested in the Mid-IR [71], [96], [97]. A mode-group selective photonic lantern has been designed and fabricated, demonstrating the the selectively excitation of the LP_{01} or of the LP_{11} mode group at the multi-mode end of the device, depending on the optical fiber excited at the single-mode end of the device.

1.2.2 Long period gratings

LPGs were first demonstrated in the late 1990s by means of the exposure to UV laser radiation [98], [99], [100]. Typically, LPGs can be used to couple the guided modes in the core of an optical fiber to the co-propagating cladding modes at specific resonant wavelengths, dependent on the grating geometry. This coupling leads to mode conversion and, usually, to dips in the transmission spectrum because of the attenuation of the cladding modes [101], [102]. LPGs have been widely studied in the field of optical communications [103], [104], [105]. In addition, in the field of sensing, they can mainly be engineered to identify temperature, strain, torsion, pressure, surrounding refractive index, and biochemical substances [106], [107], [108], [109]. While the UV-based fabrication method for fabricating LPGs is a well-established technology, it necessitates complex and time-consuming processes [101]. Moreover, this technique is unsuitable for non-photosensitive fibers, as zirconium fluoride fibers [110]. In recent years, alternative writing techniques for fabricating LPGs, mainly based on thermal effects, have been reported [111], [101], [112], [113], [114], [115], [116]. The mechanisms that contribute to the formation of gratings include geometrical alterations, relaxation of residual stress, diffusion of dopants, structural changes in the glass matrix, etc. [117], [118], [119]. Among these novel techniques, micro-tapering can be considered cost-effective and capable of obtaining pronounced transmission dip [120]. Until now, only femtosecond laser and corrugated rod have been employed for fluoride LPGs fabrication [76], [121], [75], [122].

In this thesis, LPGs based on single-mode zirconium fluoride optical fibers have been designed by means of coupled mode theory, fabricated via micro-tapering technique and characterized via broadband source in the Mid-IR

spectral range, demonstrating a large resonance occurring because of the coupling between the fundamental mode, i.e. LP_{01} mode, and the first symmetrical cladding mode, i.e. LP_{02} mode.

1.2.3 All-fiber interferometers

All-fiber interferometers have garnered significant interest due to their high sensitivity, low fabrication cost, and compact size [123], [124]. An implementation of all-fiber interferometers is based on non-adiabatic tapered optical fiber. The abrupt tapers excite cladding modes, and the device exploits the different optical path lengths of the electromagnetic modes in the waist region to produce a comb spectrum at the output, which shifts in response to external variations [125], [126]. Mach-Zehnder and Michelson interferometers for refractive index (RI) sensing have been proposed using non-adiabatic tapered optical fibers, produced through cost-effective processes employing the heat-and-pull method [127], [128], [129]. As already mentioned, optical fiber sensors that utilize tapering provide several benefits, including a simple design, ease of manufacturing, and cost-effectiveness [124], [130]. However, these tapered fiber sensors often exhibit relatively low RI sensitivities, and the length of the waist region is typically in the range of tens of millimeters, rendering them less suitable for compact integrated applications and making them more fragile [127]. In contrast, S-tapered optical fiber (STOF) can be considered an enhanced, miniaturized version of a fiber Mach-Zehnder interferometer [127]. This structure was firstly developed in 2011 for RI and strain detection [131]. In 2013, a novel refractive index sensor based on S-tapered photonic crystal fibers was introduced. This sensor was also proposed in combination with a hybrid long period grating to enable simultaneous measurement of both refractive index and temperature [132], [133].

Different geometries have been explored, particularly focusing on double S-tapers, different types of optical fiber cascading [134], [135], S-taper fiber coated with SiO$_2$ nanoparticles [130], and graphene oxide [136], [137]. Due to the small size and easy fabrication, the STOF has attracted research interests for the measurement of physical and biochemical parameters [138], including magnetic field [139], refractive index [135], temperature [133], humidity [136] and antigen–antibody interaction [140] etc.

In this thesis, a non-adiabatic tapered interferometer and a STOF have been developed on single-mode zirconium fluoride optical fiber, paving the way for a next-generation of optical fiber sensors which can benefit from the properties of the Mid-IR spectral range [78].

1.3   All-fiber Mid-IR optical fiber sources

Mid-IR emitting sources have collected significant attention in recent years, particularly for optical communications, environmental monitoring, and sensing [141], [142], [143]. Fiber lasers can be fabricated using diverse optical fiber materials, including chalcogenide and fluoride glasses. These optical fibers can be activated by doping or co-doping with a variety of rare-earth ions, such as dysprosium, erbium, thulium, holmium, neodymium, and praseodymium. By incorporating these ions, fiber lasers can be engineered to emit light at specific wavelength ranges, enabling their use in various applications that require targeted wavelengths [144], [145], [146], [147], [148], [149]. Fluoroindate fibers are particularly well-suited for applications in the $3 - 5 \ \mu m$ Mid-IR spectral region due to their exceptional optical transparency in this wavelength range. Many air pollutants and biomolecules exhibit characteristic light absorption peaks within this

window, making fluoroindate fibers valuable for sensing and spectroscopic applications targeting these molecules. The broad transparency window, combined with the low phonon energy of fluoroindate glasses, makes them promising candidates for the development of Mid-IR fiber lasers and amplifiers [150], [151], [152]. Erbium-, dysprosium-, and holmium-doped fluoroindate fibers have garnered significant interest due to their specific emission wavelengths [153], [154], [155]. In [156], the tunable laser emission at wavelengths near $\lambda_s = 2.31\ \mu m$ in a Tm^{3+} doped single-mode fluoride fiber laser has been reported. In [157], an Er^{3+}-doped ZBLAN fiber laser emitting around $\lambda_s = 2.7\ \mu m$, pumped at $\lambda_p = 980\ nm$, has been reported. In [158], a Ho^{3+}/Pr^{3+} co-doped fluoride fiber laser with an output power $P_s = 7.2\ W$ has been demonstrated at wavelengths close to $\lambda_s = 2.9\ \mu m$. Recently, holmium-doped fluoroindate fibers have been characterized, and CW lasers emitting at $\lambda_s = 3.92\ \mu m$ [153], with pumping at $\lambda_p = 888\ nm$, was obtained. Regarding the pulsed operation, lasing emissions at wavelength $\lambda_s = 2.106\ \mu m$ and $\lambda_s = 3\ \mu m$ have been obtained [159], [160].

In this thesis, a CW optical source is designed employing commercially available Pr^{3+}-doped fluoroindate fibers [161]. The pumping wavelength is $\lambda_p = 1550\ nm$ and the emission is $\lambda_s = 1550\ nm$ with a pump power threshold as low as $P_{th} = 0.007W$.

2 Theoretical principles

In this chapter, the theory useful for the design of Bragg gratings, Mid-IR optical fiber components, and optical fiber Mid-IR laser discussed in this Ph.D. thesis, is briefly reviewed.

2.1 Coupled Mode Theory: generic perturbation

Coupled Mode Theory (CMT) is a technique used to examine light propagation in perturbed or weakly coupled waveguides. Initially, the modes of the unperturbed or uncoupled structures are identified and solved. Subsequently, a linear combination of these modes is employed as a trial solution to Maxwell's equations for more complex perturbed or coupled structures. The general expression of Maxwell's equations is presented here [162]:

$$\begin{cases} \nabla \times E = -j\omega\mu H \\ \nabla \times H = j\omega\varepsilon E + j\omega P \end{cases} \tag{2.1}$$

The orthogonality of the modes enables us to represent any given field distribution as a superposition of waveguide modes. By doing this, it is only needed to consider the transverse field components. Assuming initially that only forward propagating modes are present in a given field with the transverse components $E_t(x, y)$ and $H_t(x, y)$ at a longitudinal position z [163], [164]:

$$E_t(x,y) = \sum_\nu \sum_\mu a_{\nu\mu} E_{\nu\mu}(x,y) + \int \int_0^\infty a(\nu,\mu)\, E(\nu,\mu,x,y) d\nu d\mu$$

$$H_t(x,y) = \sum_\nu \sum_\mu a_{\nu\mu} H_{\nu\mu}(x,y) + \int \int_0^\infty a(\nu,\mu)\, H(\nu,\mu,x,y) d\nu d\mu \tag{2.2}$$

The summation here covers the discrete and finite set of guided modes, while the integration spans the continuous spectrum of radiation modes. The discrete spectra in these expressions are analogous to those found in hollow metal waveguides, and the continuous spectrum resembles the angular spectrum of plane waves in free space.

It is convenient to normalize the modal fields by means of the cross power $\bar{P}$ [165]:

$$\bar{P} = 2 \int \int_{-\infty}^{+\infty} E_{\nu\mu} \times H_{\overline{\nu\mu}}^* \, dxdy = \delta_{\nu\bar{\nu}}\delta_{\mu\bar{\mu}}$$

$$\bar{P} = 2 \int \int_{-\infty}^{+\infty} E(\nu,\mu) \times H^*(\bar{\nu},\bar{\mu}) \, dxdy = \delta(\nu - \bar{\nu})\delta(\mu - \bar{\mu}) \tag{2.3}$$

The δ in the first equation are known as Kronecker deltas, while in the second equation they are called Dirac deltas. Then, it is possible to obtain $a_{\nu\mu}$ [164]:

$$a_{\nu\mu} = 2 \int \int_{-\infty}^{+\infty} E_t \times H_{\nu\mu}^* dxdy = 2 \int \int_{-\infty}^{+\infty} E_{\nu\mu}^* \times H_t dxdy \tag{2.4}$$

In the same way, it is possible to obtain $a(\nu,\mu)$ for radiating modes:

$$a(\nu,\mu) = 2 \int \int_{-\infty}^{+\infty} E_t \times H_{\nu\mu}^*(\nu,\mu) dxdy = 2 \int \int_{-\infty}^{+\infty} E_{\nu\mu}^*(\nu,\mu) \times H_t dxdy \tag{2.5}$$

Using this notation, it is possible to consider the mode expansion of a field 1 that includes both forward- and backward-propagating modes [164], [165].

$$
\begin{cases}
E_{1t} = \sum (a_v + b_v) E_{tv} \\
H_{1t} = \sum (a_v - b_v) H_{tv}
\end{cases}
\tag{2.6}
$$

where a_v are the coefficients of the forward waves and b_v are the coefficients of the backward waves. For the field 2, it is possible to focus on copropagating mode:

$$
\begin{cases}
E_2 = E_\mu e^{-j\beta_\mu z} \\
H_2 = H_\mu e^{-j\beta_\mu z}
\end{cases}
\tag{2.7}
$$

Substituting and considering the z component uninfluential [164], [165]:

$$
\frac{\partial}{\partial z} \int \int_{-\infty}^{+\infty} \left(\sum (a_v + b_v) E_{tv} \times H_\mu^* e^{+j\beta_\mu z} \right.
$$
$$
\left. + E_\mu^* e^{+j\beta_\mu z} \times \sum (a_v - b_v) H_{tv} \right)_z dx dy =
\tag{2.8}
$$
$$
= -j\omega \int \int_{-\infty}^{+\infty} P \cdot E_\mu^* e^{+j\beta_\mu z} dx dy
$$

Expanding the derivative on the left-hand side and noting that the integral is not zero only when $v = \mu$, we have:

$$
\frac{\partial}{\partial z} \left(\sum a_v \int \int_{-\infty}^{+\infty} E_{tv} \times H_v^* e^{+j\beta_v z} dx dy \right.
$$

$$
+ \sum b_v \int \int_{-\infty}^{+\infty} E_{tv} \times H_v^* e^{+j\beta_v z} dx dy +
$$

$$
+ \sum a_v \int \int_{-\infty}^{+\infty} E_{tv} \times H_v^* e^{+j\beta_v z} dx dy
$$

$$
\left. - \sum b_v \int \int_{-\infty}^{+\infty} E_{tv} \times H_v^* e^{+j\beta_v z} dx dy \right)_z =
$$

$$
= -j\omega \int \int_{-\infty}^{+\infty} P \cdot E_v^* e^{+j\beta_v z} dx dy
$$

(2.9)

$$
\frac{\partial}{\partial z} \left(a_\mu e^{+j\beta_\mu z} \left(2 \int \int_{-\infty}^{+\infty} E_{t\mu} \times H_\mu^* dx dy \right)_z \right)
$$

$$
= -j\omega \int \int_{-\infty}^{+\infty} P \cdot E_\mu^* e^{+j\beta_\mu z} dx dy
$$

(2.10)

$$
\frac{\partial}{\partial z} \left(a_\mu e^{+j\beta_\mu z} \right) = -j\omega \int \int_{-\infty}^{+\infty} P \cdot E_\mu^* e^{+j\beta_\mu z} dx dy
$$

The term $a_\mu = a_\mu(z)$ depends on z and it is possible to derive with respect to z:

$$
a'_\mu + j a_\mu \beta_\mu = -j\omega \int \int_{-\infty}^{+\infty} P \cdot E_\mu^* dx dy
$$

(2.11)

Now, assuming the field with two counterpropagating modes, thus with a positive phase constant, it is possible to obtain:

$$\begin{cases} E_2 = E_{-\mu} e^{j\beta_\mu z} \\ H_2 = H_{-\mu} e^{j\beta_\mu z} \end{cases} \qquad (2.12)$$

By developing parallel steps to those just used, the expression for b can be derived:

$$b'_\mu - j b_\mu \beta_\mu = +j\omega \int \int_{-\infty}^{+\infty} P \cdot E^*_{-\mu} dx dy \qquad (2.13)$$

It is possible to express the terms a and b according to the following relations:

$$\begin{cases} b_\mu = B_\mu e^{+j\beta_\mu z} \\ a_\mu = A_\mu e^{-j\beta_\mu z} \end{cases} \qquad (2.14)$$

Substituting:

$$\begin{cases} A'_\mu e^{-j\beta_\mu z} - j\beta_\mu A'_\mu e^{-j\beta_\mu z} + j\beta_\mu A'_\mu e^{-j\beta_\mu z} = -j\omega \int \int_{-\infty}^{+\infty} P \cdot E^*_\mu dx dy \\ B'_\mu e^{+j\beta_v z} + j\beta_\mu B'_\mu e^{+j\beta_\mu z} - j\beta_\mu B'_\mu e^{+j\beta_\mu z} = +j\omega \int \int_{-\infty}^{+\infty} P \cdot E^*_{-\mu} dx dy \end{cases} \qquad (2.15)$$

$$\begin{cases} A'_\mu = -j\omega \int \int_{-\infty}^{+\infty} P \cdot E^*_\mu e^{+j\beta_\mu z} dx dy \\ B'_\mu = +j\omega \int \int_{-\infty}^{+\infty} P \cdot E^*_{-\mu} e^{-j\beta_\mu z} dx dy \end{cases} \qquad (2.16)$$

If there are no sources within the guiding structure, the derivatives of the coefficients a and b are zero [164]. Consequently, the amplitudes remain constant, indicating no interaction between the analysed fields. In the following section,

simplifying assumptions will be made to obtain a more manageable mathematical model, which will still maintain the generality and validity of the model.

2.1.1 Coupled Mode Theory: dielectric perturbation

The behaviour of a dielectric material in the presence of an electric field is described by a physical quantity known as electric permittivity in electromagnetism and solid-state physics. A material is classified as "dielectric" if it can store energy when subjected to an electric field. Electric permittivity quantifies the material tendency to resist the intensity of the electric field within it. The value of electric permittivity depends on the material propensity to polarize when exposed to an electric field. The quantities that describe this phenomenon are the polarization vector and electric susceptibility. Electric permittivity varies with the orientation of the electric field and is therefore represented by a tensor. However, for a linear, homogeneous, and isotropic material, electric permittivity becomes a scalar quantity. In this case, it is referred to as the dielectric constant. When expressed in scalar form, the dielectric constant resembles a tensor that is a 3×3 matrix [164], [165]:

$$\varepsilon = \begin{bmatrix} \varepsilon_{11} & \varepsilon_{12} & \varepsilon_{13} \\ \varepsilon_{21} & \varepsilon_{22} & \varepsilon_{23} \\ \varepsilon_{31} & \varepsilon_{32} & \varepsilon_{33} \end{bmatrix} \tag{2.17}$$

If the material is not homogeneous, linear, and isotropic, the permittivity depends on additional factors such as position within the medium, or the frequency of the applied field. The imaginary part of the permittivity accounts for losses in cases where the electric field is slightly perturbed compared to the lossless scenario. The relationship connecting the dielectric constant ε, the electric field E, and the polarization vector P is given by [166]:

$$P = \Delta \varepsilon E \tag{2.18}$$

The variation in the dielectric constant $\Delta \varepsilon$ can be induced by creating periodic structures within the fiber, which facilitate signal coupling [14], [167].

$$\begin{cases} E_t = \sum (a_v + b_v) E_{tv} \\ H_t = \sum (a_v - b_v) H_{tv} \end{cases} \tag{2.19}$$

The field equations along the longitudinal axis are derived using Maxwell's equations.

$$\nabla_t \times H_t = \begin{vmatrix} \hat{x} & \hat{y} & \hat{z} \\ \dfrac{\partial}{\partial x} & \dfrac{\partial}{\partial y} & 0 \\ H_x & H_y & 0 \end{vmatrix} = \left(\dfrac{\partial H_y}{\partial x} - \dfrac{\partial H_x}{\partial y} \right) \hat{z} \tag{2.20}$$

Substituting:

$$j\omega \varepsilon E_z + j\omega \Delta \varepsilon E_z = \nabla_t \times H_t \rightarrow E_z = \frac{\nabla_t \times H_t}{j\omega(\varepsilon + \Delta \varepsilon)} \rightarrow$$
$$\rightarrow P_z = \frac{\Delta \varepsilon}{(\varepsilon + \Delta \varepsilon)} \sum (a_v - b_v) E_{zv} \tag{2.21}$$

The relationship for the longitudinal polarization vector P_z is:

$$P_z = \frac{\varepsilon \Delta \varepsilon}{(\varepsilon + \Delta \varepsilon)} \sum (a_v - b_v) E_{zv} \tag{2.22}$$

It is possible to derive the expression for the propagating field:

$$A'_\mu = -j\omega \int \int_{-\infty}^{+\infty} \left(\Delta \varepsilon \sum (a_v + b_v) E_{tv} \cdot E_{t\mu}^* \right) e^{+j\beta_\mu z} dx dy +$$
$$-j\omega \int \int_{-\infty}^{+\infty} \left(\frac{\varepsilon \Delta \varepsilon}{(\varepsilon + \Delta \varepsilon)} \sum (a_v - b_v) E_{zv} E_{z\mu}^* \right) e^{+j\beta_\mu z} dx dy \tag{2.23}$$

$$B'_\mu = +j\omega \int\int_{-\infty}^{+\infty} \left(\Delta\varepsilon \sum (a_\nu + b_\nu) E_{t\nu} \cdot E^*_{-t\mu} \right) e^{-j\beta_\mu z} dxdy +$$

$$+j\omega \int\int_{-\infty}^{+\infty} \left(\frac{\varepsilon\Delta\varepsilon}{(\varepsilon + \Delta\varepsilon)} \sum (a_\nu - b_\nu) E_{z\nu} E^*_{-z\mu} \right) e^{-j\beta_\mu z} dxdy \qquad (2.24)$$

Similarly, it is possible to derive the expressions for the counterpropagating field:

$$A'_\mu = -j\omega \int\int_{-\infty}^{+\infty} \left(\Delta\varepsilon \sum (a_\nu + b_\nu) E_{t\nu} \cdot E^*_{t\mu} \right) e^{+j\beta_\mu z} dxdy +$$

$$-j\omega \int\int_{-\infty}^{+\infty} \left(\frac{\varepsilon\Delta\varepsilon}{(\varepsilon + \Delta\varepsilon)} \sum (a_\nu - b_\nu) E_{z\nu} E^*_{z\mu} \right) e^{+j\beta_\mu z} dxdy \qquad (2.25)$$

$$B'_\mu = +j\omega \int\int_{-\infty}^{+\infty} \left(\Delta\varepsilon \sum (a_\nu + b_\nu) E_{t\nu} \cdot E^*_{t\mu} \right) e^{-j\beta_\mu z} dxdy +$$

$$-j\omega \int\int_{-\infty}^{+\infty} \left(\frac{\varepsilon\Delta\varepsilon}{(\varepsilon + \Delta\varepsilon)} \sum (a_\nu - b_\nu) E_{z\nu} E^*_{z\mu} \right) e^{-j\beta_\mu z} dxdy \qquad (2.26)$$

To simplify the previous expressions and to make them more compact, we can introduce the following transverse and longitudinal coupling coefficients, which take on the following expressions:

$$\begin{cases} K^t_{\nu\mu} = \omega \int\int_{-\infty}^{+\infty} \Delta\varepsilon E_{t\nu} \cdot E^*_{t\mu} dxdy \\ K^z_{\nu\mu} = \omega \int\int_{-\infty}^{+\infty} \frac{\varepsilon\Delta\varepsilon}{(\varepsilon + \Delta\varepsilon)} E_{z\nu} E^*_{z\mu} dxdy \end{cases} \qquad (2.27)$$

The derivatives of the coefficients A_μ and B_μ can be rewritten:

$$\begin{cases} A'_\mu = -j \sum \{ A_\nu (K^t_{\nu\mu} + K^z_{\nu\mu}) e^{-j(\beta_\nu - \beta_\mu)z} + B_\nu (K^t_{\nu\mu} - K^z_{\nu\mu}) e^{-j(\beta_\nu + \beta_\mu)z} \} \\ B'_\mu = -j \sum \{ A_\nu (K^t_{\nu\mu} - K^z_{\nu\mu}) e^{-j(\beta_\nu + \beta_\mu)z} + B_\nu (K^t_{\nu\mu} + K^z_{\nu\mu}) e^{-j(\beta_\nu - \beta_\mu)z} \} \end{cases} \qquad (2.28)$$

Eq. (2.28) provides a general formulation of the problem. In reality, the modes to consider are not infinite but are rather a limited number, which simplifies and makes the practical treatment much more effective. As previously noted, a non-zero derivative arises if there is a perturbation, which is included in the definition of the coupling coefficients. Specifically, if $\Delta\varepsilon$ is zero, the derivative would be zero. Additionally, from (2.28), it can be observed that the coupling depends on both transverse and longitudinal modes, including both counterpropagating- and forward-propagating modes.

2.1.2 Coupled Mode Theory: fiber gratings

Generally, the inscription of a grating via UV writing in an optical fiber induces a refractive index change in the core along the length of the fiber $n_{co}(z)$ [168], [167], [169], [170]. The cladding refractive index n_{cl} and the refractive index of the surrounding environment, usually air, n_{air} remains unchanged [169]:

$$
n = \begin{cases} n_{co}\left\{1 + \sigma(z)\left[1 + m cos\left(\dfrac{2\pi z}{\Lambda(z)}\right)\right]\right\} \\ n_{cl} \\ n_{air} \end{cases} \begin{cases} r \le r_{co} \\ r_{co} < r \le r_{cl} \\ r > r_{cl} \end{cases} \qquad (2.29)
$$

where n_{co} is the unperturbed refractive index, z is the longitudinal direction, $\sigma(z)$ is the slowly varying envelope of the grating, m is the fringe modulation, $\Lambda(z)$ is the grating period, r_{co} is the core radius, r_{cl} is the cladding radius [39]. $n_{co}\sigma(z)$ is the average dc induced refractive index change in a grating period [169]. Only the transverse coupling coefficients can be considered since the longitudinal field components are negligible with respect to the transverse field components [168], [170]:

$$K_{\nu\mu}(z) = k_{\nu\mu}(z)\left[1 + mcos\left(\frac{2\pi z}{\Lambda(z)}\right)\right] \qquad (2.30)$$

$$k_{\nu\mu}(z) = \frac{\omega\varepsilon_0 n_{co}^2 \sigma(z)}{2} \iint_{\Omega_c} E_\nu(x,y,z) \cdot E_\mu^*(x,y,z)dxdy \qquad (2.31)$$

E is the transverse electric field, Ω_c is the core area (i.e. where the grating is written), ω is the angular frequency, ε_0 is the vacuum permittivity.

2.2 Opto-mechanical modelling

The refractive index tensor for dielectric materials in cartesian coordinates can be expressed as follows; since the tensor is symmetric, it is represented by six components, instead of nine [171]:

$$n = \begin{bmatrix} n_{xx} & n_{xy} & n_{xz} \\ n_{yx} & n_{yy} & n_{yz} \\ n_{zx} & n_{zy} & n_{zz} \end{bmatrix} = \begin{bmatrix} n_1 & n_6 & n_5 \\ n_6 & n_2 & n_4 \\ n_5 & n_4 & n_3 \end{bmatrix} \qquad (2.32)$$

The photo-elastic and thermo-optic effects are described by introducing a dielectric permittivity tensor [172]:

$$\begin{cases} B_i = \dfrac{1}{n_i^2}, & i = 1,2,3 \\ B_i = 0, & i = 4,5,6 \end{cases} \qquad (2.33)$$

By neglecting the second-order terms, the change in the impermeability tensor (ΔB_i), due to the applied strain (photo-elastic effect) and temperature (thermo-optic effect), is obtained by [173], [174]:

$$\Delta B_i = Q_i \Delta T + p_{ij}\epsilon_{ij}, \quad i,j = 1 \dots 6 \qquad (2.34)$$

$[p]$ is the strain-optic tensor and, for an isotropic material, it is defined as [171]:

$$p = \begin{bmatrix} p_{11} & p_{12} & p_{12} & 0 & 0 & 0 \\ p_{12} & p_{11} & p_{12} & 0 & 0 & 0 \\ p_{12} & p_{12} & p_{11} & 0 & 0 & 0 \\ 0 & 0 & 0 & (p_{11} - p_{12})/2 & 0 & 0 \\ 0 & 0 & 0 & 0 & (p_{11} - p_{12})/2 & 0 \\ 0 & 0 & 0 & 0 & 0 & (p_{11} - p_{12})/2 \end{bmatrix} \tag{2.35}$$

ϵ are the elements of the strain tensor:

$$\epsilon = \begin{bmatrix} \epsilon_1 & \epsilon_6 & \epsilon_5 \\ \epsilon_6 & \epsilon_2 & \epsilon_4 \\ \epsilon_5 & \epsilon_4 & \epsilon_3 \end{bmatrix} \tag{2.36}$$

For optically isotropic materials [171]:

$$\Delta B_i = \frac{d\left(\frac{1}{n_i^2}\right)}{dT} \Delta T - p_{ij} \alpha_j \Delta T + p_{ij} \epsilon_{ij}, \quad i, j = 1 \dots 6 \tag{2.37}$$

$$\begin{cases} \alpha_j = \alpha, & i = 1,2,3 \\ \alpha_j = 0, & i = 4,5,6 \end{cases} \tag{2.38}$$

Substituting, it is possible to obtain the refractive index change due to temperature variation ΔT and strain ϵ [171]:

$$
\begin{cases}
\Delta n_1 = -\frac{n_1^3}{2}\big(p_{11}\epsilon_1 + p_{12}(\epsilon_2 + \epsilon_3)\big) + \frac{dn}{dT}\Delta T + \frac{n_1^3}{2}(p_{11} + 2p_{12})\alpha\Delta T \\[2mm]
\Delta n_2 = -\frac{n_2^3}{2}\big(p_{11}\epsilon_2 + p_{12}(\epsilon_1 + \epsilon_3)\big) + \frac{dn}{dT}\Delta T + \frac{n_2^3}{2}(p_{11} + 2p_{12})\alpha\Delta T \\[2mm]
\Delta n_3 = -\frac{n_3^3}{2}\big(p_{11}\epsilon_3 + p_{12}(\epsilon_2 + \epsilon_1)\big) + \frac{dn}{dT}\Delta T + \frac{n_3^3}{2}(p_{11} + 2p_{12})\alpha\Delta T \\[2mm]
\Delta n_4 = -\frac{n_4^3}{4}(p_{11} - p_{12})\epsilon_4 \\[2mm]
\Delta n_5 = -\frac{n_5^3}{4}(p_{11} - p_{12})\epsilon_5 \\[2mm]
\Delta n_6 = -\frac{n_6^3}{4}(p_{11} - p_{12})\epsilon_6
\end{cases}
\tag{2.39}
$$

To study the effect of curvature on refractive index, conformal mapping method can be considered. In particular, a curved optical waveguide, with a cross-sectional refractive index distribution n, can be mapped into a straight one. In case of large curvature radius R (with respect to the size of the device), the equivalent straight optical waveguide can be described by a cross-sectional refractive index distribution n_s [175]:

$$
n_s = n(1 + Cx_{proj})
\tag{2.40}
$$

$C = 1/R$ is the curvature and $x_{proj} = r\cos(\theta)$ is the projection of each point of the optical waveguide over the plane perpendicular to the neutral plane, as shown in Figure 2.1. The modified cross-sectional refractive index distribution n_s is affected by strain components:

$$
\epsilon_2 = \epsilon_3 = -\nu\epsilon_1
\tag{2.41}
$$

$$
\epsilon_1 = Cx_{proj}
\tag{2.42}
$$

They alter the cross-sectional refractive index distribution n which needs to be evaluated by considering the stress-optic relations:

$$n = n_0 + \Delta n = n_0 - \left(\frac{n_0^3}{2}\right)(p_{12} - vp_{12} - vp_{11})Cx_{proj} \qquad (2.43)$$

where n_0 is the refractive index distribution of the optical waveguide without curvature, p_{11} and p_{12} the components of the photo-elastic tensor. For silica glass, $p_{11} = 0.121$, $p_{12} = 0.27$, $v = 0.16$ [60].
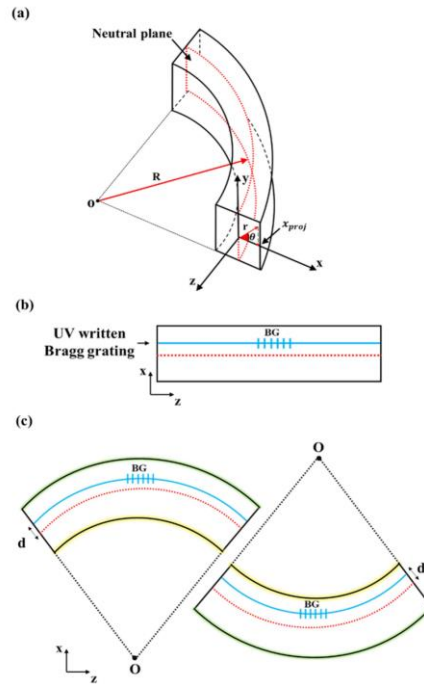

Figure 2.1   (a) 3D-sketch of a curved waveguide. (b) 2D-sketch of the straight optical waveguide. (c) 2D-sketch of the curved optical waveguide with positive (left) and negative (right) curvature C (green colored line for tensile strain, yellow colored line for compressive strain) [60].

2.3 Optical fiber taper

As previously described, the method for tapering optical fibers involves partially melting the fiber and applying a tensile force to stretch and thin it. The outcome of this process is a structure like that depicted in Figure 2.2, i.e. a fused biconical taper. According to this sketch, d_{cl} is the original fiber cladding diameter and d_{cl-w} is the cladding diameter of the narrowest part of the taper (i.e. waist region) having a length L_w. Each transition region has a length Z_0 and the profile depends on the decreasing radius function $r_{cl}(z) = d_{cl(z)}/2$, where z is the longitudinal coordinate. Let us define e the elongation undergone by the fiber and L_0 the starting length that is heated and stretched [176]. The radius profile r_w can be defined as [177], [178]:

$$r_w(e) = r_0^{-\left(\frac{e}{2L_0}\right)} \tag{2.44}$$

Moreover:

$$2Z_0 = e + L_0 - L_w \tag{2.45}$$

Then, considering $L_w = L_0$:

$$r_{cl}(z) = r_{cl}^{-\left(\frac{z}{L_0}\right)} \tag{2.46}$$

Propagation losses in optical fiber devices are caused by scattering, which involves light being radiated from the fiber core, and by the coupling of core modes to cladding radiation modes [179]. Scattering losses are negligible if $\lambda/n_{cl} \leq Z_0$, where λ is the wavelength in vacuum of the light signal and n_{cl} is the refractive index of the fiber cladding. On the other hand, the modal coupling losses are negligible if $Z_0 \leq Z_c$, with $Z_c = 2\pi/|\beta_1 - \beta_2|$ being the beat length [129].

Here, β_1 is the propagation constant of the core mode and β_2 is the propagation constant of the cladding mode closest to β_1. Considering both criteria:

$$\lambda/n_{cl} \leq Z_0 \leq Z_c \tag{2.47}$$

In a tapered optical fiber, the above condition is met when the tapering angle Ω between the fiber axis and any point on the interface between the core and the cladding in the transition region is sufficiently small [180]:

$$\Omega \leq \frac{r_{co}(z)}{2\pi}|\beta_1 - \beta_2| \tag{2.48}$$
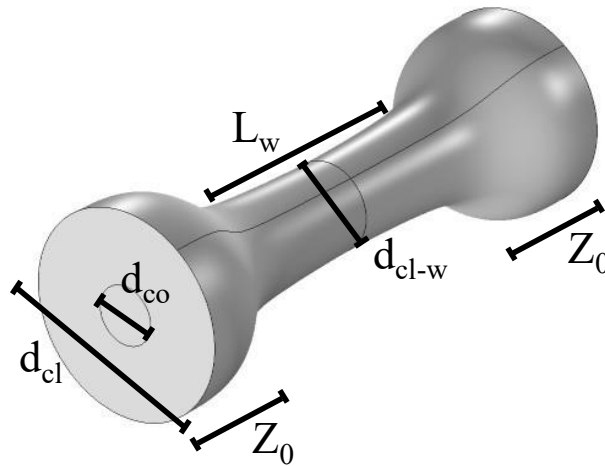

Figure 2.2   Sketch of a taper on a single-mode optical fiber.

2.3.1 Optical fiber combiner

The optical fiber combiner, typically, features the following interfaces, as shown in Figure 2.3:

- On one end, there is a fiber that should be connected to a specific type of active fiber, often through fusion splicing. Sometimes, an additional passive fiber can be included between these two sections, e.g. an FBG, if it cannot be incorporated into the active fiber.
- On the other end, the combiner has several input multimode fibers that can be connected to fiber-coupled pump laser diodes. Additionally, there is often another fiber (either single-mode or few-mode) through which signal light can be injected or extracted. For a fiber laser, the signal light is not injected, and the laser light is extracted from the other end.

In addition to the adiabatic criterion to bridge the two ends, to avoid significant losses, the beam brightness, proportional to transmitted optical power, should be maintained [97], [158]. In other words, the brightness ratio BR allows to estimate the transmission loss of the designed combiner:

$$BR \simeq \frac{D_{out}^2 NA_{out}^2}{ND_{in}^2 NA_{in}^2} \geq 1 \tag{2.49}$$

where N defines the number of input fibers, NA_{in} and NA_{out} defines numerical apertures of input fibers and output fiber, and D_{out} and D_{in} are the core diameters of output and input fibers. If the brightness principle is respected, i.e. if $BR > 1$, the intensity launched into the input ports is equal to the intensity of the beam at the combiner output. $BR < 1$ means a loss of the beam brightness, i.e. the beam intensity at the output is lower than at the input.
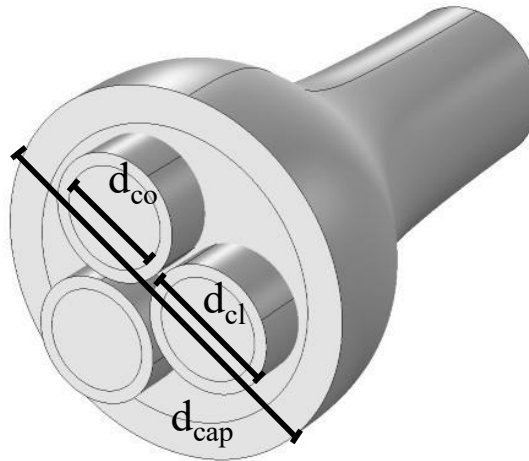
Figure 2.3   Sketch of a taper on an optical fiber combiner; different multi-mode optical fibers are inserted in a capillary and then tapered down.

2.3.2 Optical fiber coupler

Optical fiber couplers can be manufactured using the fused biconical tapering method. In the case of symmetric couplers, two identical optical fibers are placed in proximity (twisted or inside a low-refractive index glass capillary) and then heated and stretched over a short length. Power coupling between the electromagnetic modes happens in the waist region, where the characteristic periodic exchange of power between the modes occurs, as shown in Figure 2.4. CMT is typically used in electromagnetic design to describe the co-directional coupling for the HE_{11} mode [8], [181]. By considering that $\beta_{11} = \beta_{12} = \beta_1$, $\beta_{12} = \beta_{21} =$

β_2, $K_{12} = K_{21} = K$, a simplified form of coupled mode equations, derived from CMT, can be employed [8], [181]:

$$\frac{dA_1}{dz} = -jA_2K_{12}^{-j(\beta_2-\beta_1)z} \tag{2.50}$$

$$\frac{dA_2}{dz} = -jA_1K_{21}^{-j(\beta_2-\beta_1)z} \tag{2.51}$$

The solution of these differential equations is:

$$A_1(z) = A_0 cos\,(kz) \tag{2.52}$$

$$A_2(z) = A_0 \sin\,(kz) \tag{2.53}$$

Considering $P_0 = A_0^2$ as the input power in one of the two legs of the coupler, the output power at each output port can be calculated as [8], [181]:

$$P_C(L_w) = P_0 \sin^2(\kappa L_w) \tag{2.54}$$

$$P_T(L_w) = 1 - P_C(L_w) = P_0 \cos^2(\kappa L_w) \tag{2.55}$$

$$\kappa = \frac{K_0\left(\frac{WD}{r_{co1}}\right)U^2}{k_0 n_{co}\left(r_{co1}VK_1(W)\right)^2} \tag{2.56}$$

$$U = r_{co1}\sqrt{n_{co}^2 k_0^2 - \beta^2} \tag{2.57}$$

$$W = r_{co1}\sqrt{\beta^2 - n_{cl}^2 k_0^2} \tag{2.58}$$

L_w is the waist length, κ the coupling coefficient, r_{co1} the core radius in the waist region, D the core-to-core distance in the waist region, n_{co} the core refractive index, n_{cl} the cladding refractive index, K_0, and K_1 the Bessel functions of the second kind (respectively evaluated at WD/r_{co1} and W), V the normalized frequency, k_0 the wave number, β the propagation constant.
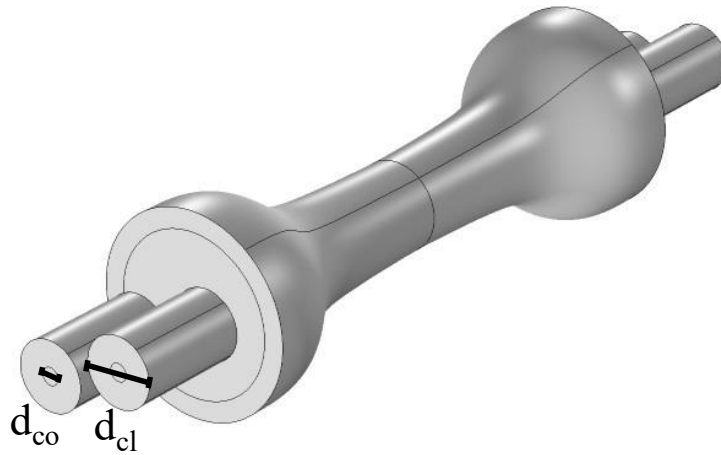
d_{co} d_{cl}

Figure 2.4   Sketch of an optical fiber combiner; two optical fibers in a low refractive index ca-
pillary are tapered and a periodic exchange of power among them is obtained in the
waist region.

Excess loss is calculated as $EL = 10\log\left(P_0/(P_T(L_w) + P_C(L_w))\right)$, while the coupling ratio CR is dependent on the optical power coming from each output port divided by the total output power [182]:

$$CR_T = P_T(L_w)/(P_T(L_w) + P_C(L_w)) \tag{2.59}$$

$$CR_C = P_C(L_w)/(P_T(L_w) + P_C(L_w)) \tag{2.60}$$

The coupling ratio CR and its spectral dependence are strongly influenced by the geometry of the optical fiber coupler, e.g. waist diameter and length. The excess loss EL is affected by the quality and the geometry of the transition. To prevent coupling of higher-order cladding modes, the transition must be adiabatic, allowing the mode to be treated as a series of local versions of the excitation [182].

2.3.3 Photonic lantern

Typically, a photonic lantern consists of an optical device that links a single multi-mode core to an array of identical waveguides, each supporting fewer modes (usually single-mode) [84], [183]. During the transition, the core diameters are reduced, corresponding to a decreasing in optical field confinement. For small photonic lantern diameters, the individual waveguides are coupled among each other, resulting in the formation of non-degenerate mode groups. Specifically, for three identical optical fibers, as shown in Figure 2.5, light launched into one or more fibers at the Single-Mode End (SME) excites multiple propagation modes at the Multi-Mode End (MME), i.e. the LP_{01} mode and the LP_{11} mode [84]. In the reverse direction, light excites the array of optical fibers at the SME based on the transverse distribution of mode amplitudes and phases in the transition region where the cores are weakly coupled [184], [185]. In spatial division multiplexing/demultiplexing, each propagation mode functions as a separate channel [186]. Therefore, mode control and selectivity are necessary to prevent mode scrambling. To achieve this control, different single-mode optical fibers are used [186]. This enables the propagation mode guided in one of the optical fibers at SME to be directed into specific mode groups LP, at MME. Thus, for this operation, a 3-mode photonic lantern requires the handling of the LP_{01} and of the LP_{11} modes [186]. This can be obtained employing three optical fibers, one with a propagation mode with phase constant β_1 larger than β_2 of the propagation modes pertaining to the other two identical optical fibers. The mode guided by the first fiber (with phase constant β_1) evolves into the first propagation mode at the MME, i.e. LP_{01} of the photonic lantern mode. The modes having phase constant β_2 evolve into an orthogonal combination of the spatial modes (odd and even) of the LP_{11} mode group at the MME [186].
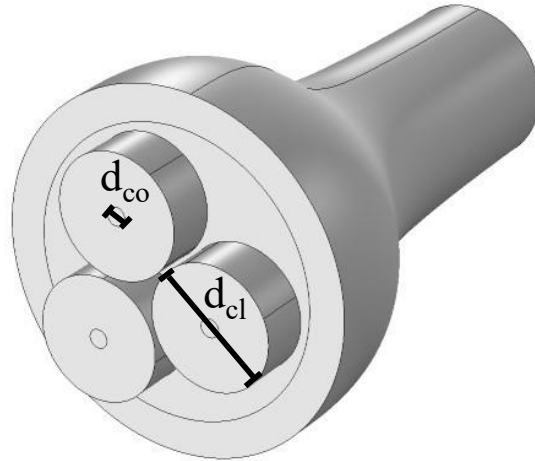
Figure 2.5   Sketch of a photonic lantern; different single-mode optical fibers are inserted in a capillary and the whole structure is tapered down.

By considering three optical fibers, each with a different normalized frequency V, the propagation mode guided in one of the optical fibers at the SME can also be forced to evolve into specific spatial modes. However, this solution is rarely used, because of mode-mixing in multi-mode fibers [187], [188]. It is worthwhile noting that the mode-selective behaviour of photonic lanterns can be enhanced by using a higher number of optical fibers.

It is crucial to achieve low loss in both directions. Losses are ascribed to the reduction in mode number, and the mode-order changing [189], [191], [190]. In case of light incoherently distributed among the excited modes, the number of modes at the MME N_{MME} should be equal to the number of modes at the SME N_{SME} to obtain a bidirectional device, in agreement with the brightness theorem

of optics [191], [192]. In particular, the loss related to mode number changing is $L_M(dB) = 10|log_{10}(N_{SME}/N_{MME})|$ [84]. Mode-order changes can lead to additional losses because, in symmetric structures, propagation modes might alter their modal order along the tapered region [90]. To prevent this issue, the cores must be positioned to overlap and sample the electromagnetic field adequately at the MME [90].

2.3.4 All-fiber interferometers

Tapering an optical fiber implies reducing the core and cladding diameters by heating and stretching the fiber until a waist region is formed [193]. In a non-adiabatic taper, the power of the fundamental mode LP_{01}, propagating through the transition and waist regions, is coupled into higher-order modes (usually of the same symmetry), due to sharp transitions, as shown in Figure 2.6. Due to the varying optical paths of the electromagnetic modes, a Mach-Zehnder interferometer effect is produced, resulting in a comb-like spectral pattern at the output [139]. The two-beam optical interference equation allows to estimate the output intensity [194], [195]:

$$I = I_1 + I_2 + 2\sqrt{I_1 I_2} \cos(\Delta\phi) \qquad (2.61)$$

$$\Delta\phi = \frac{2\pi\Delta n_{eff} L_{eff}}{\lambda} \qquad (2.62)$$

I_1, I_2 are the core and cladding mode intensities respectively, Δn_{eff} is the effective refractive index difference between the core and cladding modes, $\Delta\phi$ is the phase difference between the core and cladding modes, L_{eff} is the effective length of the taper, λ is the wavelength. External quantities can induce a variation

of both Δn_{eff} and L_{eff} and thus change the spectral properties of the device [194], [195].

Similar to the non-adiabatic tapered sensor, the main concept behind the S-tapered fiber structure is to combine both interference arms within a single fiber [194]. Figure 2.7 illustrates a schematic diagram of the S-tapered fiber, consisting of two abrupt bends and a straight section [196]. The presence of the initial S-tapered region excites high-order cladding modes [195], [197]. The fundamental core mode and the high-order cladding modes propagate through the straight section until they reach the second bend. At this point, the high-order cladding modes recouple and interfere with the fundamental core mode [130]. In other words, light is initially coupled from the fiber core to the cladding in the first bending section, and then it is partially coupled back from the cladding to the core in the second bending section [127].
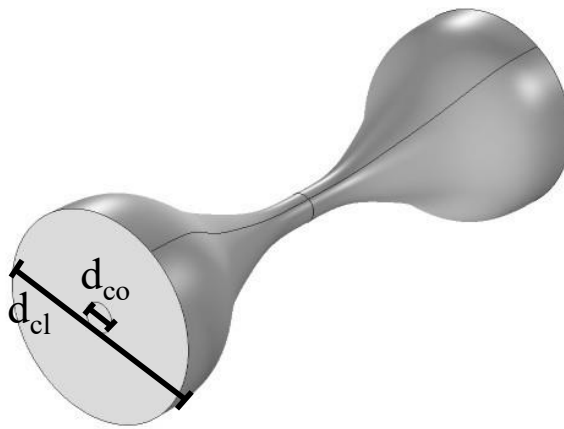

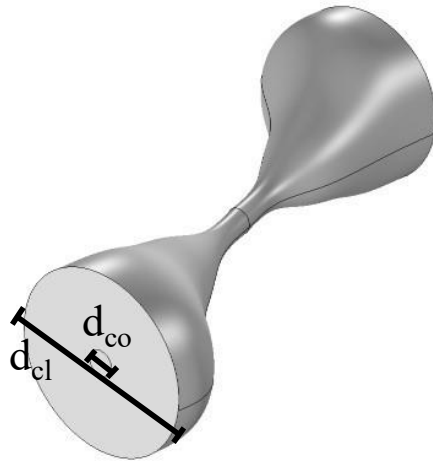Figure 2.6   Sketch of a non-adiabatic taper.

Figure 2.7   Sketch of S-tapered optical fiber.

In the waist section, the cladding mode field extends outside the fiber and interacts with the surrounding environment, acting as the sensing arm, while the core mode remains confined within the fiber core, serving as the reference arm [196].

2.4   Mid-IR fiber source based on Pr³⁺-doped fluoroindate fiber

The praseodymium-doped glass emitting at $\lambda_s = 4\ \mu m$ when pumped at $\lambda_p = 1550\ nm$ can be modelled by a 5-level scheme, as illustrated in Figure 2.8. It considers: i) pumping (bold black arrow), ii) stimulated emission (bold red arrow), iii) radiative and non-radiative emissions, iv) Excited State Absorption

(ESA), v) cross-relaxation (CR) phenomena [161]. By considering the well-known rate equation approach, the following nonlinear system can be solved to evaluate the ion populations $N_1, \dots, N_5$:

$$\frac{\partial N_1}{\partial t} = -W_{14}N_1 + W_{41}N_4 + A_{51}N_5 + A_{41}N_4 + A_{31}N_3 + A_{21}N_2 \qquad (2.63)$$
$$+ W_{NR21}N_2 - W_{CRN1}N_5 + W_{NR51}N_5$$

$$\frac{\partial N_2}{\partial t} = -W_{25}N_2 + W_{52}N_5 - \frac{1}{\tau_{R2}}N_2 + A_{52}N_5 + A_{42}N_4 + A_{32}N_3 \qquad (2.64)$$
$$+ W_{CRN1}N_5 + W_{NR32}N_3 - W_{NR21}N_2$$

$$\frac{\partial N_3}{\partial t} = -W_{34}N_3 + W_{43}N_4 - \frac{1}{\tau_{R3}}N_3 + A_{53}N_5 + A_{43}N_4 - W_{NR32}N_3 \qquad (2.65)$$
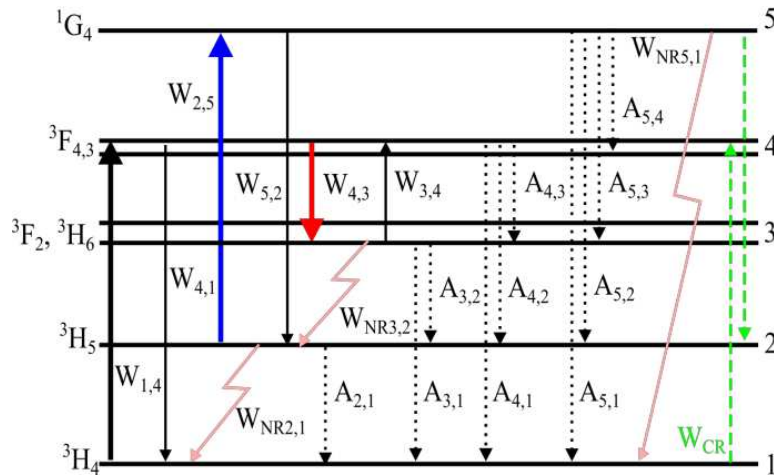

Figure 2.8   Energy levels scheme, including pumping (bold black arrow), stimulated emission (bold red arrow), radiative (dotted arrows) and nonradiative (lightning arrows) emissions, Excited State Absorption (ESA) (blue bold arrow), and cross-relaxation (CR) (green dashed arrows) phenomena.

$$\frac{\partial N_4}{\partial t} = W_{14}N_1 - W_{41}N_4 - W_{43}N_4 + W_{34}N_3 - \frac{1}{\tau_{R4}}N_4 + A_{54}N_5 \tag{2.66}$$
$$+ W_{CRN1}N_5$$

$$\frac{\partial N_5}{\partial t} = W_{25}N_2 - W_{52}N_5 - \frac{1}{\tau_{R5}}N_5 - W_{CRN1}N_5 - W_{NR51}N_5 \tag{2.67}$$

where $A_{i,j} = \frac{\beta_{i,j}}{\tau_i}$ are the radiative decays, τ_i are the $i-$th level lifetimes, $\beta_{i,j}$ are the branching ratios, W_{CR} is the cross relaxation rate, and $W_{NR,ij}$ are the non-radiative decay rates. The ion population condition $N_{Pr} = N_1 + N_2 + N_3 + N_4 + N_5$ is considered. The coefficients W_{ij} are the transition rates for $i \rightarrow j$ transition defined as:

$$W_{i,j} = \frac{\sigma_{i,j}(\lambda_{p/s})}{h\nu_{p/s}A_d}P_{p/s}\Gamma_{p/s} \tag{2.68}$$

P_p the pump power, P_s the forward signal power, $\sigma_{i,j}(\lambda_{p/s})$ is the emission/absorption cross section at the wavelength $\lambda_{p/s}$ for the transition $i \rightarrow j$, h is the Planck constant, $\Gamma_{p/s}$ the overlap coefficients of pump and signal beams with the doped area A_d, i.e. the core area, $\nu_{p/s}$ the pump/signal frequency. The power propagation along the fiber, for the pump P_p and for the signal P_s, is modeled by considering:

$$\frac{\partial P_p}{\partial z} = [g_p(z) - \alpha]P_p(z) \tag{2.69}$$

$$\frac{\partial P_s^\pm}{\partial z} = \pm[g_s(z) - \alpha]P_s^\pm(z) \tag{2.70}$$

where α is the glass attenuation, and g_p and g_s are the pump and signal gains:

$$g_p(z) = \left[-\sigma_{14}(v_p)N_1(z) + \sigma_{41}(v_p)N_4(z)\right]\Gamma_p$$
$$+ \left[-\sigma_{25}(v_p)N_2(z) + \sigma_{52}(v_p)N_5(z)\right]\Gamma_p \qquad (2.71)$$

$$g_s(z) = \left[-\sigma_{34}(v_s)N_3(z) + \sigma_{43}(v_s)N_4(z)\right]\Gamma_s \qquad (2.72)$$

The following boundaries conditions are imposed:

$$P_p(0) = P_p \qquad (2.73)$$

$$P_s{}^+(0) = R_{in}Ps^-(0) \qquad (2.74)$$

$$P_s{}^-(L) = R_{out}Ps^+(L) \qquad (2.75)$$

where $z = 0$ and $z = L$ represent the ends of the laser cavity, R_{in} and R_{out} are respectively the input and output mirror reflectivity, and P_p is the input pump power. The initial conditions for level populations are also imposed as follows:

$$N_1(0) = N_p \qquad (2.76)$$

$$N_2(0) = N_3(0) = N_4(0) = N_5(0) = 0 \qquad (2.77)$$

3 Fiber Bragg Gratings with non-conventional optical platforms

The advancement of optical sensors utilizing Bragg gratings has been induced by the demand for compact, affordable devices capable of delivering non-invasive, real-time, and highly accurate measurements of different quantities. This chapter presents the findings from the Ph.D. research related to Bragg gratings, which can be also employed as mirrors in laser cavities.

3.1 Design of Microstructured Flat Optical Fiber for Stress Monitoring in Composite Materials

In this Section, an innovative Microstructured Flat Optical Fiber (MFOF) is designed in order to achieve multiaxial strain sensing capabilities in the context of composite material monitoring. The sensing regions are the two eyelets of the MFOF where Bragg gratings can be inscribed, via DUW. To allow sensing in multiple directions, an optimized longitudinal air hole pattern (i.e. microstructure) is proposed near one of the Bragg gratings/eyelets. The effect of the strain field is evaluated via a 3D-FEM approach and is exploited to calculate the change of the refractive index. The electromagnetic modal analysis and the CMT theory are then exploited to investigate the Bragg wavelength shift for the slow and fast axis fundamental modes, guided in the two eyelets and determining the sensitivity. The designed MFOF can be embedded in composite materials

reducing the drawbacks related to both orientation and excess resin and may allow sensing performance higher than that obtainable with the cylindrical optical fibers. The following paragraphs are organized as follows: in Section 3.1.1, the advantages, and the MFOF description, in Section 3.1.2 the simulation approach and the model validation; in Section 3.1.3, the geometrical and physical parameters of both the CFRP and the MFOF; in Section 3.1.4, the numerical results; in Section 3.1.5, the conclusion.

3.1.1 Geometry and advantages of the flat optical fiber

The flat optical fiber design is ideal for embedding in composite materials, addressing issues related to resin-rich regions and orientation thanks to its geometry. This fiber is essentially a slab waveguide with a surrounding cladding and can support multimode propagation in the lateral elliptical core regions, namely "eyelets," as well as single-mode propagation in the central core region due to its thin and flat core layer [198], [199]. Single-mode waveguides can be fabricated in both the eyelets and central core layer using DUW or femtosecond laser inscription [198]. Flat optical fiber sensors are employed to detect damage, such as impact, debonding, or delamination, by comparing spectra before and after damage [35], [36], [37]. An innovative MFOF has been designed for multiparameter monitoring, offering a novel solution for triaxial strain measurement with high accuracy. The strain transfer from the host material to the sensor is carefully considered in simulations, considering the differences in mechanical properties (e.g., density, Young's modulus, Poisson's ratio) between the optical fiber and composite material [38]. Bragg gratings inscribed in both eyelets provide different transverse strain sensitivities due to a pattern of air holes in one of the eyelets [23], [200], [201]. The Bragg wavelength shift caused by the applied

stress enables the monitoring of internal strain in CFRP composites. The proposed flat optical fiber sensor is illustrated in Figure 3.1(a), showing the DUW waveguides in the eyelets, the central core layer, and the microstructure with air holes. Figure 3.1(b) depicts the uncoated MFOF sensor embedded in the sixth layer of a CFRP lamina, which consists of eight unidirectional layers. The sensor can be embedded in different layers due to the unidirectional nature of the composite. The flat optical fiber can be fabricated using modified chemical vapor deposition (MCVD).
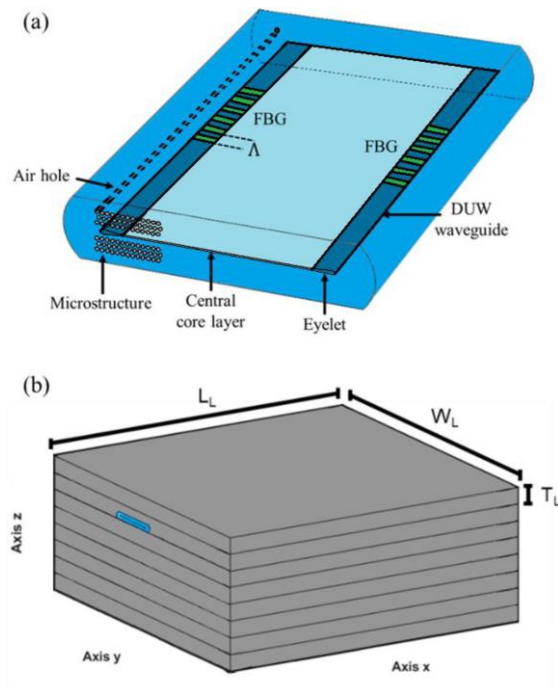
Figure 3.1   Sketch of the MFOF with air holes close to one eyelet along the x axis (a). Sketch of the simulated CFRP lamina (grey) with the embedded MFOF sensor (blue). The lamina is unidirectional, and it is composed of eight layers [40].

Previous fabrication methods resulted in cylindrical preforms collapsing into planar shapes without microstructures [198]. To incorporate the microstructure, the preform must collapse before the drawing stage. An ultrasonic mill can then form the holes directly in the preform, or appropriate silica canes can be stacked.

3.1.2 Design approach and model validation

The design approach is outlined as follows: i) 3D- FEM model using COMSOL Multiphysics to simulate the mechanical interaction and the strain transfer of the CFRP lamina with the embedded MFOF; ii) 2D-FEM mode analysis of the MFOF considering the strain of i); iii) application of the transfer matrix method (TMM) to assess the impact of strains on the reflection spectra of the gratings. The CFRP is modelled using micromechanical analysis of the unit cell, which leads to the computation of the elasticity matrix $[E]_m$ [202]. The resulting strains are used to determine the refractive index variation Δn of the optical guiding structure [202]. The effective refractive index of the fundamental modes n_{eff} guided in the two waveguides is obtained via 2D-FEM mode analysis and employed as input for the computation of the Bragg wavelength λ_B shift through TMM [167].

   The model for simulating the embedded optical fiber sensor in CFRP laminate has been validated. Specifically, both the mechanical analysis of the composite lamina and the electromagnetic modal analysis of the MFOF have been validated taking into account literature results [203] for a CFRP lamina (Toray T800H/3631, Toray Industries, Inc.) with eight cross-ply layers $[0_2/90_4/0_2]$. The physical properties of this laminate are detailed in [204], [205], [206]. Each composite lamina layer is characterized by a thickness $T_L = 0.15\ mm$, a length $L_L = 120\ mm$, and a width $W_L = 20\ mm$. A micromechanical analysis of a

single unit cell, consisting of carbon fiber and resin (with a carbon fiber-resin volume fraction $v_f = 0.6$), has been performed to compute the elasticity matrix $[E]_m$ of the layer [2]. The stress σ_x as a function of strain ϵ_x, measured using a strain gauge, is compared with simulation results. Figure 3.2 shows a comparison between the simulated tensile stress σ_x versus strain ϵ_x (purple dashed curve) and the measurements (yellow curve) reported in [203], demonstrating excellent agreement. Figure 3.3 presents the simulated reflection spectra, with no external loading ($\epsilon_x = 0\%$, dotted blue curve) and with transverse cracks having a crack density $\rho = 7\ cm^{-1}$ ($\epsilon_x = 0.42\%$, orange curve), for a uniform silica FBG with core diameter $d_{co} = 10\ \mu m$, cladding diameter $d_{cl} = 125\ \mu m$, and grating period $\Lambda = 530\ nm$.
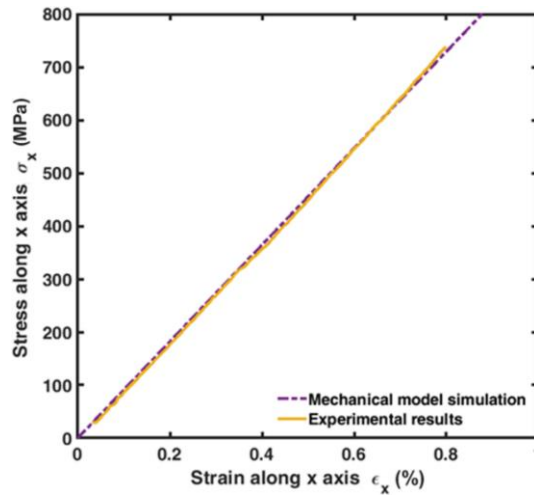

Figure 3.2   Tensile stress σ_x versus strain ϵ_x; comparison between the 3D-FEM model (purple dash dotted curve) and the experimental results (yellow curve) [40].
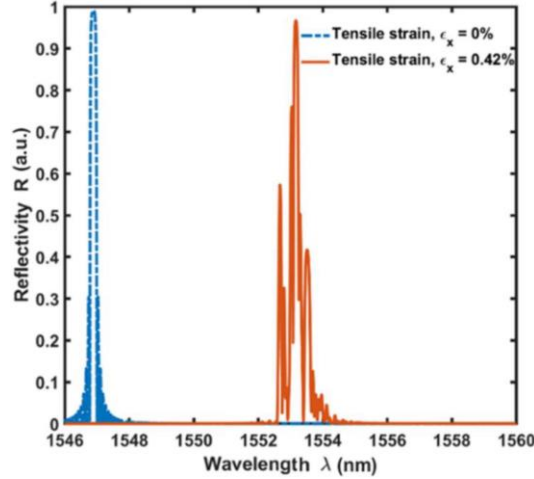
Figure 3.3   Simulated reflection spectra in absence of external loading ($\epsilon_x = 0\%$, dotted blue curve) and in presence of transverse cracks with crack density $\rho = 7\ cm^{-1}$ ($\epsilon_x = 0.42\%$, orange curve) for uniform silica FBG with core diameter $d_{co} = 10\ \mu m$, cladding diameter $d_{cl} = 125\ \mu m$ and grating period $\Lambda = 530\ nm$ [40].

The results match well with [203], confirming that the overall model and simulation approach are validated for an embedded uncoated FBG under uniaxial non-uniform strain conditions such as transverse cracks [203].

3.1.3 Design of the embedded microstructured flat optical fiber

The mechanical and electromagnetic analysis for the embedded sensor design realistically considers the geometry and physical properties of both the optical fiber and the CFRP. Specifically, parameters for the carbon fiber and epoxy resin (with a carbon fiber-resin volume fraction of $v_f = 0.6$) are detailed in Tables 3.1 and 3.2 [42]. The proposed MFOF sensor for structural health monitoring is designed to achieve efficient triaxial strain discrimination, which is closely related to the arrangement of air holes along the optical fiber length. This pattern

can be optimized by varying the diameter, pitch, and position of the air holes in the MFOF cross-section. However, it is important to note that the range of these variations is limited by mechanical robustness, which decreases as the air filling fraction increases. The physical properties of the MFOF are reported in Table 3.3, and the cross-section of the MFOF is shown in Figure 3.4. The geometrical parameters and physical properties of the MFOF, such as the height of the central layer H_L, the height of the cladding H_{cl}, the height of elliptical eyelets H_{eye}, and the length of the cladding D_{cl}, are detailed in Table 3.4 [42]. These parameters are realistic as they pertain to a fabricated flat optical fiber without microstructure [42]. DUW can be employed along the length of the flat optical fiber in the eyelets to avoid light propagation in the central core layer, thereby guiding light only in the eyelets. While the presence of air holes reduces the total UV light flux at the fiber core, a periodic interference can still be achieved with longer exposure times [207], [208]. The cladding is pure silica, while the eyelets and central core layer are doped with germanium/boron [199]. The refractive index change in the eyelets with respect to the central core region is $\Delta n_{DUW} = 5 \times 10^{-3}$ [199].

TABLE 3.1   GEOMETRICAL PARAMETERS OF THE CFRP LAMINA [40].

Parameter	Symbol	Value
Layer thickness	T_L	$0.3\ mm$
Layer length	L_L	$150\ mm$
Layer width	W_L	$40\ mm$

The refractive index is $n_{eye} = 1.4595$ for the eyelets, $n_{cc} = 1.4590$ for the central core regions, and $n_{cl} = 1.4439$ for the cladding at a wavelength of $\lambda = 1560 \, nm$.

TABLE 3.2   PHYSICAL PARAMETERS OF THE CFRP LAMINA [40].

Parameter	Symbol	Value carbon fiber	Value epoxy	Unit
Young's modulus	E	230 (x) 15 (y)	4	GPa
Shear modulus	G	24 (xy) 5.03 (yz)	–	GPa
Poisson's ratio	v	0.2 (xy) 0.07 (yz)	0.35	–
Density	ρ	1800	1100	kg/m^3

TABLE 3.3   PHYSICAL PARAMETERS OF THE CFRP LAMINA [40].

Parameter	Symbol	Value	Unit
Young's modulus	E	78.3	GPa
Poisson's ratio	v	0.186	–
Pockel's coefficient	p_{11}	0.121	–
Pockel's coefficient	ρ_{12}	0.27	–
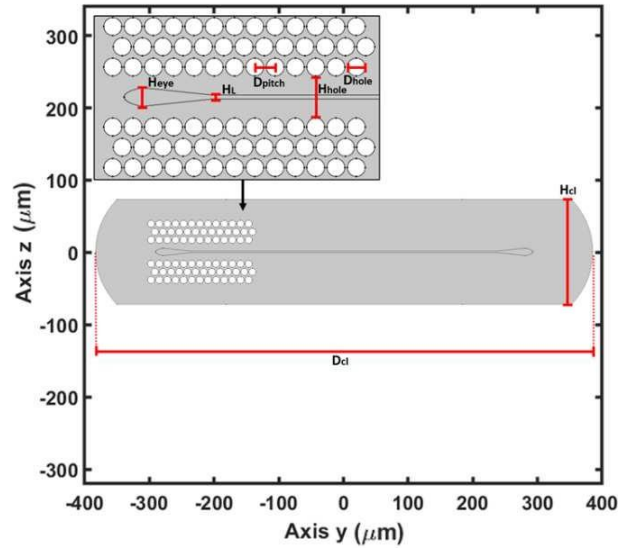
Figure 3.4   Cross-section of the proposed MFOF [40].

For a flat optical fiber with no microstructure and without external stress, with the aforementioned optical and geometrical parameters, the simulated effective refractive index of the fundamental mode guided in the eyelet is $n_{eff} = 1.4579$, which matches perfectly with measurements [42]. The design strategy focused on refining the microstructure to achieve the desired sensor response. The optimized microstructure was obtained through multiple simulations, involving both mechanical and electromagnetic investigations, in agreement with the previously described design approach. The design criterion aimed to maximize the sensitivity of one eyelet to applied loads. This can be seen in Figure 3.5, which reports the strain distribution σ_y in the MFOF cross-section embedded in the CFRP lamina under a tensile stress $\sigma_y = 35\ MPa$ along the y-axis. The air holes cause a more intense strain field in the microstructured eyelet. Therefore,

the designed pattern increases the birefringence B of the microstructured eyelet when subjected to stress along the y-axis σ_y. Birefringence arises since the two polarizations of the fundamental mode are guided with different velocities, i.e. with effective refractive indices: $n_{eff,fast}$ for the mode polarized along the fast axis and $n_{eff,slow}$ for the mode polarized along the slow axis. $\Delta\lambda_B$ between the two Bragg peaks increases with increasing birefringence. On the other hand, for stress applied along the z-axis σ_z, the strain field distribution in the microstructured eyelet has lower values compared to the stress applied to the eyelet without microstructure. Figure 3.6 reports the electric field norm distribution of the fundamental modes for the two eyelets at a wavelength of $\lambda = 1560\ nm$; the simulated effective refractive index of the fundamental mode is $n_{eff} = 1.4579$ in the unperturbed scenario.

TABLE 3.4   GEOMETRICAL PARAMETERS OF THE MFOF [40].

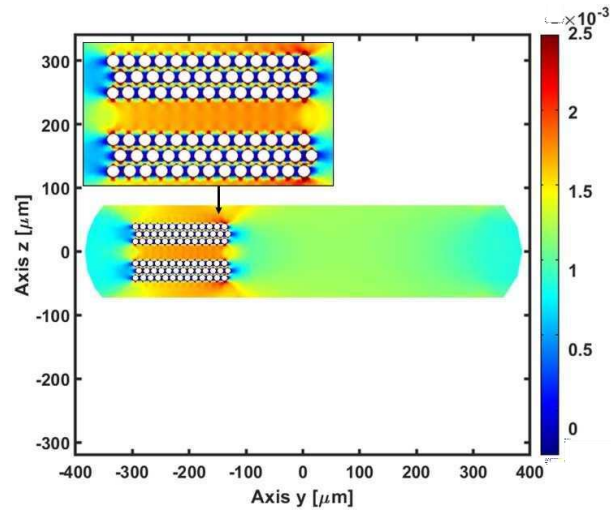| Parameter	Symbol	Value	Unit
Length of the cladding	D_{cl}	764.46	μm
Distance between the air holes	D_{pitch}	12.5	μm
Diameter of the air holes	D_{hole}	11	μm
Height of elliptical eyelets	H_{eye}	13.71	μm
Height of the central layer	H_L	2.46	μm
Height of the cladding	H_{cl}	162.33	μm
Vertical distance between holes	H_{hole}	26	μm

Figure 3.5   Strain distribution ϵ_y in the MFOF cross-section embedded in the CFRP lamina, for a tensile stress $\sigma_y = 35\ MPa$ along the y axis [40].
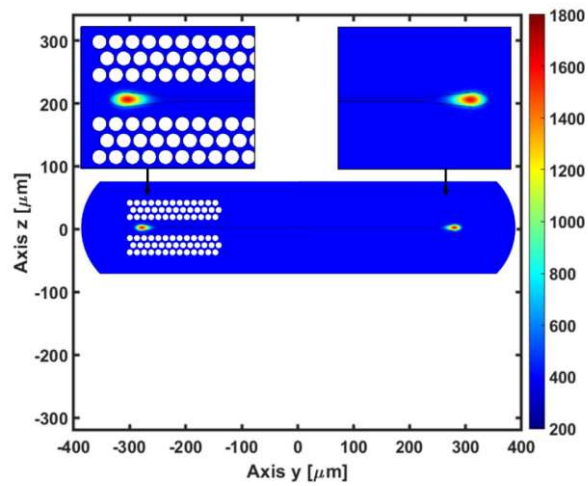

Figure 3.6   Electric field norm distribution of the fundamental modes for the microstructured eyelet and the eyelet without microstructure, at $\lambda = 1560\ nm$ [40].

Uniform FBGs with a refractive index profile change of $\Delta n_{FBG} = 3 \times 10^{-4}$ are considered in both eyelets. The other parameters of the gratings are grating period $\Lambda = 0.5349 \, \mu m$, refractive index modulation $\Delta n_{FBG} = 3 \times 10^{-4}$, grating length $L = 2000 \, \mu m$.

3.1.4 Sensitivity: numerical results

The refractive index change due to applied stress was calculated according to [202]. The reflection spectra as a function of stress were evaluated for both the eyelets, for both polarizations (i.e. fast and slow axes). Four different sensitivities were calculated by the ratio $\Delta \lambda_B / \Delta \sigma_i$, where the subscript $i = x, y, z$ indicates the stress direction. They are the fast axis propagation mode of the microstructured eyelet $K_{i,fm}$, the slow axis propagation mode of the microstructured eyelet $K_{i,sm}$, the fast axis propagation mode of the eyelet without microstructure $K_{i,f}$, the slow axis propagation mode of the eyelet without microstructure $K_{i,s}$. The longitudinal stress analysis along the x-axis considered the range from $\sigma_x = 0 \, MPa$ to $\sigma_x = 90 \, MPa$. The influence of air holes was negligible in the case of longitudinal stress σ_x and the sensitivities to stress along the x-axis σ_x are reported in Table 3.5.

Figure 3.7 shows the Bragg wavelength λ_B as a function of σ_y for both the microstructured eyelet and the non-microstructured eyelet. The graph displays the fast axis propagation mode for the microstructured eyelet (solid blue line), the slow axis propagation mode for the microstructured eyelet (orange dashed line), the fast axis propagation mode for the non-microstructured eyelet (yellow dash-dotted line), and the slow axis propagation mode for the non-microstructured eyelet (purple dotted line). The behavior of the slow and fast axes in the microstructured eyelet differs from that of the non-microstructured

eyelet. The air holes in the microstructured fiber alter the internal stress distribution within the cross-section. In materials with holes, internal stress focuses on the surface perpendicular to the applied load and passes through the hole center. When stress is applied along the y-axis σ_y, internal stress becomes concentrated along the z-axis in the microstructured region, as depicted in Fig. 3.5. This leads to a notable refractive index change, which influences the propagation mode properties and shifts the Bragg wavelength λ_B

Figure 3.8 shows the Bragg wavelength λ_B as a function of σ_z for the four reflected peaks. In this scenario, the sensitivity of the fast and slow axes for the non-microstructured eyelet is greater than that of the microstructured eyelet. This is because the air holes focus the internal stress distribution on the surface perpendicular to the direction of the applied stress σ_z, causing the stress to be distributed outside the microstructured region, with the air holes acting as a buffer. The sensitivities to transverse stresses for each polarization in the designed MFOF are summarized in Tables 3.6 and 3.7.

TABLE 3.5   SENSITIVITY TO STRESS ALONG x AXIS σ_x [40].

Parameter	Symbol	Value	Unit
Fast axis eyelet without microstructure	$K_{x,f}$	8.88	pm/MPa
Fast axis microstructured eyelet	$K_{x,fm}$	8.86	pm/MPa
Slow axis eyelet without microstructure	$K_{x,s}$	8.85	pm/MPa
Slow axis microstructured eyelet	$K_{x,sm}$	8.91	pm/MPa

TABLE 3.6   SENSITIVITY TO STRESS ALONG y AXIS σ_y [40].

Parameter	Symbol	Value	Unit
Fast axis eyelet without microstructure	$K_{y,f}$	12.89	pm/MPa
Fast axis microstructured eyelet	$K_{y,fm}$	21.06	pm/MPa
Slow axis eyelet without microstructure	$K_{y,s}$	5.02	pm/MPa
Slow axis microstructured eyelet	$K_{y,sm}$	7.22	pm/MPa

TABLE 3.7   SENSITIVITY TO STRESS ALONG z AXIS σ_z [40].

Parameter	Symbol	Value	Unit
Fast axis eyelet without microstructure	$K_{z,f}$	−3.42	pm/MPa
Fast axis microstructured eyelet	$K_{z,fm}$	−2.19	pm/MPa
Slow axis eyelet without microstructure	$K_{z,s}$	−6.48	pm/MPa
Slow axis microstructured eyelet	$K_{z,sm}$	−3.85	pm/MPa

The substantial variation in sensitivity along the transverse directions allows for effective detection of triaxial stress. The interaction between the double grating and birefringence B, induced by the applied transverse stresses, results in the appearance of four distinct peaks or dips in the reflection/transmission spectrum, potentially enabling the monitoring of an additional physical

parameter. The proposed device exhibits sensitivity to stress from all directions. In particular, to perform triaxial stress detection, the linear model proposed in [209], [210] can be used. This way, the stresses in the host material can be derived from measured wavelength shifts $\Delta\lambda_B$ using the stress transfer matrix and sensitivity matrix [209], [210]. The longitudinal strain sensitivities along the x-axis of the sensor proposed in this paper are consistent with high-performance solutions in the literature [209], [211], $S_x = 1.24\ pm/\mu m$ for both eyelets, slightly higher than those reported in [29].
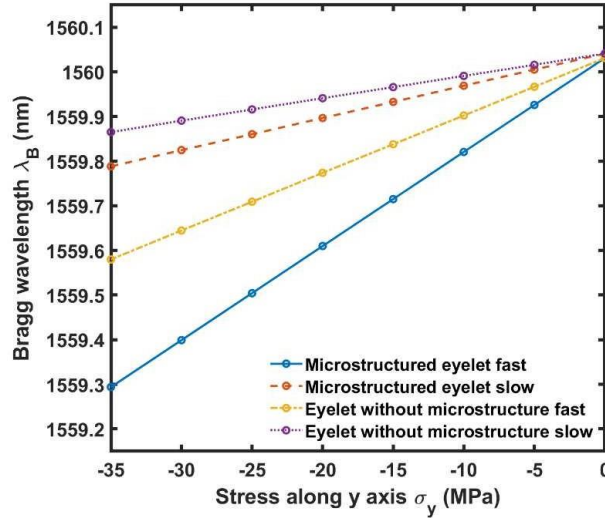
Figure 3.7   Simulated Bragg wavelength λ_B versus the transverse stress σ_y; fast axis microstructured eyelet (continuous blue), slow axis microstructured eyelet (orange dashed), fast axis eyelet without microstructure (yellow dash dotted), slow axis eyelet without microstructure (purple dotted). Grating characteristics: $\Lambda = 0.5349\ \mu m$, $\Delta n_{FBG} = 3 \times 10^{-4}$, $L = 2000\ \mu m$ [40].
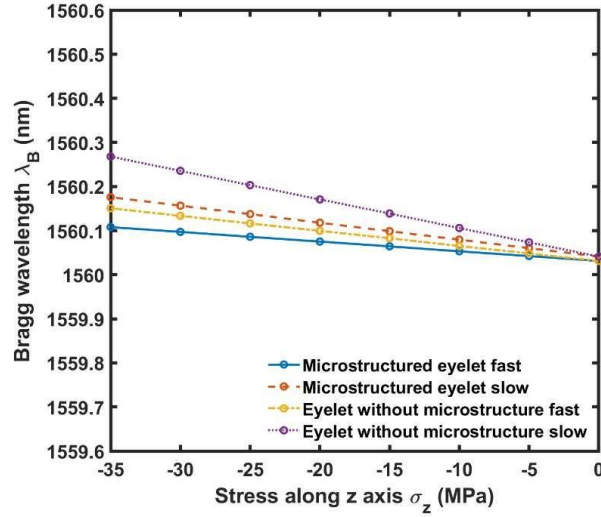
Figure 3.8   Simulated Bragg wavelength λ_B versus the transverse stress σ_z; fast axis microstructured eyelet (continuous blue), slow axis microstructured eyelet (orange dashed), fast axis eyelet without microstructure (yellow dash dotted), slow axis eyelet without microstructure (purple dotted). Grating characteristics: $\Lambda = 0.5349\ \mu m$, $\Delta n_{FBG} = 3 \times 10^{-4}$, $L = 2000\ \mu m$ [40].

In literature, different approaches were proposed to this aim: i) multiple sensors embedded in the composite material or different positioning of sensors for longitudinal, in-plane, and out-of-plane monitoring [32], [212]; ii) multiple FBGs in a single polarization-maintaining optical fiber, one shielded by a capillary to reduce transverse strains [211]; iii) multiple FBGs operating at different wavelengths [209]. In such cases, the need for precise control over fiber rotation or mode polarization orientation during embedding reduces practicality. The strength of the proposed microstructured flat optical fiber lies in its ability to function without requiring exact orientation control. In addition, by inscribing a series of FBGs, it becomes possible to map strains with high spatial resolution

through wavelength division multiplexing. As a result, the microstructured flat fiber offers a practical solution for multiaxial structural health monitoring.

3.1.5 Conclusions

A novel MFOF has been designed for multiparameter sensing in CFRP lamina. The air hole microstructure pattern in one eyelet modifies the strain transfer between the composite lamina and the guiding region. This strain-transfer, combined with electromagnetic modal analysis, allows for the calculation of different transverse sensitivities for the two FBGs written in the eyelets. The key advantage of the designed microstructure is its impact on the slow and fast y-axis sensitivities: $K_{y,f} = 12.89\ pm/MPa$, $K_{y,fm} = 21.06\ pm/MPa$, $K_{y,s} = 5.02\ pm/MPa$, and $K_{y,sm} = 7.22\ pm/MPa$, enabling high sensitivity triaxial strain detection. Additionally, the flat optical fiber shape facilitates the embedding process, reducing issues related to resin-rich regions of circular optical fibers and the orientation of high birefringent optical fibers.

3.2 Effects of Curvature on Flexible Bragg Grating in Off-Axis Core: Theory and Experiment

A flexible Bragg grating based on planar technology using silica glass has been designed, manufactured via flame hydrolysis deposition, and experimentally tested for monitoring high curvatures. Both theoretical and experimental investigations clarify the sensing mechanism when the core is slightly offset from the center. Conformal mapping, modal analysis, and CMT are employed to examine the electromagnetic behavior of the proposed sensor. Experimental results show different sensitivities to positive and negative curvatures. The reflection spectrum of the planar Bragg grating sensor and the relationship between its resonant wavelengths and curvature have been measured for a wide curvature range up to $\pm\,33m^{-1}$. The following paragraphs are organized as follows: in Section 3.2.1, the simulation details; Section 3.2.2, the sensor electromagnetic design; Section 3.2.3, the sensor fabrication and characterization; Section 3.2.4, the prospects, and conclusion.

3.2.1 Simulation approach

Generally, standard optical FBG sensors have negligible sensitivity to curvature. Introducing non-symmetrical configurations, such as an off-axis core, significantly increasing the Bragg grating spectral response to curvature. Indeed, curvature induces stress distribution within an optical waveguide, altering its refractive index distribution (due to stress-optic effects), and shifting the electromagnetic mode field profile. Both these effects lead to changes in the interaction between the optical modes coupled by the Bragg grating. Conformal mapping and the well-known CMT can be exploited to study the interaction between propagating modes. The modified refractive index distribution n_s is

employed to assess the electromagnetic field distributions of the fundamental and higher-order propagating modes via 2D-FEM. The transverse electromagnetic field distributions are calculated for both straight and curved waveguides. Consequently, the electromagnetic field profile of the propagating modes shifts toward the region with higher refractive index [212]. The relationship between the Bragg grating spectral response and the curvature C can be explained using CMT. Before solving the coupled mode equations, the transverse coupling coefficients $K_t(z)$ are calculated for all propagating modes [212]. Moreover, since Bragg grating is located outside the neutral plane, the nominal Bragg grating pitch Λ_0 changes to $\Lambda = \Lambda_0(1 + \epsilon_z)$. Generally, for calculating ϵ_z, x_{proj} corresponds to the distance between the center of the Bragg grating and the neutral plane, defined as core offset d (more details in Section 2.2) [213], [214]. However, when the distance d is small, for an accurate estimation, the shift of the electromagnetic field profile toward the region with a greater refractive index should be considered [214], [215]. The simulation approach employed for the design is summarized as follows: conformal mapping method for refractive index computation of the equivalent waveguide, 2D-FEM to obtain the electromagnetic mode profile and effective refractive index in the equivalent waveguide, coupling coefficient $K_t(z)$ calculation [216], and implementation of the CMT as a boundary value problem. This procedure is iterated for each wavelength λ and for each curvature value C.

3.2.2 Design of the sensor

An opto-mechanical design is carried out to investigate the response of a curvature sensor with a slightly off-axis core position. Planar technology is selected to avoid considering the effect of torsion.
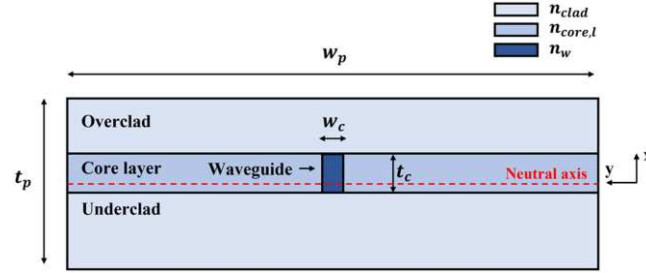
Figure 3.9   Sketch of the designed planar Bragg grating sensor. The waveguide in which the grating is inscribed (blue colored) is written in the central core layer and it is slightly off-axis with respect to the neutral axis [60].

The geometric and physical parameters are feasible with available technology, e.g. flame hydrolysis deposition and physical machining [217]. The effect of electromagnetic mode profile shift is emphasized by choosing a few-mode waveguide. Figure 3.9 presents a sketch (not to scale) of the designed sensor. The core width is $w_c = 14.5\mu m$, smaller than the core thickness $t_c = 19.5\mu m$, leading to a substantial electromagnetic mode shift along the x-axis, as shown in Figure 3.10. Other geometric parameters include thickness $t_p = 57\mu m$, width $w_p = 1\ mm$, and core offset $d = 1.2\mu m$. The underclad and overclad are made of pure silica glass and have identical compositions with a refractive index $n_{clad} = 1.444$ at the wavelength $\lambda = 1570\ nm$. A step-index profile is assumed for both the core layer and the waveguide. Specifically, the refractive index of the core layer is $n_{core,l} = 1.4633$ and the refractive index of the waveguide is $n_w = 1.4713$ at the same wavelength $\lambda = 1570\ nm$. Wavelength dispersion is modeled via the Sellmeier equation for silica glass [218]. The effective refractive indices and electromagnetic field profiles of all propagating modes are simulated via FEM and considered in coupling coefficients and CMT equations. The effective refractive index of the fundamental mode is $n_{eff} = 1.4712$ at the

wavelength $\lambda = 1570 \; nm$ when no curvature C is applied. The uniform Bragg grating has a sinusoidal modulation with amplitude $\Delta n_{BG} = 2 \times 10^{-4}$ and a length $L = 12 \; mm$. The nominal grating period is $\Lambda_0 = 0.534 \mu m$. This value allows to obtain the resonant coupling around the wavelength $\lambda = 1570 \; nm$. As already mentioned in Section 2.2, curvature C shifts the electromagnetic field of the propagating modes towards the waveguide region with high refractive index. Figure 3.10 shows the shift of the electric field norm E of the fundamental mode for curvature $C = [0m^{-1}, \pm 33m^{-1}]$. The simulation is computed in the wavelength range from $\lambda = 1565 \; nm$ to $\lambda = 1574 \; nm$ with a sampling step $\Delta\lambda = 5 \; pm$. The simulated reflection spectrum when no curvature is applied is shown in Figure 3.11.
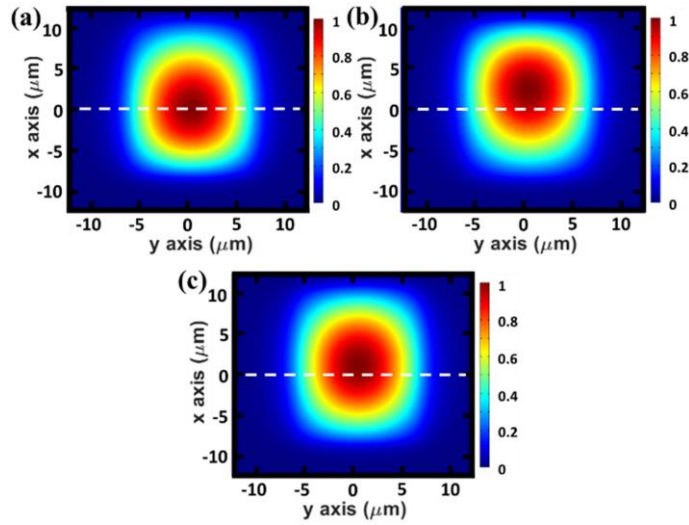
Figure 3.10 Norm of the electric field E of the fundamental mode for: (a) Curvature $C = -33 \; m^{-1}$, (b) Curvature $C = 33 \; m^{-1}$, (c) Curvature $C = 0 \; m^{-1}$ [60].

The UV-written waveguide is few-mode and four propagating modes interact with the Bragg grating, inducing four resonant wavelengths, marked as P_1, P_2, P_3, P_4, corresponding to the spatial modes $E_{11}, E_{21}, E_{31}, E_{32}$, respectively. For shortness, only one of the nearly degenerate orthogonal polarizations is shown in the inset of Figure 3.11.
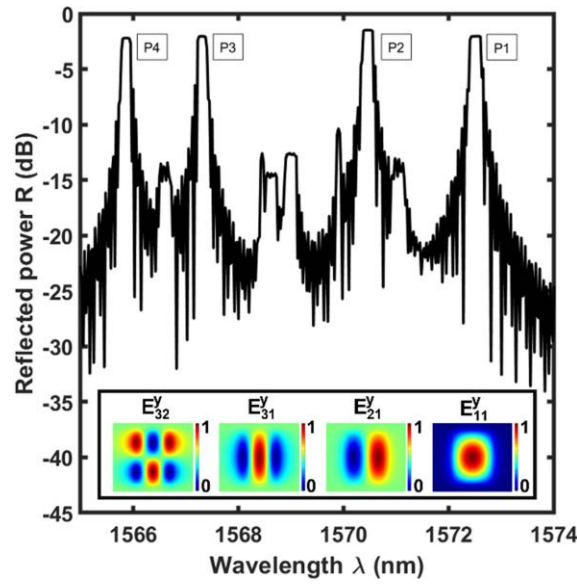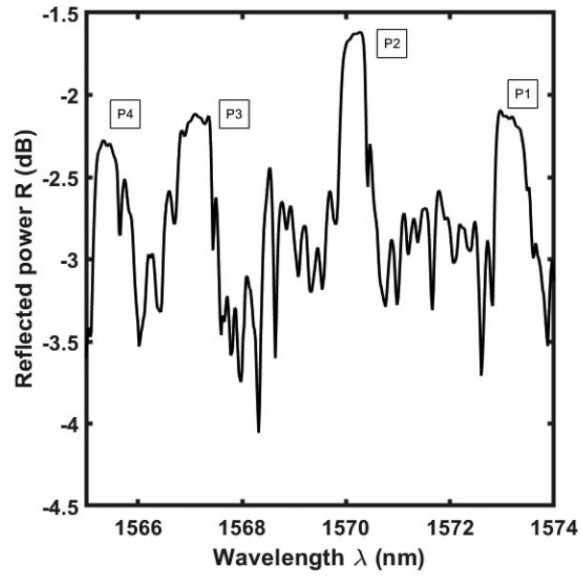

Figure 3.11   Simulated reflection spectrum of the planar Bragg grating sensor when no curvature C is applied; length of the Bragg grating $L = 12\,mm$, refractive index modulation of the Bragg grating $\Delta n_{BG} = 2 \times 10^{-4}$. In the inset, the y component of the electric field for y polarized modes $E_{11}^y, E_{21}^y, E_{31}^y, E_{32}^y$ [60].

3.2.3 Fabrication and characterization of the sensor

Flame Hydrolysis Deposition (FHD) is performed on a sacrificial p-doped [1 0 0] silicon wafer, depositing three doped silica layers—overclad, core, and underclad. Then, the silicon is removed through physical machining, leading to a flexible glass substrate with nominal thickness of 57 μm. Figure 3.12 reports a cross-sectional image of the planar sensor captured with a CCD camera and the three layers are clearly visible. DUW is used to inscribe the few-mode waveguide and the uniform Bragg grating in the core layer simultaneously. The reflection spectrum of the planar Bragg grating, measured with an optical spectrum analyzer, is shown in Figure 3.13. The planar sensor is butt-coupled to a cylindrical optical fiber using UV curable glue, as illustrated in Figure 3.14.
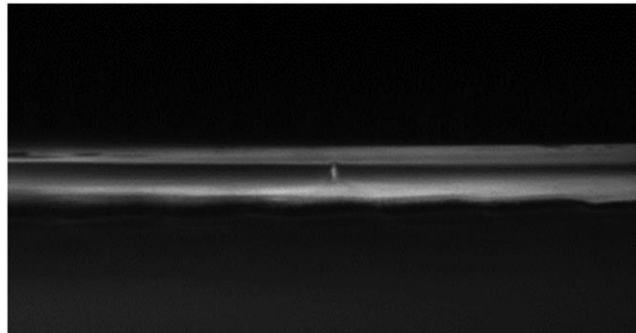
Figure 3.12   Enlargement of the cross section of the planar Bragg sensor captured via CCD camera [60].

Figure 3.13   Measured reflection spectrum of the planar Bragg grating sensor when no curvature C is applied; length of the Bragg grating $L = 12\ mm$, refractive index modulation of the Bragg grating $\Delta n_{BG} = 2 \times 10^{-4}$ [60].
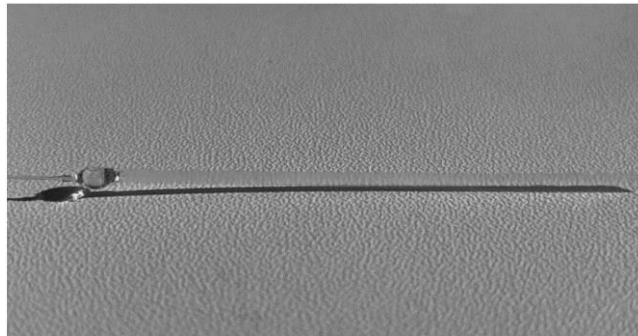

Figure 3.14   Planar Bragg sensor butt-coupled to a cylindrical optical fiber through UV curable glue [60].

Four resonant wavelengths appear in Figure 3.13 because of the few mode waveguide. The measured resonant peaks with the set-up illustrated in Figure 3.15 align well with the simulated ones.

Figures 3.16 and 3.17 show the measured Bragg wavelength shift $\Delta\lambda_B$ (black squares) as a function of curvature C for peaks P3 and P4, respectively, demonstrating good agreement with numerical results (dotted line). Both figures exhibit an almost linear response for positive curvature C values. Specifically, for positive curvature, the electromagnetic field shifts toward the outer half of the sensor, mainly experiencing tensile strain ϵ_z, which increases linearly with curvature C. The linearized sensitivity for positive curvature values is $S_{P3+} = 5.9pm/m^{-1}$ for peak P3 and $S_{P4+} = 5.2pm/m^{-1}$ for peak P4. The different sensitivities arise from the variation in effective refractive indices between the straight and curved planar Bragg grating sensor for each mode. In other words, the effective refractive index difference for peak P3 is greater than for peak P4, causing a larger Bragg wavelength shift for peak P3. As curvature C decreases to slightly negative values, the electromagnetic field shifts toward the center of the planar sensor and is affected by compressive strain ϵ_z. When curvature C is around $-23\ m^{-1}$, the electromagnetic field intersects the neutral plane, where principal axis strains are zero, resulting in zero sensitivity. With more negative curvature, the electromagnetic field marginally extends beyond the neutral plane, encountering tensile strain ϵ_z. Thus, the combined effects of cross-sectional refractive index changes and tensile strain ϵ_z on the grating period Λ cause a reversal of the slope. In summary, for positive curvature values, the electromagnetic field shifts toward the device outer half with increasing tensile strain ϵ_z; for negative curvature values, it shifts from the inner half, where compressive strain ϵ_z occurs, to the outer half, where tensile strain ϵ_z is present, see Figure 3.10.
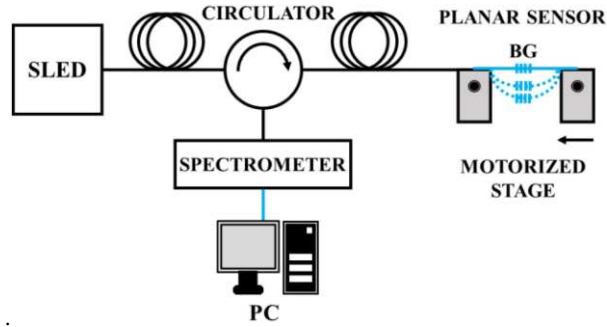
Figure 3.15 Experimental set-up adopted for the curvature measurement of the planar Bragg grating [60].
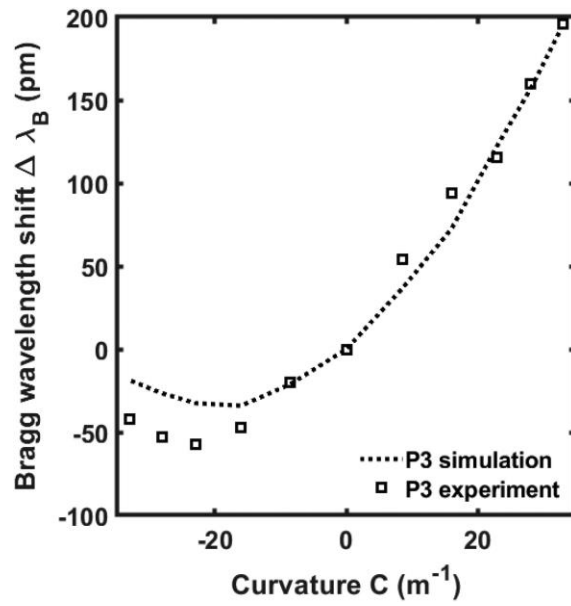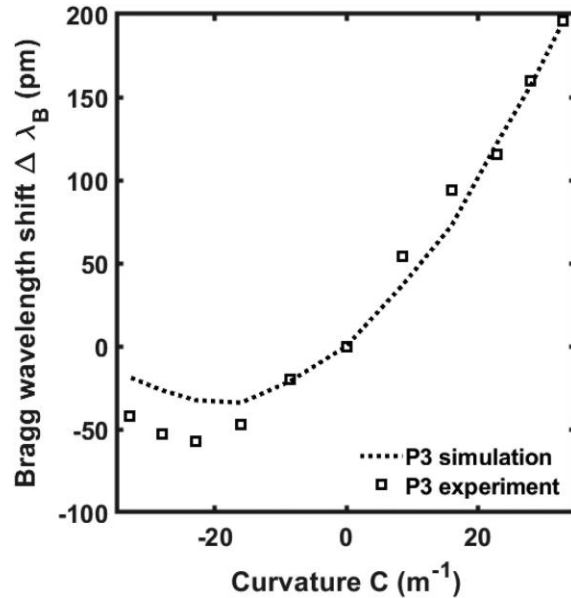

Figure 3.16 Simulated (dotted line) and measured (square markers) Bragg wavelength shift $\Delta\lambda_B$ of the resonance peak P3 for curvature $C = 0\ m^{-1}, \pm 8.5\ m^{-1}, \pm 16\ m^{-1}, \pm 23\ m^{-1}, \pm 28\ m^{-1}, \pm 33\ m^{-1}$ [60].

Figure 3.17 Simulated (dotted line) and measured (square markers) Bragg wavelength shift $\Delta\lambda_B$ of the resonance peak P4 for curvature $C = 0\ m^{-1}, \pm 8.5\ m^{-1}, \pm 16\ m^{-1}, \pm 23\ m^{-1}, \pm 28\ m^{-1}, \pm 33\ m^{-1}$ [60].

3.2.4 Conclusions

A high curvature sensor based on an ultrathin flexible silica planar Bragg grating has been proposed, designed, and characterized. The implementation of a CMT-based code explains the resonant wavelength shifts for different curvatures. Experimental results align with simulations and are reported for high curvatures up to $\pm 33\ m^{-1}$, demonstrating excellent mechanical robustness compared to traditional optical fiber solutions.

3.3 Flexible Photonic Sensors: Investigation of an Approach Based on Ratiometric Power in Few-Mode Waveguides for Bending Measurement

This section proposes using ratiometric power change in a few-mode optical waveguide as a novel method to measure bending via flexible photonics devices. To investigate this, a sensor with a Bragg grating approximately aligned to the neutral axis was designed, fabricated, and characterized. The design uses FEM, Beam Propagation Method (BPM), and CMT to simulate the electromagnetic and mechanical behavior during a three-point bending test. Experimental results demonstrate that the planar device can endure sharp curvatures without mechanical failure. As the bending increases, the reflected power from the fundamental mode decreases while the reflected power from higher-order modes increases. The measured ratiometric power sensitivity to displacement is $K_{PR} = -0.78dB/mm$, with minimal variation across a $40°C$ temperature range. The proposed sensor is suitable for multiparameter sensing, such as simultaneous temperature and curvature monitoring, by combining the Bragg wavelength shift with changes in mode optical power. A prototype of the flexible photonic curvature sensor is depicted in Fig. 3.18. The subsequent paragraphs are organized as follows: Section 3.4.1 details the electromagnetic design and mechanical investigation of the sensor; Section 3.4.2 describes the sensor fabrication and reports the comparison between the numerical and experimental results; Section 3.4.3 provides conclusions and discusses future prospects.
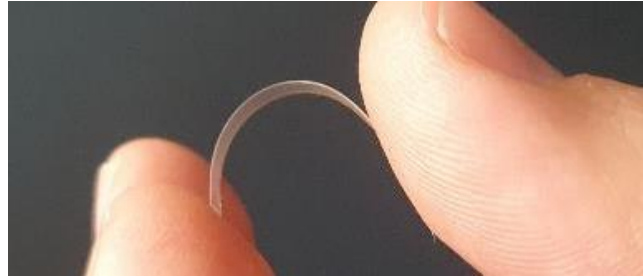
Figure 3.18   Flexible planar photonic chip in doped silica fabricated through FHD [61].

3.3.1 Electromagnetic and mechanical modelling

The flexible photonic sensor is designed using a 2D FEM electromagnetic modal analysis with the COMSOL Multiphysics® Wave Optics module. Following this, a 3D FEM analysis is conducted using the COMSOL Multiphysics® Structural Mechanics module to model the sensor under a three-point bending test. The bending test impact on the Bragg grating optical response is examined through both electromagnetic and mechanical analyses. The mechanical analysis provides key details such as the maximum displacement, curvature profile, and strain distribution. This curvature profile is then used in 3D BPM modeling with BeamProp®-RSOFT Design® to evaluate mode power mixing, complemented by CMT. Bending in multimode waveguides leads to mode coupling and changes in optical power distribution [167]. The strain distribution, electromagnetic field profile, and mode power data are input into an in-house MATLAB® code based on CMT. Three Bragg gratings—#G1, #G2, and #G3— are designed following this methodology. Particular attention is given to Bragg grating #G2, which is at the center of the flexible sensor and is subjected to nearly uniform curvature along its length. The experimental results for #G2 are

consistent with numerical simulations, explaining the sensor optical behavior alongside gratings #G1 and #G3, which are used to further understand the sensor performance and the loads.

   To assess the sensor capability to monitor both curvature and temperature, a channel waveguide with two propagating modes is designed. The flexible photonic sensor features a core layer positioned slightly off the neutral axis, optimizing dimensions to balance surface stress and electromagnetic field confinement. The sensor total thickness is $t_{fp} = 60\ \mu m$ and width is $w_{fp} = 1\ mm$. The channel waveguide is rectangular, and it is written within the core layer. Its width is $w_{wg} = 7\ \mu m$, and its thickness is identical to the one of the core layer, $t_{co} = t_{wg} = 9\ \mu m$. The core layer, $1.5\ \mu m$ offset from the central neutral axis, is surrounded by overclad and underclad layers made of identical silica glass with a uniform refractive index of $n_{cl} = 1.4452$ at a wavelength of $\lambda = 1553\ nm$. The core layer has a refractive index of $n_{co} = 1.4645$, and the channel waveguide's refractive index is $n_{wg} = 1.4695$, achieved using DUW.
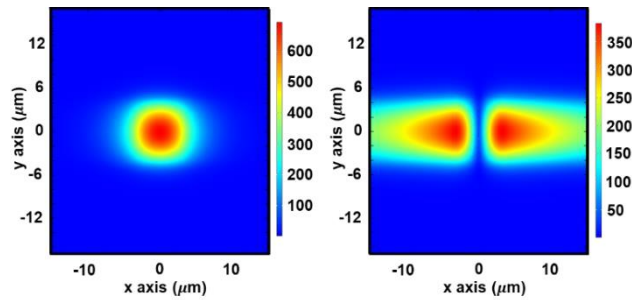

Figure 3.19   Norm of the electric field E of the fundamental E_{11} and high order mode E_{21}. The coordinates $(0;\ 0)$ refer to the center of the waveguide [61].
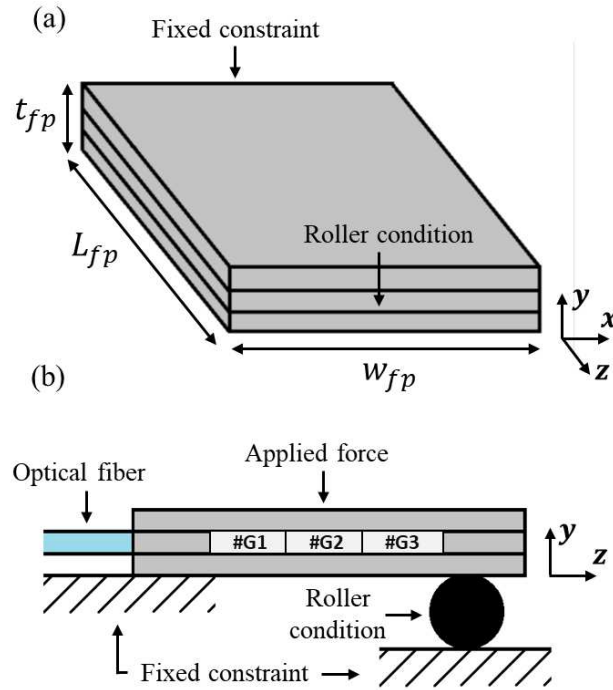
Figure 3.20 (a) Sketch of the boundary conditions and applied forces to the 3D-FEM modeled flexible photonic sensor for three-point bending test simulation; (b) schematic representation of the set-up and Bragg grating locations [61].

Both the core and waveguide have a step-index profile, with refractive index dispersion modeled using a Sellmeier equation [218]. The norm of the electric field E for both the guided modes, i.e. respectively the spatial modes E_{11}, E_{21}, is reported in Figure 3.19. For the numerical investigation of the sensor under three-point bending, a 3D model of the multi-layered glass platform with a length of $L_{fp} = 60 \ mm$ is considered. Mechanical parameters such as Poisson's ratio and Young's modulus, measured via nano-indentation, are used [212]. The

sensor boundary conditions include a fixed constraint on the left and a simply supported condition on the right, as illustrated in Figure 3.20. A force is applied perpendicularly to the sensor longitudinal axis, with values $F_i = [0\ mN, 3.3\ mN, 6.6\ mN, 9.8\ mN, 12\ mN]$ with $i = 1 \rightarrow 5$. The simulation results show good agreement with classical beam theory and the simulated maxima displacements are respectively $d_{sim} = [0\ mm, 3\ mm, 6\ mm, 9\ mm, 11\ mm]$, as can be seen in Figure 3.21 for F_5. The curvature radius, calculated from the displacement profile, is used in 3D BPM modeling to assess mode power mixing. For instance, Figure 3.22 reports the curvature radius C_R versus the cumulative arch length S considering the applied force F_5.

Conformal mapping in 3D-BPM helps modeling the refractive index changes due to bending by comparing a curved waveguide to a straight one with a modified cross-sectional refractive index. The 3D-BPM approach does not account for strain-induced refractive index changes, which are considered separately using stress-optic relations in 2D-FEM. The simulation also includes a Gaussian beam profile to model butt coupling with a single-mode optical fiber. Finally, the power mode mixing can be inferred. In particular, by considering the maximum displacement $d_{sim} = 11\ mm$, the power mode mixing investigation for the grating #G2 demonstrates that the simulated peak power $P_{s,hom}$ of the high order mode increases of $\Delta P_{s,hom} = 3.4\ dBm$ at the expense of the peak power $P_{s,fun}$ of the fundamental mode.

The 2D-FEM modal analysis incorporates stress-optic relations and strain distributions from the 3D-FEM model. The designed uniform Bragg grating has a sinusoidal modulation with an amplitude $\Delta n_{BG} = 2 \times 10^{-4}$ and a length $L = 12\ mm$. The nominal grating period of #G2, when the planar sensor is

not subjected to curvature, is $\Lambda_{\#G2} = 0.51774\,\mu m$. CMT is used to compute coupling coefficients and reflection spectra, with wavelength ranges and grating parameters carefully selected to match the modes resonant wavelengths. Simulated reflection spectra for Bragg grating #G2, reported in Figure 3.23, show a maximum Bragg wavelength shifts of $\Delta_{\lambda s,fun} = -250\,pm$ for the fundamental mode and $\Delta_{\lambda s,hom} = -240\,pm$ for the higher-order mode.
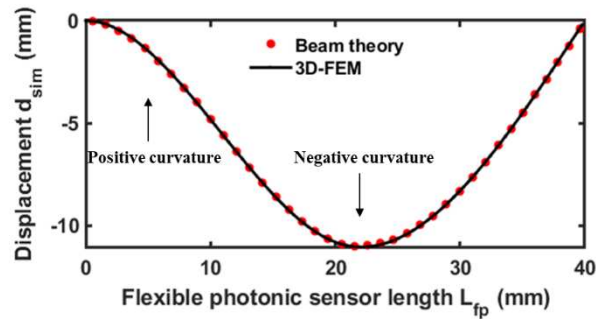

Figure 3.21   Displacement profile as a function of the flexible photonic sensor length L_{fp} considering the applied force F_5 [61].
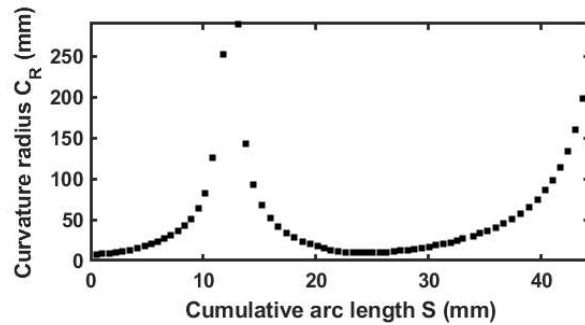

Figure 3.22   Curvature radius C_R vs cumulative arch length S considering the applied force F_5 [61].
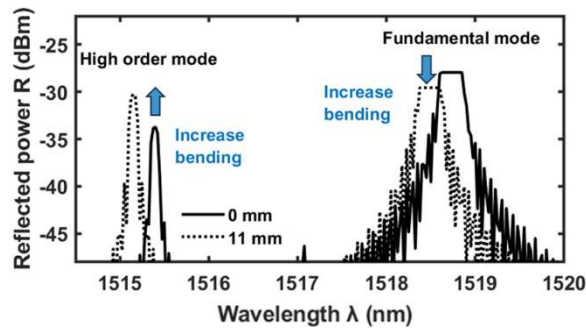
Figure 3.23 Simulated reflection spectrum of the Bragg grating #G2, unperturbed (solid curve) and with displacement $d_{sim} = 11\ mm$ (dotted curve); length of the Bragg grating $L = 12\ mm$, refractive index modulation of the Bragg grating $\Delta n_{BG} = 2 \times 10^{-4}$ [61].

3.3.2 Fabrication and characterization

The flexible glass substrate is obtained via FHD, which involves depositing three doped silica layers (overclad, core, and underclad) sequentially onto a rigid silicon wafer (diameter $d = 152\ mm$, thickness $t = 1\ mm$, p-doped [100]). The silicon has a thermally grown wet oxide layer to prevent chemical reactions between the silica layers and the silicon. Equal compositions for the underclad and overclad layers balance stress differentials and reduce bending when the substrate is removed. The deposition flow rates are SiCl$_4$ at 137 $sccm$, BCl$_3$ at 70 $sccm$, and PCl$_3$ at 31 $sccm$ for the cladding layers, and SiCl$_4$ at 123 $sccm$, GeCl$_4$ at 130 $sccm$, and BCl$_3$ at 16 $sccm$ for the core layer, all through a hydrogen-oxygen flame. High-temperature consolidation is performed at 1360 °C for the core layer and 1250 °C for the cladding layers. The final step involves removing the silicon substrate through physical machining. The fabricated device cross-section is shown in Figure 3.24 (a). The flexible photonic sensor measures

approximately $1\,mm$ in width, $58\,\mu m$ in thickness, and $60\,mm$ in length, with the core layer offset from the neutral axis. The core layer thickness slightly differs from the target due to dopant diffusion. Figure 3.24 (b) shows the sensor coupled with a single-mode polarization-maintaining optical fiber using UV-cured adhesive. The refractive indices, measured at $\lambda = 1553\,nm$, are $n_{cl} = 1.445$ for the cladding layers and $n_{co} = 1.469$ for the core layer. The DUW technique inscribes the channel waveguide and three Bragg gratings within the core layer, located at different positions along the device length.
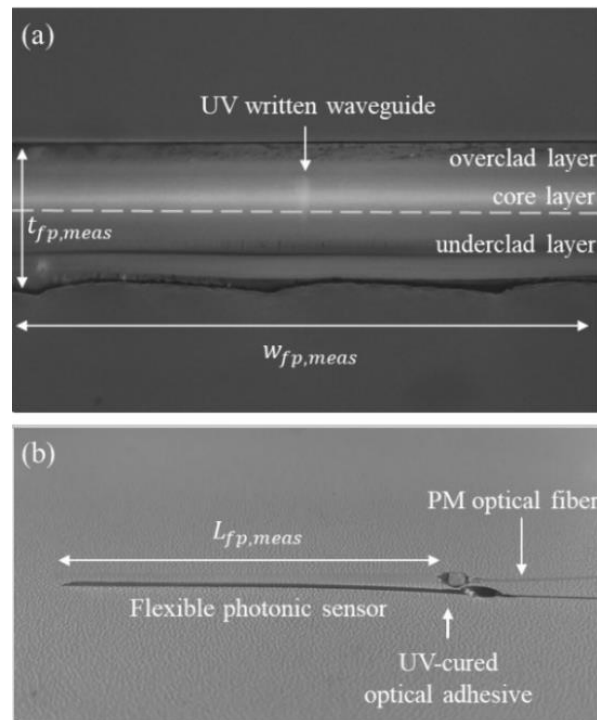

Figure 3.24 (a) Cross-section of the flexible photonic sensor captured via microscope camera; (b) flexible photonic sensor coupled to a polarization maintaining optical fiber via UV-cured optical adhesive [61].

The gratings, each $12\ mm$ long, have a uniform apodization profile with a modulation of $\Delta n_{BG} = 2 \times 10^{-4}$ and are pseudo-randomly ordered. The resonant wavelengths for the fundamental mode are $1528\ nm$, $1519\ nm$, and $1588\ nm$ for gratings #G1, #G2, and #G3, respectively. Figure 3.25 shows the reflected power versus wavelength for the unperturbed gratings, with each supporting two resonant peaks.
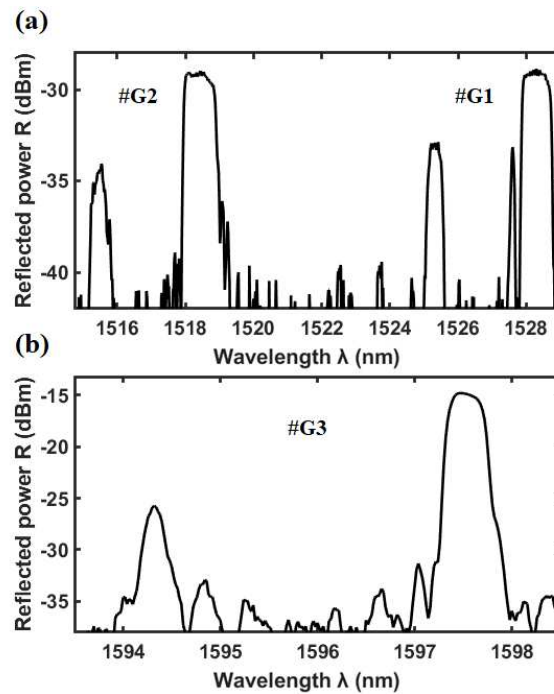

Figure 3.25 Measured reflection spectra of the unperturbed Bragg gratings (a) #G1, #G2 and (b) #G3; length of the Bragg grating $L = 12\ mm$, refractive index modulation of the Bragg grating $\Delta n_{BG} = 2 \times 10^{-4}$ [61].
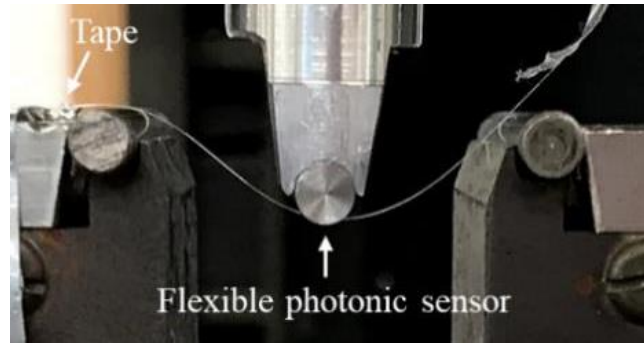
Figure 3.26   Photograph of the experimental set-up. Centre-to-centre separation of rollers $s = 20\ mm$, diameter of rollers $d_{roll} = 6\ mm$ [61].
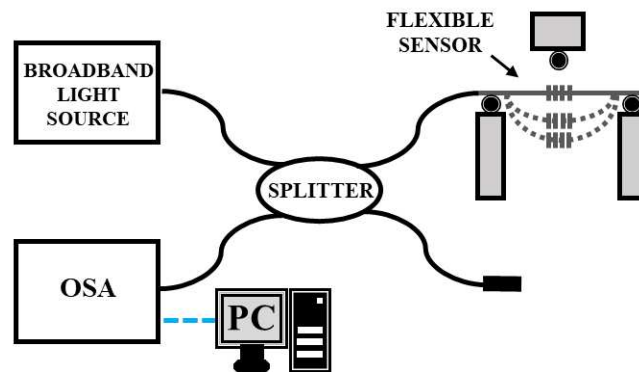

Figure 3.27   Experimental set-up employed for spectra measurements [61].

The flexible photonic sensor was tested using a three-point bending setup with an Instron E1000 electromechanical machine, as illustrated in Figure 3.26. The sensor was incrementally displaced from $0\ mm$ to $11\ mm$. During testing, a negative Bragg wavelength shift in the pm range was observed. Grating #G2, at the loading point, showed the largest wavelength shifts due to maximum curvature. The measured Bragg wavelength shifts were $-264\ pm$ for the fundamental mode and $-223.5\ pm$ for the high-order mode, with a peak power

increase of $4\ dBm$ for the high-order mode at $11\ mm$ displacement. Optical measurements of grating responses for displacements from 0 to $11\ mm$ are taken with the set-up summarized in Figure 3.27. Figures 3.28 (a) and (b) show wavelength shifts for gratings #G1 and #G3, while Figures 3.28 (c) and (d) compare simulated and measured shifts for grating #G2.
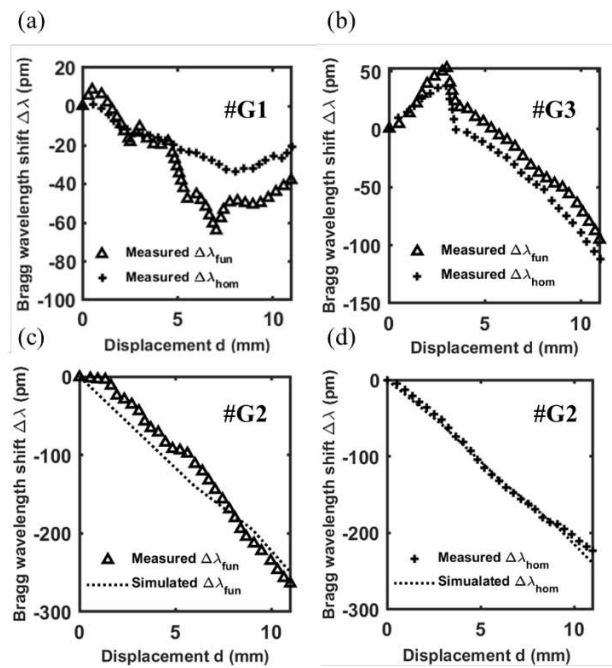

Figure 3.28   Measured Bragg wavelength shifts $\Delta\lambda_m$, of the fundamental mode (triangle markers), high order mode (cross markers) for (a) the gratings #G1 and (b) #G3. (c) Comparison between the simulated (dotted curve) and measured (triangle markers) Bragg wavelength shift $\Delta\lambda_{fun}$ of the fundamental mode, (d) comparison between the simulated (dotted curve) and measured (cross markers) Bragg wavelength shift $\Delta\lambda_{hom}$ of the high order mode, for the grating #G2 [61].

The results align well with experiments, showing that grating #G2 experiences the largest wavelength shifts due to constant negative curvature. Grating #G1, with two curvatures of opposite signs, shows a maximum shift of $-38\,pm$ for the fundamental mode and $-20.6\,pm$ for the high-order mode. Grating #G3, located where strains are lower, has maximum shifts of $-95.2\,pm$ and $-112\,pm$, respectively. Grating #G2 provides sensitivities of $-2.4\,pm/m$ for the fundamental mode and $-2.1\,pm/m$ for the high-order mode.

Figure 3.29 depicts the peak power change for the high-order mode of gratings #G1, #G2, and #G3. The simulated peak power change for grating #G2 matches the measured value, with all gratings showing maximum power changes at $6\,mm$ displacement. The power exchange between modes helps infer bending levels using the ratiometric power, which is the ratio of peak power reflected by the fundamental and high-order modes.
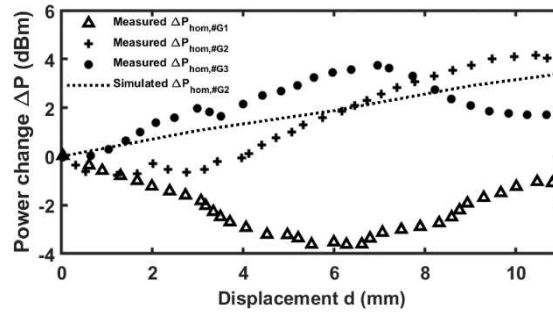

Figure 3.29 Measured peak power change $\Delta P_{m,hom}$ versus the displacement d for the high order mode of the grating #G1 (triangle markers), #G2 (cross markers), #G3 (circle markers) and simulated peak power change $\Delta P_{s,hom}$ for the grating #G2 (dotted curve) [61].
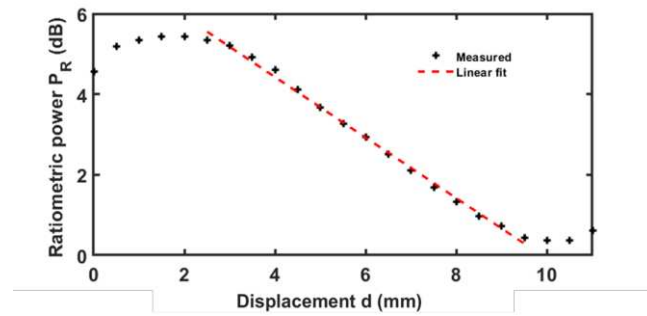
Figure 3.30   Ratiometric power P_R versus the displacement d for the grating #G2 (cross markers). The red dashed line is the linear fit of the curve [61].

Figure 3.30 shows the ratiometric power of grating #G2 versus displacement, with a linear response between $2\,mm$ and $10\,mm$ and a sensitivity of $-0.78\,dB/mm$. The response is nearly flat from $0\,mm$ to $2\,mm$ due to initial deflection. The sensor power change is unaffected by temperature variations over a $40\,°C$ range, with a thermo-optic Bragg shift sensitivity of $11.5\,pm/K$.

3.3.3 Conclusion

A new method for monitoring bending using flexible photonics is introduced, leveraging the ratiometric power ratio between the peak power reflected by the fundamental and higher-order modes and the Bragg wavelength shift. A sensor was developed to test this approach, after a detailed optomechanical design and characterization. This sensor stands out from other fiber optic curvature sensors by minimizing the substrate thickness, allowing for greater bending capability. The results reveal that the wavelength shift varies with the curvature's direction. Experimental data aligns with simulations, demonstrating that the flexible sensor can handle curvatures up to $110\,m^{-1}$. Grating #G2 shows Bragg wavelength

shift sensitivities of $-2.4\,pm/m^{-1}$ for the fundamental mode and $-2.1\,pm/m^{-1}$ for the high-order mode, with a ratiometric power sensitivity of $-0.78\,dB/mm$. The sensor exhibits minimal power variation over a $40\,°C$ temperature range, with a thermo-optic sensitivity of approximately $11.5\,pm/K$. These characteristics enable the sensor to perform both temperature and curvature measurements simultaneously, facilitating the development of advanced multiparameter sensors.

4   Mid-IR optical fiber devices

Mid-IR can be considered an enabling spectral window for environmental monitoring, healthcare, and industrial process control. In this context, the development of optical components is crucial due to lack of commercial devices. This chapter illustrates the main findings obtained during the Ph.D. research activity with respect to Mid-IR optical components, such as combiners, couplers, photonic lanterns, long period gratings, and all-fiber interferometers.

4.1   Fused optical fiber combiner based on indium fluoride glass: perspectives for mid-IR applications

An end-pump fused fiber combiner, utilizing multimode step-index fluoroindate optical fibers (InF$_3$), has been developed, produced, and tested for the first time. Given the low glass transition temperature T_g and brittleness of fluoroindate fibers, multiple trials were necessary to establish a reliable fabrication and standardization process. The results indicate consistent fabrication and no visible signs of crystallization. Consequently, this method provides a basis for developing fluoroindate-based devices. The combiner electromagnetic design was achieved through modal analysis and 3D-BPM, calculating transmission efficiency. Experimental data align with simulations, confirming the device ability to function in the Mid-IR spectral range. The paragraph is organized as follows: Section 4.1.1 reports the 3×1 fluoroindate combiner geometry and the electromagnetic design; Section 4.1.2, the fabrication challenges, the fabrication

procedure and the characterization; Section 4.1.3, reports the prospects and con-clusion.

4.1.1 Design

Key constraints in designing this optical combiner include the adiabatic taper criterion and the beam brightness principle. The electromagnetic design involves two main steps: a preliminary modal investigation of both untapered and tapered cross-sections (see Figures 4.1(a) and 4.1(b)), and the use of the BPM to assess electromagnetic power propagation and coupling.

Geometrical and physical parameters were chosen to ensure electromagnetic field confinement within a single core, at the single output, across a wavelength range from $1.00\ \mu m$ to $5.00\ \mu m$ when one of the three optical fibers is excited, and to satisfy the adiabatic taper criterion. BPM simulations were conducted to evaluate the net transmission efficiency $\eta_{s,net}(z) = P_p(z)/P_{in}$, defined as the ratio of the power along the propagation direction $P_p(z)$ to the input power P_{in} at $z = 0\ mm$, with different wavelengths λ and input Gaussian beam waists B_w. The 3×1 fluoroindate combiner comprises three multimode step-index fluoroin-date optical fibers arranged in an equilateral triangle, surrounded by a low-index fluoroindate capillary. Figure 4.1(a) presents a 3D sketch of the device. Both the optical fibers and capillary are manufactured by Le Verre Fluoré, Bruz, France. The core and cladding diameters of the fluoroindate optical fibers are approxi-mately $d_{co} = 100\ \mu m$ and $d_{cl} = 160\ \mu m$, respectively, while the capillary in-ternal and external diameters are $d_{inner,cap} = 360\ \mu m$ and $d_{outer,cap} = 580\ \mu m$. The core and cladding are made from InF$_3$ glass with different stoichi-ometries, with refractive indices of $n_{co} = 1.504$ and $n_{cl} = 1.474$ at $\lambda = 1.55\ \mu m$, resulting in a numerical aperture of approximately $NA = 0.30$. The

capillary, specifically designed and fabricated for this purpose, has a refractive index $n_{cap} = 1.472$, lower than the cladding refractive index. The dispersion curves are reported in Figure 4.2.

Figure 4.1(b) shows the longitudinal section sketch of the combiner, detailing a straight input section $L_{IN} = 1\ cm$, a linear down-taper section of $L_{DT} = 1.5\ cm$, and a waist section of $L_W = 2.5\ cm$, totaling $5\ cm$ in length. The combiner tapers from an input diameter of $580\ \mu m$ to an output diameter of approximately $d_{out} = 116\ \mu m$. This output diameter is close to the inner cladding diameters of many double cladding fibers, facilitating splicing to improve beam quality and power delivery. Figure 4.3 illustrates the refractive index profile at the output cross-section.
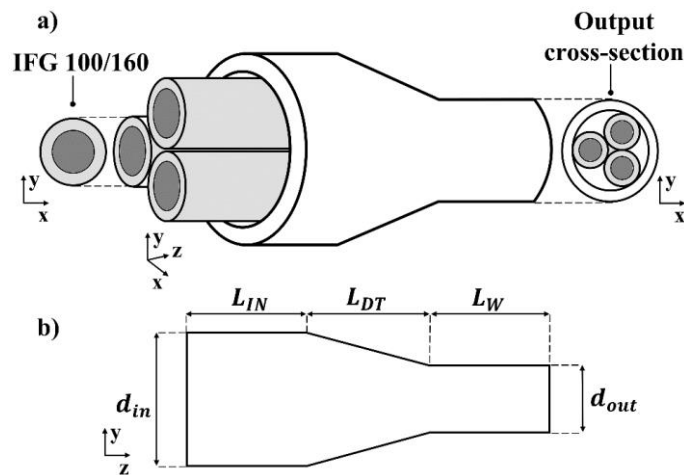

Figure 4.1   (a) 3 × 1 fluoroindate combiner sketch; (b) longitudinal section in the y-z plane of the 3 × 1 fluoroindate combiner with linear down-taper [73].

The operation of the 3×1 fluoroindate combiner was numerically investigated for wavelengths $\lambda = \{1.00;\ 1.55;\ 3.20;\ 5.00\}\ \mu m$ with a beam waist $B_w = 70.0\ \mu m$, chosen to optimize the net transmission efficiency across these wavelengths. For comparison with experimental results, the device operation at $\lambda = 1.55\ \mu m$ was also simulated with a beam waist $B_w = 10.4\ \mu m$. BPM-simulated net transmission efficiencies at $\lambda = 1.55\ \mu m$ for both beam waists are shown in Figure 4.4.
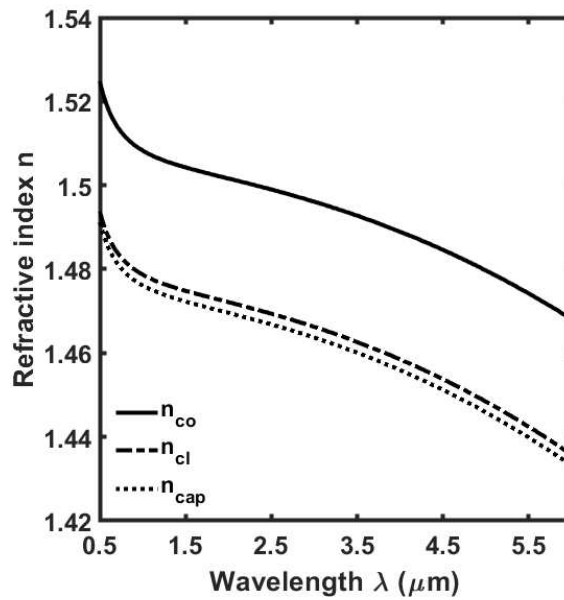

Figure 4.2   Refractive index n as a function of the wavelength λ; core refractive index n_{co} (solid line), cladding refractive index n_{cl} (dotdash line), capillary refractive index n_{cap} (dotted line) [73].
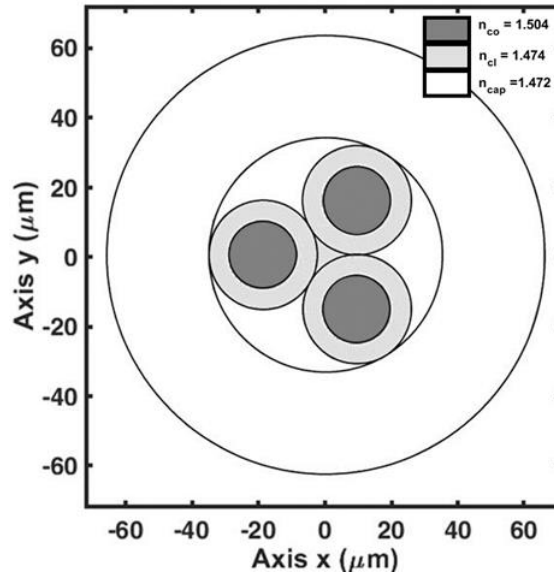
Figure 4.3   Refractive index distribution, greyscale, of the simulated 3×1 fluoroindate combiner at the output cross-section ($z = L_{out}$) at the wavelength $\lambda = 1.55 \, \mu m$ (x-y plane) [73].

The smaller beam waist corresponds to Corning SMF-28 silica optical fiber, used in NIR wavelength experiments. The results, presented in Table 4.1, confirm compliance with the adiabatic taper criterion for multimode fiber tapering, demonstrating high net transmission efficiency across a wide wavelength range from NIR to Mid-IR with negligible power losses due to tapering. The normalized frequency V value for each optical fiber at the output cross-section ensures bounding for the fundamental mode and a few higher-order modes also at the upper wavelength bound $\lambda = 5 \, \mu m$. The simulations confirm minimal power coupling between optical fibers, aligning with modal analysis results [87].

TABLE 4.1   SIMULATED TRANSMISSION EFFICIENCY

Wavelength λ [μm]	Beam waist B_w [μm]	Transmission efficiency [%]
1.55	10.4	80.1
1.00	70.0	98.2
1.55	70.0	98.2
3.20	70.0	98.2
5.00	70.0	98.1

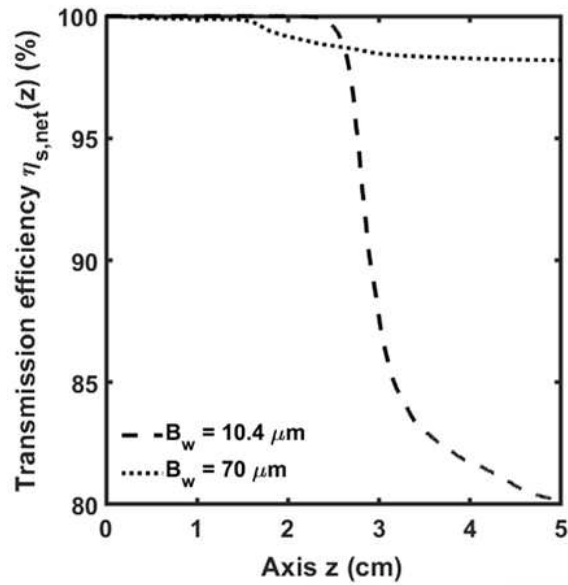
Figure 4.4   BPM simulation of transmission efficiency $\eta_{sim}(z)$ along the propagation direction (z-axis), for beam waist $B_W = 10.4\ \mu m$ (dashed line) and $B_W = 70\ \mu m$ (dotted line) at the wavelength $\lambda = 1.55\ \mu m$ [73].

4.1.2 Fabrication and characterization

The 3×1 fluoroindate combiner, described in Section 4.1.1, was fabricated using the Vytran GPX-2400 glass processing system based on graphite filament heating. Manufacturing fluoroindate glass components is challenging due to its fragility and unique thermal properties, such as a low melting temperature, narrow glass-transition, and steep viscosity/temperature profile, as can be seen in Figure 4.5. Strict temperature control is essential to avoid inhomogeneities and surface crystallization. To ensure precise temperature control, an ad-hoc normalization procedure using fluoride glass was developed for the Vytran GPX-2400. Various parameters, including filament power, applied tension, pull velocity, and argon flow rate, were optimized through extensive testing. The quality of the fluoroindate optical components heavily relies on these factors.

Before assembly, the optical fibers were stripped of their polymer coating with a stripping gel, cleaned with isopropyl alcohol, and manually threaded into the capillary. The heating source was a commercial graphite filament. Throughout the process, the glass was maintained at a temperature close to the softening point. Excessive heat could lead to surface crystallization or a fused waist, while insufficient heat could result in larger waist diameters or capillary breaking. The combiner diameter decreased during tapering, requiring a corresponding decrease in filament power to maintain the softening temperature. A constant fiber holding block pull velocity $v_{block} = 0.5 \ mm/s$ was used, with initial filament power $P_f \sim 12 \ W$. The pull velocity was controlled with a $0.1 \ s$ repetition time. The structure was pre-tensioned to $\sim 15 \ g$, and an argon flow purged the fusion region to prevent crystallization and extend filament life. Excess isopropyl alcohol was removed using a vacuum pump. During the tapering process, the vacuum pump promoted capillary collapse, ensuring a homogeneous cross-section

without trapped air. The Vytran GPX-2400 built-in sensor monitored tension to adjust parameters appropriately: reducing filament power or increasing pull velocity if tension became too small, and vice versa if tension became too large.

Figure 4.6 shows tension variations during tapering, while Figure 4.7 captures the fabrication process with a digital microscope.

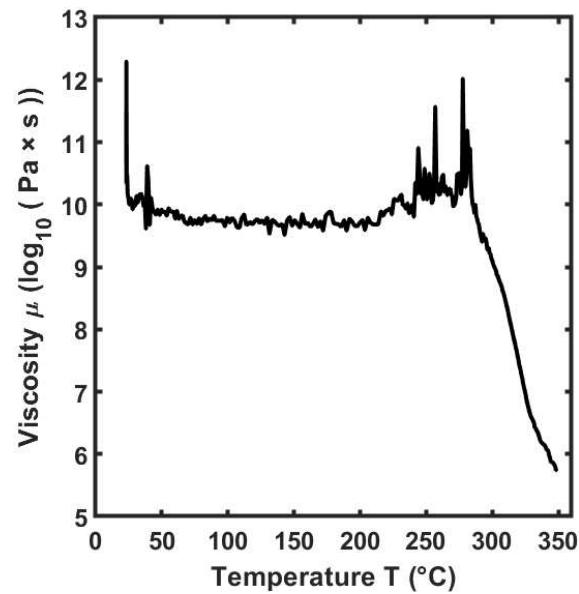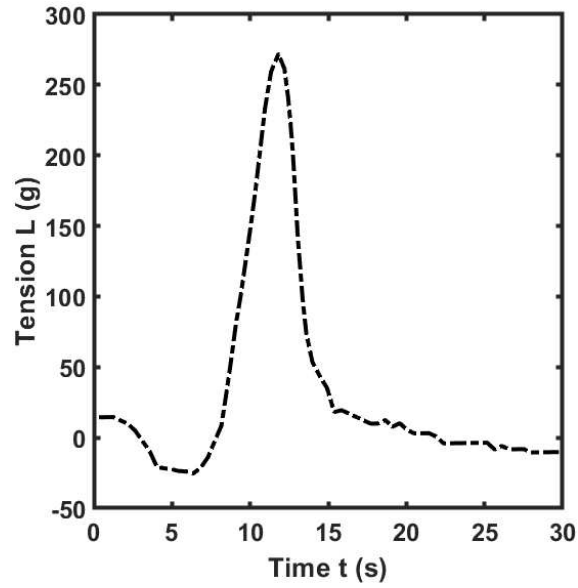Figure 4.5   Viscosity μ of fluoroindate glass versus temperature T [73].

Figure 4.6   Tension monitor measured during combiner manufacturing using Vytran GPX-2400 sensor [73].
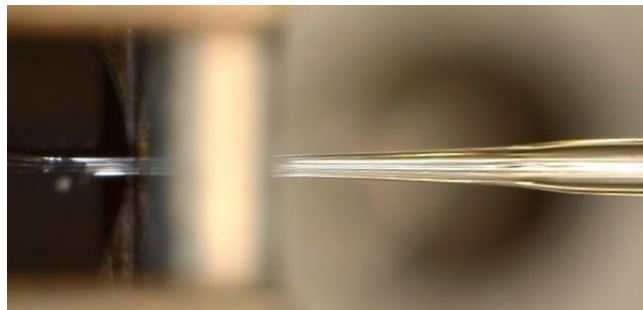

Figure 4.7   Longitudinal view of the 3 × 1 fluoroindate combiner, captured with Dino-Lite camera, during a stage of the fabrication process. At left, the FTAT3 graphite filament of the Vytran GPX-2400 workstation [73].

The final dimensions and cross-sections of the 3×1 fluoroindate combiner were obtained using the Vytran GPX-2400 microscope camera, and the device was cleaved in the waist ragion with a Vytran cleaver. Figure 4.8 shows the output cross-section, indicating that using a fluoroindate capillary with a lower melting temperature than the optical fibers, along with vacuum assistance, resulted in a homogeneous output cross-section with no air holes. Microscope images in Figure 4.9 depict the combiner longitudinal view of the down-taper. The combiner is characterized by a down-taper transition length $L_{DT} = 1.5 \, cm$, achieving the desired dimensions without surface crystallization and with a scaling factor $SF = 5$.

Two experimental setups were developed to evaluate the combiner performance in the NIR and Mid-IR spectral ranges. The first setup, Figure 4.10, included an Exalos SLED EBD-5200 light source emitting at $\lambda = 1.55 \, \mu m$, a silica single-mode $50:50$ coupler, and two Newport power meters. Bare fiber terminators connected the coupler to the fluoroindate fibers. This setup measured the per-port net transmission efficiency $\eta_{m,net}$, defined as the ratio of the output combiner power $P_{out,comb}$ to the power at the probe fiber output $P_{probe,IFG}$. Measurements for different input ports are reported in Table 4.2, showing excellent agreement with simulated efficiencies $\eta_{s,net}(L_{out})$ for a Gaussian input beam with $B_W = 10.4 \, \mu m$ at $\lambda = 1.55 \, \mu m$.

The second setup, Figure 4.11, investigated the combiner performance from $\lambda = 1.00 \, \mu m$ to $\lambda = 5.00 \, \mu m$ using a halogen lamp, Horiba iHR550 monochromator, and In-Sb-detector with a lock-in amplifier.
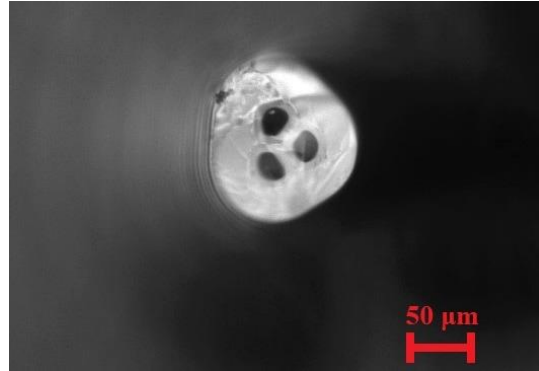
Figure 4.8   Output cross-section of the 3 × 1 fluoroindate combiner, captured with Vytran GPX-2400 microscope camera [73].
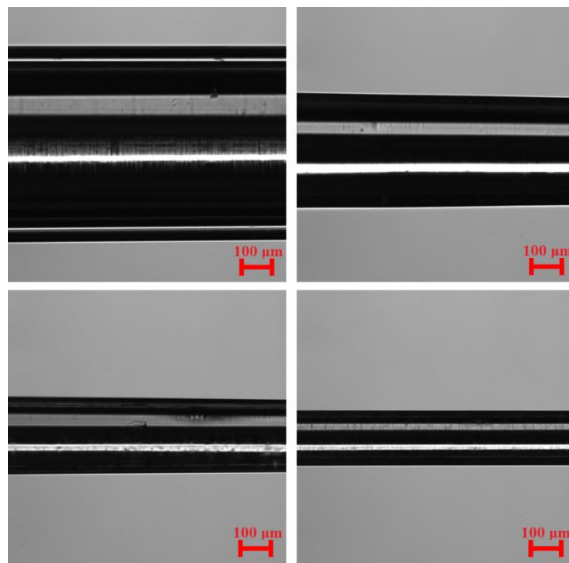
Figure 4.9   Longitudinal view of the 3 × 1 fluoroindate combiner, captured with Vytran GPX-2400 microscope camera, at different stages of the tapering process [73].

This setup measured overall transmission efficiency $\eta_{m,overall}$, including both combiner and coupling losses. Graphite inkjet applied to the combiner dissipated light power guided through the capillary. Figure 4.12 shows the overall transmission efficiency with and without graphite covering, indicating a flat behaviour from NIR to Mid-IR.

A far-field beam measurement was performed using an Ophir Pyrocam IV profiler at $\lambda = 1.55\,\mu m$, and Figure 4.13(a) shows the captured beam. Near-field measurements at $\lambda = 0.635\,\mu m$ with the Vytran GPX-2400 CCD camera are shown in Figure 4.13(b).
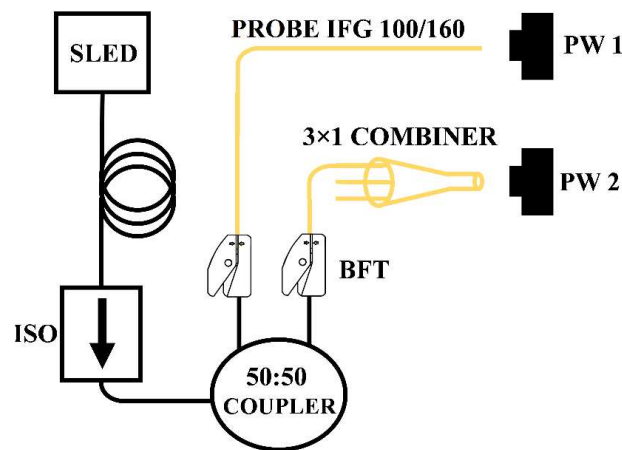
Figure 4.10   Sketch of the experimental set-up used to characterize 3×1 fluoroindate combiner transmission efficiency $\eta_{m,net}$ at the wavelength $\lambda = 1.55\,\mu m$. The silica optical fibers are represented in black, the fluoroindate optical fibers in yellow [73].

TABLE 4.2   MEASURED AND SIMULATED TRANSMISSION EFFICIENCY AT $\lambda = 1.55\ \mu m$

Parameter	Output power [μm]	Measured Transmission efficiency [%]	Simulated Transmission efficiency [%]
P_1	1.513	78.4	80.1
P_2	1.555	80.6	80.1
P_3	1.497	77.6	80.1
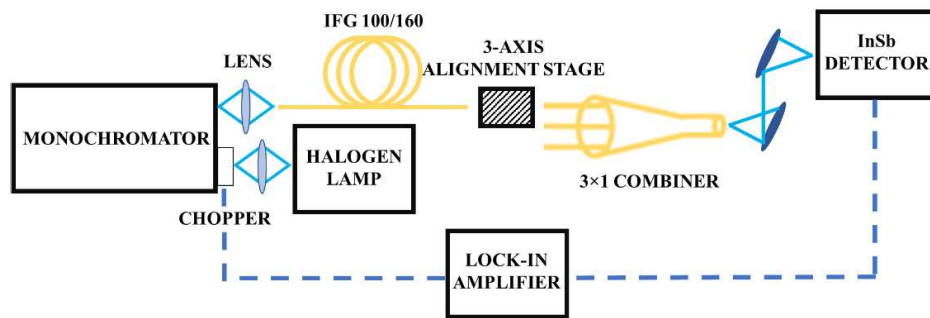
Figure 4.11   Schematic of the experimental set-up used for 3×1 fluoroindate combiner characterization from NIR to Mid-IR [73].
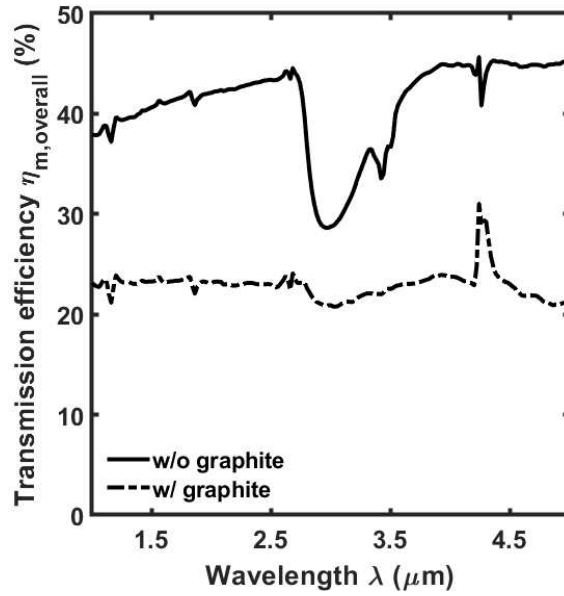
Figure 4.12 Overall transmission efficiency $\eta_{m,overall}$ measured in the Mid-IR wavelength range; 3×1 fluoroindate combiner without graphite covering (solid line), with graphite covering (dotdash line) [73].
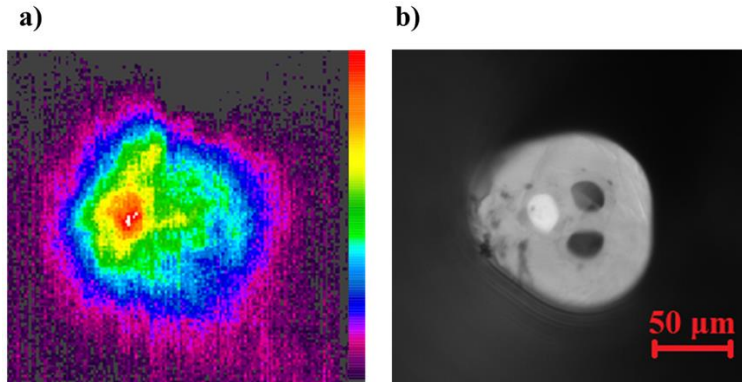
Figure 4.13 (a) Far-field measurement of the beam at the output of the 3×1 fluoroindate combiner captured with the camera beam profiler Ophir Pyrocam IV at the wavelength $\lambda = 1.55\,\mu m$; (b) near-field measurement of the beam at the output of the 3×1 fluoroindate combiner captured, at the wavelength $\lambda = 0.635\,\mu m$, by the CCD microscope camera of the Vytran GPX-2400 [73].

4.1.3 Conclusion

A 3×1 fluoroindate combiner for the Mid-IR wavelength range has been designed and fabricated. A customized fabrication and normalization technique using the Vytran GPX-2400 glass processing system was developed. This achievement marks a significant step towards the reliable production of fused glass components based on optical fibers made of soft glasses. Characterization at $\lambda = 1.55\,\mu m$ showed a maximum per-port net transmission efficiency of $\eta_{m,net} = 80.6\%$, consistent with simulations. This work facilitates the fabrication of high-quality, low-loss fluoroindate fiber combiners using commercial glass workstations, enabling wavelength and power scaling and eliminating the need for bulk optics components and free-space optical setups.

4.2 Low-Loss Fluoride Optical Fiber Coupler for Mid-Infrared Applications

Utilizing indium fluoride optical fibers, an optical fiber coupler is designed using CMT, fabricated through fused biconical tapering, and characterized. The fabrication process is carried out using the Vytran® GPX-2400 glass processing system. The fabricated 2×2 coupler shows minimal surface crystallization. Experimental results closely match simulations, demonstrating the feasibility of reproducible, low-loss fused optical fiber components for operation in the Mid-IR range. In particular, the fabricated 2×2 optical fiber coupler with few-mode fibers exhibits a measured coupling ratio $CR = 72.2:27.8$ at the wavelength $\lambda = 3.34~\mu m$, and an excess loss $E_L = 0.88~dB$ at the same wavelength. The following sections are organized as follows: Section 4.2.1, reports the electromagnetic design via CMT; Section 4.2.2, the fabrication process and the characterization in the Mid-IR spectral range; Section 4.2.3, the conclusion.

4.2.1 Design

The electromagnetic design of the 2×2 indium fluoride optical fiber coupler, sketched in Figure 4.14, was performed using CMT to accurately predict the through and cross port powers for various waist geometries (i.e. waist diameters and waist length). The designed coupler utilizes two step-index indium fluoride fibers IFG MM (0.20) 28/100 from Le Verre Fluoré (Bruz, France), each with a core diameter $d_{co,i} = 28~\mu m$ and a cladding diameter $d_{cl,i} = 100~\mu m$. These fibers are placed inside a fluoroindate capillary with a low refractive index, facilitating close contact, increasing the coupler robustness,

and easing the fusion process due to the larger cross-sectional area, which makes controlling fabrication parameters easier. The capillary inner diameter is $d_{in-cap,i} = 360 \ \mu m$, and its output diameter is $d_{out-cap,i} = 550 \ \mu m$.
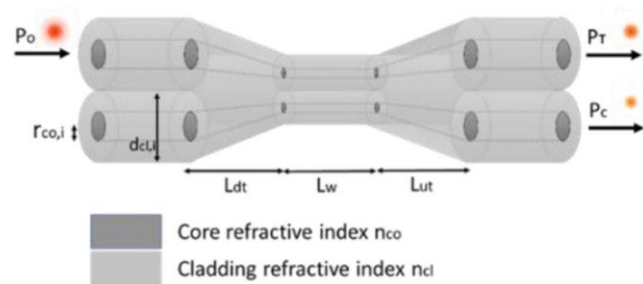
Figure 4.14   Sketch of an optical fiber coupler fabricated via fused biconical tapering technique; the input power P_0 is split among the through port and the cross port, according to the physical and geometrical properties of the waist/coupling region, long L_W [71].
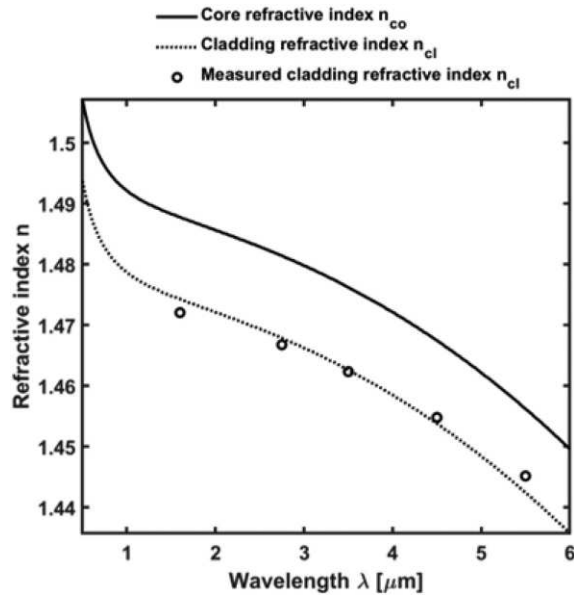
Figure 4.15 Dispersion of the core refractive index n_{co} (solid line) and of the cladding refractive index n_{cl} (dotted line) as functions of the wavelength λ [71].
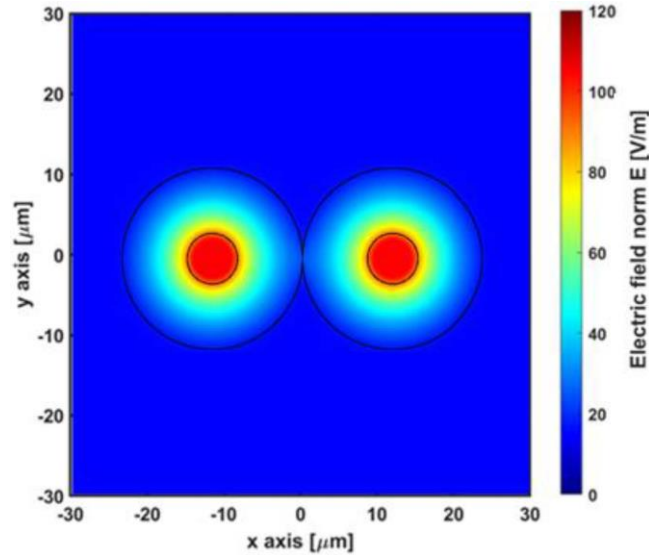
Figure 4.16   Electric field norm E of the supermode guided in the waist region; scaling factor $SF = 4.3$, supermode effective refractive index $n_{eff} \sim 1.4647$, at the wavelength $\lambda = 3.34\,\mu m$ [71].

At the wavelength $\lambda = 3.34\,\mu m$, the core and cladding refractive indices are $n_{co} = 1.4774$ and $n_{cl} = 1.4638$, respectively, yielding a numerical aperture NA of approximately 0.20. The capillary refractive index is $n_{cap} = 1.4618$ at the same wavelength.

Figure 4.15 illustrates the refractive index dispersion of the core and cladding versus wavelength λ, used in simulations. The effective refractive index of the mode guided in the waist region of each fiber, without the other fiber (hypothesis of the CMT), is $n_{eff} \approx 1.4647$, calculated using FEM.

Figure 4.16 shows the electric field norm of the supermode in the waist region (a linear combination of the HE$_{11}$ mode in each fiber) with an

effective refractive index of $n_{eff} \approx 1.4647$, illustrating field overlap. The down-taper and up-taper lengths are $L_{dt} = L_{ut} = 15\ mm$, designed to guarantee adiabatic transitions, preventing higher-order mode losses.

Figure 4.17 shows the spectral dependence of the normalized output powers of the through port P_T (solid line) and the cross port P_C (dotted line).

Figure 4.18 depicts the normalized output powers of the through port P_T (solid line) and the cross port P_C (dotted line) as functions of waist length L_W at $\lambda = 3.34\ \mu m$. The desired coupling ratio $CR = 70\!:\!30$ can be achieved with a waist length $L_W = 21.25\ mm$ and a scaling factor $SF = 4.3$, as shown in Figures 4.17-18. The optical fibers are single-mode in the waist region.
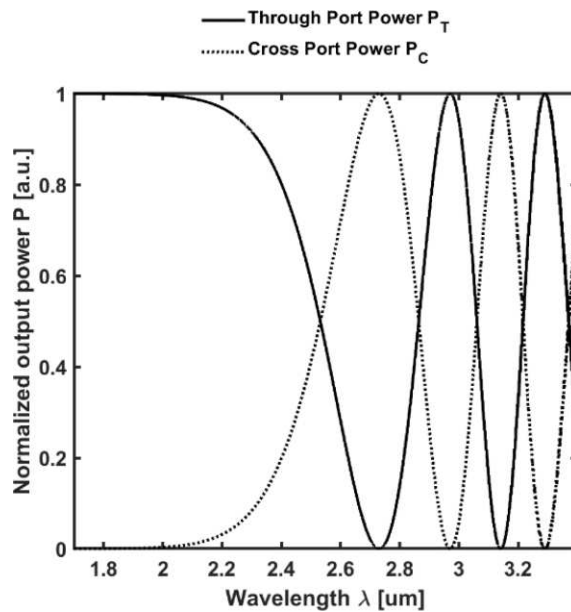
Figure 4.17 Normalized output powers of the through port P_T (solid line) and of the cross port P_C (dotted line) as functions of the wavelength λ [71].
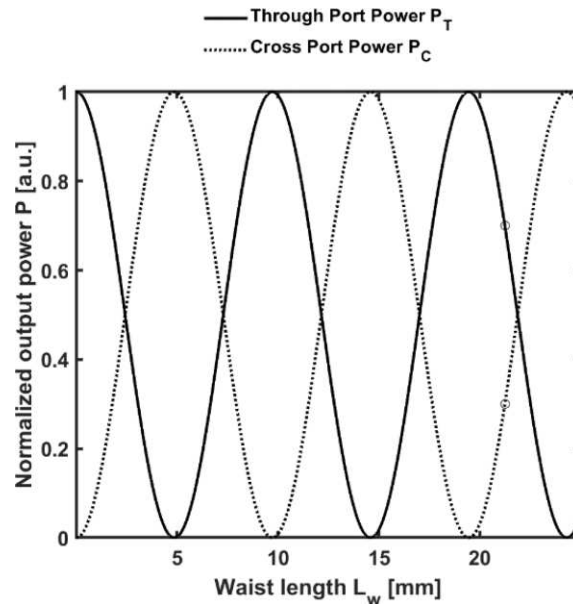
Figure 4.18 Normalized output powers of the through port P_T (solid line) and of the cross port P_C (dotted line) as functions of the waist length L_W, at the wavelength $\lambda = 3.34\,\mu m$ [71].

The design was validated via 3D-BPM (BeamProp, RSoft Design Group). A Gaussian beam was used to excite the input fiber, achieving a coincident coupling ratio CR.

4.2.2 Fabrication and characterization

Two segments of IFG MM (0.20) 28/100 optical fiber were cleaved using the Vytran LDC-400 optical fiber cleaver. The cross-sections were inspected under a microscope to ensure there were no scratches on the fiber end-facets. These fiber segments were then inserted into a low-index indium fluoride capillary, long $17\,cm$, with the aid of isopropyl alcohol. The structure was

secured in the fiber holding blocks of the Vytran GPX-2400 glass filament processing system. As already mentioned, indium fluoride glass has drawbacks such as mechanical fragility, sensitivity to temperature and humidity, surface oxidation, viscosity, and interdiffusion of core, cladding, and capillary materials. These issues can be mitigated by operating the graphite filament near the glass transition temperature $T_g = 275°C$ and heating in a controlled argon environment. The quality of the fiber coupler transition, the alignment of imposed and measured dimensions, and the drawing tension during fabrication were used to identify the correct parameters. For a fixed fiber holding block pull velocity, high filament power can cause surface crystallization or incomplete taper formation, while low power can result in large waist diameter or fiber breakage.

Figure 4.19 shows the drawing tension during fabrication, helping to identify the appropriate initial filament power. A negative peak indicates over-softened glass, while a high peak indicates insufficient softening.

Figure 4.20 shows longitudinal micrographs captured by the Vytran GPX-2400 CCD camera, demonstrating a smooth diameter reduction without irregularities in the taper profile. Minimal surface crystallization allowed for low excess loss. Avoiding crystallization in areas guiding the electromagnetic field is crucial for minimizing losses. The measured waist length is approximately $21\ mm$.
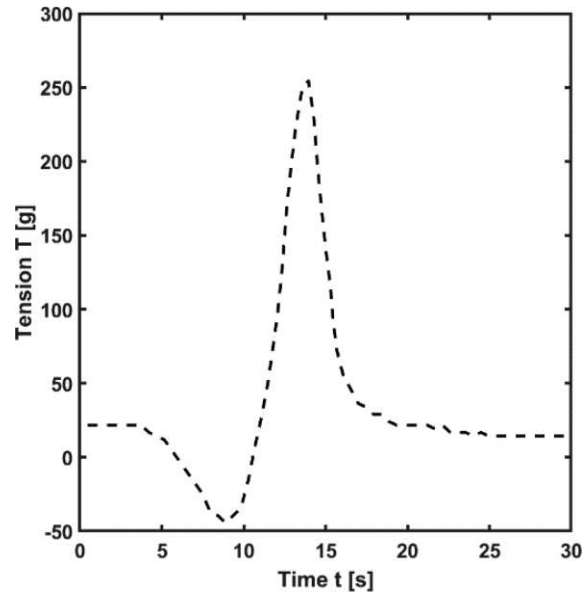
Figure 4.19   Drawing tension T as a function of the fabrication time t [71].
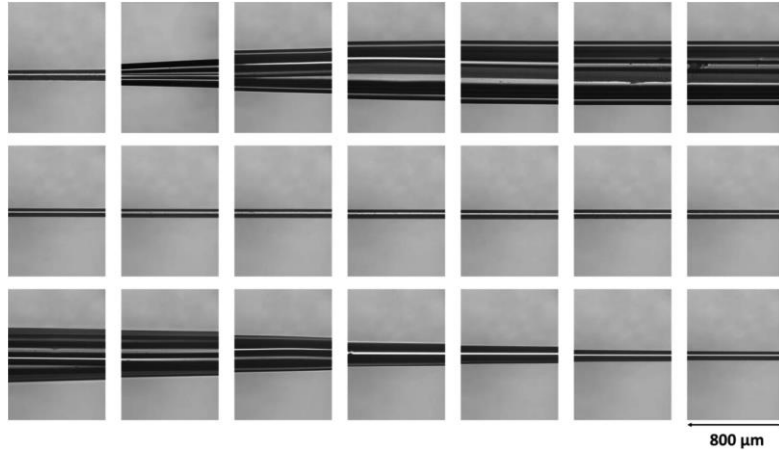
Figure 4.20 Montage of longitudinal micrographs (starting from top right, finishing to bottom left) of the fabricated 2 × 2 indium fluoride optical fiber coupler, captured via CCD camera. Each micrograph covers a length of 800 μm. Micrographs are reported with a sampling step of 1600 μm [71].

The experimental setup is shown in Figure 4.21. The fabricated device was tested using an ICL from Nanoplus Nanosystems and Technologies GmbH, Wurzburg, Germany, emitting at $\lambda = 3.34 \mu m$. The ICL was pigtailed with an indium fluoride optical fiber (IFG (0.30) 9.5/125) from Le Verre Fluoré, with a mode field diameter of 9.7 μm. Excitation was performed via free-space coupling using a groove and a three-axis stage. The through port power $P_T = 2.59 \, mW$, and the cross-port power $P_C = 1.00 \, mW$, measured by two thermal power sensors connected to a Thorlabs PM100D console. The actual coupler waist length was slightly shorter than designed, resulting in a measured coupling ratio of 72.2 : 27.8. The power injected into the input fiber was $P_{in} = 4.4 \, mW$, measured after cleaving the fiber before the down-taper region. The excess loss is $E_L = 0.88 \, dB$, including losses from mode reduction in the down-taper transition. The device was tested after one month,

showing negligible variations in excess loss and coupling ratio, confirming its stability. The coupler can be adapted for wavelengths up to 5.5 μm, the upper transparency limit of InF$_3$ glass. The performance of this and other fabricated couplers based on indium fluoride optical fibers are reported in Table 4.3.
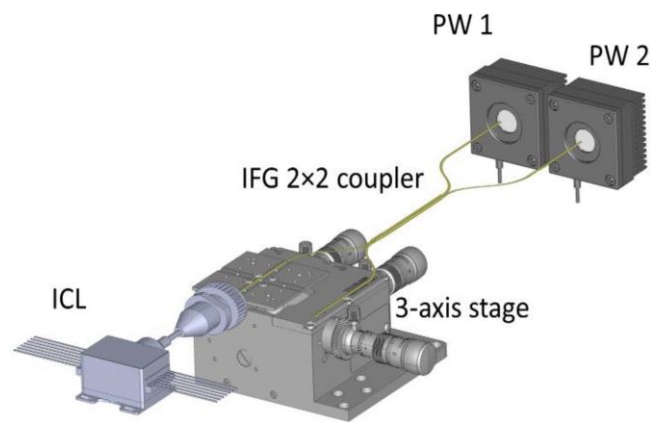
Figure 4.21 Sketch of the experimental set-up adopted to characterize the fabricated 2 × 2 indium fluoride optical fiber coupler. The ICL power is coupled in the input optical fiber of the coupler via Thorlabs MAX313D/M 3-axis stage. The cross port power P_C and the through port power P_T are measured with two thermal power sensors, i.e., PW 1 and PW 2 [71].

TABLE 4.3   PERFORMANCE COMPARISON OF THE FABRICATED INDIUM FLUORIDE OPTI-
CAL FIBER COUPLERS

Operation	Wavelength	Coupling ratio	Excess loss
Multimode	1.55 μm	85.0: 15.0	0.63 dB
Few-mode	3.34 μm	72.7: 27.8	0.88 dB
Single-mode	3.34 μm	48.1: 51.9	1.20 dB

4.2.3 Conclusion

Low-loss optical fiber couplers using indium fluoride optical fibers have been designed, fabricated, and characterized for the Mid-IR spectral range. One of the fabricated couplers shows a measured coupling ratio $CR = 72.2: 27.8$, with an excess loss $EL = 0.88\ dB$ at a wavelength $\lambda = 3.34$ μm. The experimental results align well with the simulations. Future research will focus on determining the power-damage threshold of the indium fluoride optical fiber coupler. This newly fabricated coupler promotes and advances research towards all-fiber mid-infrared applications, such as in-band pumped mid-infrared amplifiers and high-power all-fiber lasers.

4.3 Mode-Group Selective Photonic Lantern based on Indium Fluoride Optical Fibers for Mid-Infrared

A mode-group selective photonic lantern made of three indium fluoride optical fibers is designed via 2D-FEM electromagnetic modal analysis, fabricated by stretching and heating technique, and then characterized in the Mid-IR spectral region. A conventional glass processing system is employed for the fabrication, overcoming the main limitation related to the narrow temperature range for indium fluoride optical fiber processing. The experimental results are in optimum agreement with the simulations, demonstrating the possibility to selectively excite the photonic lantern modes. The following paragraphs are organized as follows: Section 4.3.1, the electromagnetic design of the photonic lantern; Section 4.3.2, the fabrication process and the characterization of the device in the Mid-IR spectral range; Section 4.3.3, the conclusion and the prospects.

4.3.1 Design

The design of a mode-group selective photonic lantern involves a 2-D electromagnetic modal analysis using commercial FEM software. This analysis allows to obtain information about the photonic lantern diameter D_{out} where the number of modes is $N_{MME} = 3$ and the mode evolution at specific points along the longitudinal transition. The computations are performed at a wavelength of $\lambda = 3.34~\mu m$. The optical fibers and customized fluoride capillary, fabricated by Le Verre Fluoré (Bruz, France), have the following refractive indices at $\lambda = 3.34~\mu m$: core refractive index $n_{co\#1} = 1.4774$ for the few-mode optical fiber #1, $n_{co\#2} = n_{co\#3} = 1.4939$ for the single-mode optical fibers #2 and #3, cladding refractive index $n_{cl} = 1.4638$ for all three fibers, and capillary refractive

index $n_{cap} = 1.4613$. The core and cladding diameters of optical fiber #1 are $d_{co\#1} = 25\ \mu m$, $d_{cl\#1} = 100\ \mu m$ while for optical fibers #2 and #3, the core and cladding diameters are $d_{co\#2} = d_{co\#3} = 7.5\ \mu m$ and $d_{cl\#2} = d_{cl\#3} = 125\ \mu m$, respectively. The capillary output diameter is $d_{cap} = 440\ \mu m$.

These fluoride optical fibers were selected for their market availability and the large propagation constant differences they offer in the photonic lantern modes, ensuring adiabaticity with short down-taper length $L_{dt} \approx 25\ mm$ [219].

Figure 4.22 shows the refractive index distribution of the starting cross-section of the designed photonic lantern, using a grey colorimetric scale where darker shades indicate higher refractive index values.
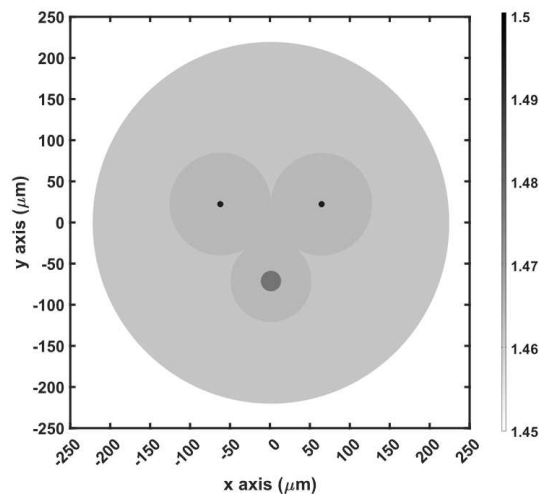
Figure 4.22   Refractive index distribution of the untapered cross-section of the designed photonic lantern, in grey colorimetric scale. The white-colored domain outside the capillary is air [219].

Figure 4.23 depicts the evolution of the effective refractive index of the first eight spatial modes against the lantern diameter D_{out}. The solid black lines represent the mode groups LP_{01} and LP_{11} (LP_{11a} and LP_{11b}). For proper operation, these should be the only modes guided at the MME. The horizontal black dash-dotted lines represent the cladding n_{cl} and capillary n_{cap} refractive indices. Solid red lines indicate cladding modes, with $n_{eff} < n_{cap}$ at the MME. As noted in [187], multimode fibers can be used for photonic lantern fabrication, relaxing the adiabaticity requirement at high wavelengths and allowing a wider range of diameters and refractive indices for achieving the desired modal selectivity.
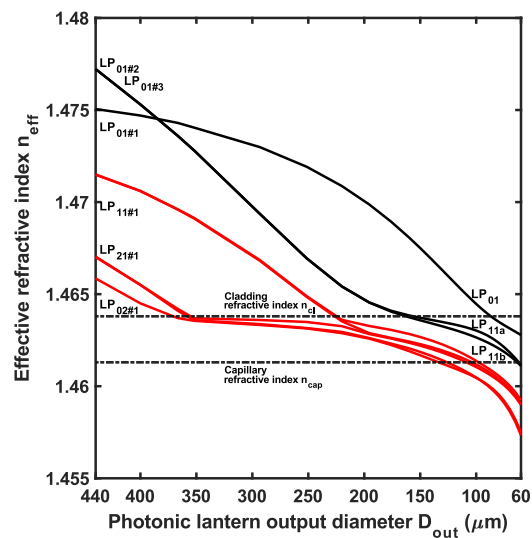
Figure 4.23 Effective refractive index n_{eff} of the first eight spatial modes at the wavelength $\lambda = 3.34\ \mu m$ of the mode-group selective photonic lantern based on indium fluoride glass, for different photonic lantern output diameter D_{out} [219].
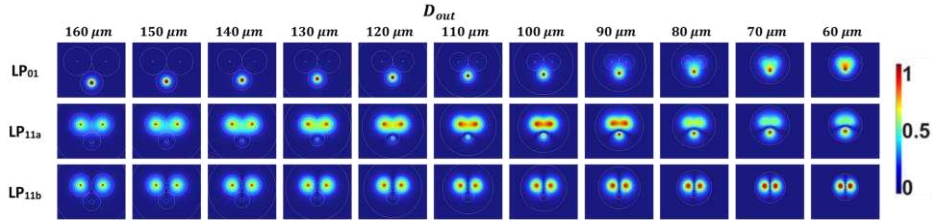
Figure 4.24   Normalized electric field norm E (V/m) of the LP_{01}, LP_{11a} and LP_{11b} propagation modes for different photonic lantern output diameter from $D_{out} = 160$ to $60\ \mu m$ [219].

In our experiment, the fundamental mode of the few-mode optical fiber #1, i.e. $LP_{01\#1}$ is preferentially excited due to the use of a single-mode pigtailed laser, and a short length of the few-mode fiber. There is a crossing between the effective refractive index curves of the fundamental mode in optical fiber #1 and those in optical fibers #2 and #3, but there is no coupling because the fundamental modes are still well-confined in the respective cores at this stage of the transition. A photonic lantern output diameter of approximately $D_{out} = 80\ \mu m$ can be considered the best as it guides only three spatial modes, far from cut-off [86].

Figure 4.24 illustrates the profile of the normalized electric field norm E for the lantern modes for various diameters ranging from 160 to 60 μm. For $440\ \mu m > D_{out} > 275\ \mu m$, the fundamental modes remain confined within each optical fiber. The mode-group selectivity condition is satisfied since, at $D_{out} = 275\ \mu m$ (where optical fibers #1, #2, and #3 are still unperturbed), $n_{eff\#1} > n_{eff\#2} = n_{eff\#3}$. When D_{out} decreases, the LP_{11} mode group emerges as a supermode from the LP_{01} modes guided in optical fibers #2 and #3.

4.3.2 Fabrication and characterization

The fabrication is similar to the procedure to obtain combiners and couplers. In

this case, optical fibers #1, #2, and #3 are cleaved using a cleaver with diamond blade and then inserted into a low refractive index indium fluoride capillary. The structure is clamped with the two fiber holding blocks of the Vytran GPX-2400 glass processing system. Experimental results indicate that the tension should be between 250 g to 600 g to prevent crystallization or structural breakage. Given the hygroscopic nature of fluoride glass, the device fabrication is carried out under Argon flow $R_{Ar} = 0.35 L/min$ to avoid high losses due to water absorption and impurity-induced crystallization. A Linicon LV-125A vacuum pump is used at the end of the capillary to assist glass collapsing and prevent the presence of air holes at the MME. Before tapering, 18 g tension is applied by moving a fiber holding block. During tapering, both fiber holding blocks move in the same direction at different speeds to achieve the necessary stretching, leading to a down-taper length of $L_{dt} = 25 mm$ and an average taper angle $\Omega = 0.41°$, which guarantees adiabaticity. Vytran LDC-400 optical fiber cleaver is again used to cleave the biconical taper in the waist region, obtaining the MME of the photonic lantern.

Figure 4.25(a) shows a picture of the fabricated indium fluoride mode-group selective photonic lantern, with the MME on the left and the three independent optical fibers on the right. Figures 4.25(b)-4.25(d) present micrographs of the cleaved cross-sections at various points along the transition of the fabricated photonic lantern (obtained via the cut-back method) and taken with a Vytran GPX-2400 microscope camera. The three optical fiber cores are clearly visible, as shown by launching visible light from a white lamp into the optical fibers.

The device is tested with the same ICL employed for the coupler operating at the wavelength of $\lambda = 3.34 \mu m$, and pigtailed with a single-mode indium fluoride optical fiber by Le Verre Fluoré. The ICL excites each of the optical fibers #1, #2, and #3 of the photonic lantern. The power at the MME ($D_{out} \approx 80\ \mu m$)

is measured by a thermal power sensor and normalized to the input power $P_{in} = 2.4 mW$. The insertion losses are $IL = 1.25\ dB$ for fiber #1, $IL = 1.63\ dB$ for fiber #2, and $IL = 1.50\ dB$ for fiber #3, accounting also for coupling losses from the ICL to the optical fibers due to imperfect mode matching.
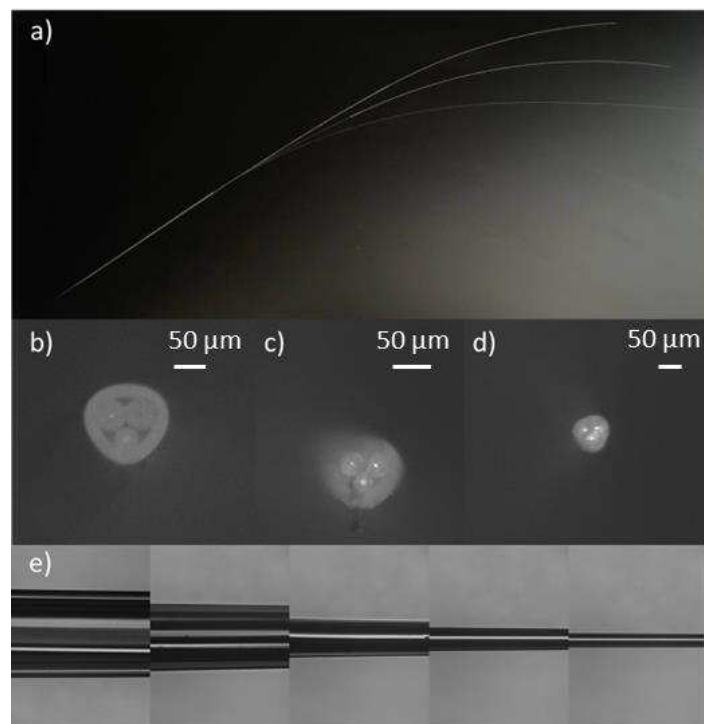
Figure 4.25   a) Picture of the fabricated indium fluoride mode-group selective photonic lantern; b)-c)-d) Micrographs of the cleaved cross-sections along the transition of the fabricated mode-group selective photonic lantern (photonic lantern output diameter: b) $D_{out} \simeq 130\ \mu m$, c) $D_{out} \simeq 100\ \mu m$, d) $D_{out} \simeq 80\ \mu m$); e) Montage of longitudinal micrographs along the transition [219].
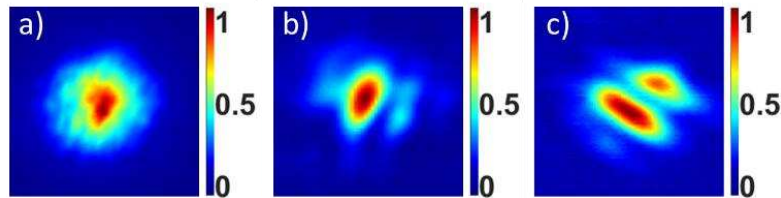
Figure 4.26   Measured normalized farfield intensity distribution at the MME of the fabricated pho-
tonic lantern, via Pyrocam IIIHR beam profiling camera; a) excitation of optical fiber
#1; b) excitation of optical fiber #2; c) excitation of optical fiber #3 [219].

Figure 4.26 shows the farfield intensity distribution at the MME for individual excitation of the optical fibers. When fiber #1 is excited, the output at the MME shows the typical quasi-gaussian LP_{01} mode profile (Figure 4.26(a)). The LP_{11} mode profile when exciting the optical fiber #2 (Figure 4.26(b)) and the optical fiber #3 (Figure 4.26(c)).

4.3.3 Conclusion

The feasibility of a Mid-IR photonic lantern using fluoride optical fibers has been demonstrated. The electromagnetic design was developed using 2D-FEM to achieve a mode-selective photonic lantern. A commercial glass processing system was employed to fabricate the device, addressing the challenges related to the thermo-mechanical behaviour of indium fluoride glass. The prototype was characterized in the Mid-IR spectral range, showing less than $IL = 1.7\ dB$ losses at the wavelength of $\lambda = 3.34 \mu m$. Modal selectivity was confirmed through measurements with a beam profiling camera at the same wavelength $\lambda = 3.34 \mu m$.

The fabricated photonic lantern has a high number of potential applications, including very large telescope interferometers, Mid-IR equipment for exoplanet

discovery, thermal radiation imaging (night vision, hot spot detection), and Mid-IR optical communication systems. Therefore, this achievement is a significant step toward the practical application of this device in Mid-IR fields, particularly in astrophotonics, imaging, and communication systems. Future research should aim to scale the photonic lantern to incorporate more fluoride optical fibers and evaluate its long-term stability under various conditions.

4.4 Micro-Tapered LPG for Mid-IR Applications

Micro-tapering technique is exploited to obtain LPGs in fluoride glass. The periodic tapering on the non-UV photosensitive zirconium fluoride optical fiber leads to LPGs characterized by a significant transmission attenuation larger than 15 dB, at the resonant wavelength. The experimental results align well with the simulations, demonstrating the possibility to adopt the devices in sensing and equalizing system. The following paragraphs are organized as follows: Section 4.4.1, the electromagnetic design of the LPG; Section 4.4.2, the fabrication process and the characterization of the device in the Mid-IR spectral range; Section 4.4.3, the conclusion and the prospects.

4.4.1 Design

The simulation is conducted on the zirconium fluoride ZFG [1.95] 6.5/125 (0.23) fiber from Le Verre Fluoré (Bruz, France), which has a core radius $r_{co} = 3.25\,\mu m$, a cladding radius $r_{cl} = 62.5\,\mu m$, and a numerical aperture $NA = 0.23$. This fiber supports single-mode operation for wavelengths above $\lambda = 1.95\,\mu m$. An equivalent model for the actual micro-tapered LPG is developed by identifying a straight LPG written in a scaled-down fiber. Thus, $r_{co-eq} = 2.60\,\mu m$ and $r_{cl-eq} = 50.25\,\mu m$ have been investigated considering their average geometrical dimension in a micro-taper. Material dispersion of zirconium fluoride glasses is included in the spectral calculations, as shown in Figure 4.27 [220]. Moreover, losses are neglected due to the short length of the LPG.

Figure 4.28 reports the electric field norm of the interacting modes, i.e. LP$_{01}$ and LP$_{02}$ modes, for the scaled-down ZFG [1.95] 6.5/125 (0.23) at $\lambda = 3180\,nm$. The computed effective refractive indices via 2D-FEM are $n_{eff} \approx$

1.4808 for LP$_{01}$ and $n_{eff} \approx 1.4780$ for LP$_{02}$. The computation assumes the domain outside the cladding is air, with a perfectly matched layer for a better estimation of the cladding modes. The imposed grating period is $\Lambda = 1.36\ mm$ and the number of grating periods is $N = 25$. Moreover, a total chirp $\Delta = 0.0095\ mm$ is considered to account for fabrication tolerances. The average dc induced refractive index changes is $n_{co}\sigma = -0.0011$ [76]. The FEM modal analysis is performed from $\lambda = 2500\ nm$ to $\lambda = 4000\ nm$ and the number of computed modes is $N = 50$.
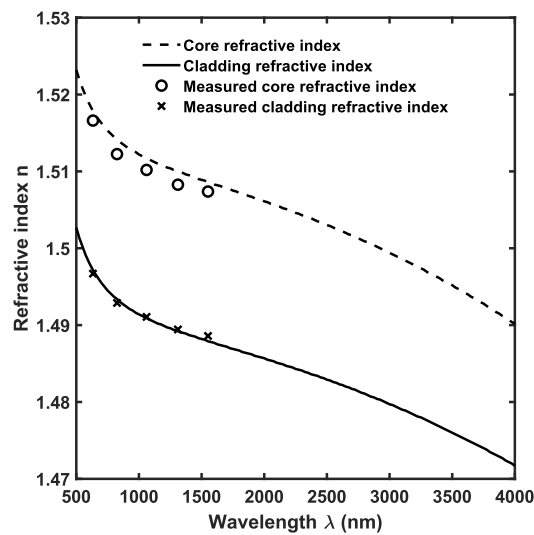
Figure 4.27   Measured and calculated core (circle markers and dashed line) and cladding refractive index (cross markers and solid line) n dispersion as a function of the wavelength λ.
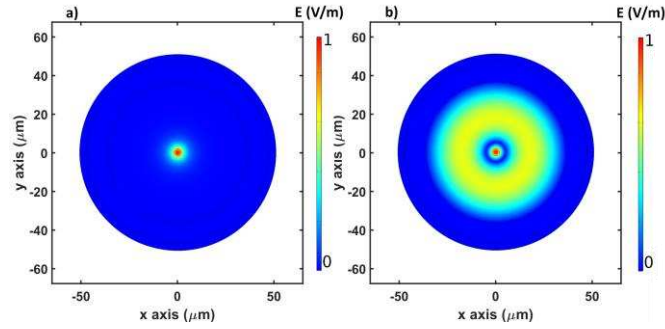
Figure 4.28   Simulated electric field norm E of the a) LP$_{01}$ mode with effective refractive index $n_{eff} \simeq 1.4808$ and b) LP$_{02}$ mode with effective refractive index $n_{eff} \simeq 1.4780$ at the wavelength $\lambda = 3180 \ nm$ for scaled down ZFG [1.95] 6.5/125 (0.23) with core radius $r_{co} = 2.60 \ \mu m$ and cladding radius $r_{cl} = 50.25 \ \mu m$.
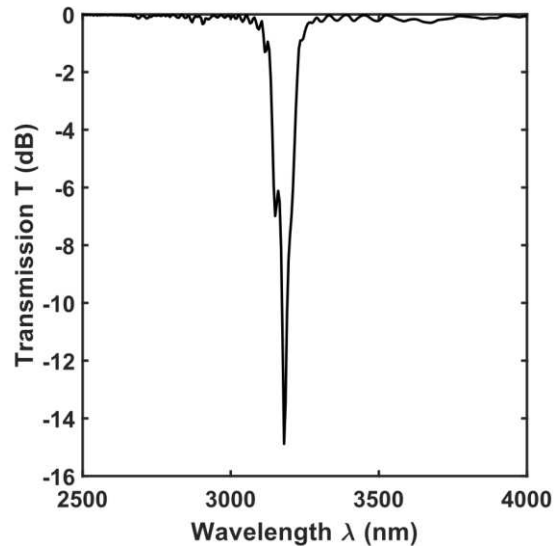
Figure 4.29   Simulated transmission spectrum T of the designed zirconium fluoride LPG.
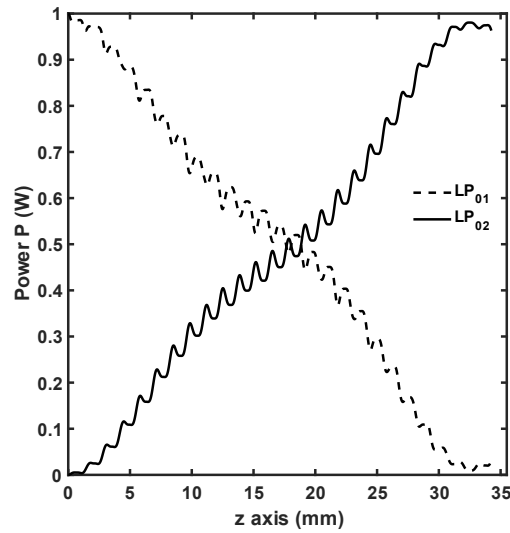
Figure 4.30   Power P of the core mode LP$_{01}$ and of the cladding mode LP$_{02}$ as a function of the longitudinal direction, i.e. z axis, at the wavelength $\lambda = 3180\ nm$.

Figure 4.29 shows the transmission spectrum T of the designed zirconium fluoride LPG. A sharp resonance with approximately $15\ dB$ attenuation is calculated at $\lambda = 3250\ nm$. At this resonance wavelength, the power of the core mode LP$_{01}$ couples to the cladding mode LP$_{02}$.

Figure 4.30 illustrates the power exchange along the grating length L between LP$_{01}$ and LP$_{02}$ at the resonant wavelength.

4.4.2 Fabrication and characterization

ZFG [1.95] 6.5/125 (0.23) optical fiber from Le Verre Fluoré (Bruz, France) is cleaved with an automatic diamond-blade cleaver and cleaned with isopropyl alcohol. The micro-tapering process involves two concurrent steps: heating and

pulling the fiber. Different geometric profiles of micro-tapers can be achieved by adjusting either the velocity of the translation stages or the heating filament power. Specifically, the amount of glass entering the heat zone must equal the amount exiting, which determines the pulling speed $v_1 = d_1^2/d_2^2 \times v_2$, where d_1 is the initial cladding diameter, d_2 is the local diameter of the tapered fiber, v_1 is the pulling speed, and v_2 is the feeding speed. Both feeding and pulling occur in the same direction but at different speeds, defining the tapering ratio. During fabrication, the graphite filament remains stationary while the fiber holding blocks move at a pulling speed of $v_1 = 100 \, \mu m/s$. After fabricating a single micro-taper, both fiber holding blocks are displaced by the same distance and, then, another micro-taper of the same dimensions is produced. The fiber is allowed to cool between taper formations to avoid residual heat effects. The distance between two micro-tapers is the grating period Λ.

Figure 4.31 shows the tension measurements during the creation of five micro-tapers. As for the other fabrications, initially, a pre-tension is applied moving one fiber holding block while maintaining the other fixed. As the glass softens, one block moves faster than the other and the tension increases to $F = 65 \, g$. Excessive tension indicates over-softening and potential crystallization in fluoride glasses, leading to high propagation losses. Insufficient tension suggests the glass is not soft enough and could be damaged.

Figure 4.32 presents longitudinal micrographs of the fabricated zirconium fluoride LPG, showing good repeatability and high-quality transitions. To absorb power from the cladding modes, a cladding mode stripper consisting of a high-index polymer is placed after the zirconium fluoride LPG. A computer vision-based code measures the cladding radius r_{cl} along the longitudinal direction z, enabling calculation of the average grating period $\Lambda = 1.36 \, mm$ and waist diameter $d_w = 89.2 \, \mu m$. The retrieved profile is reported in Figure 4.33.
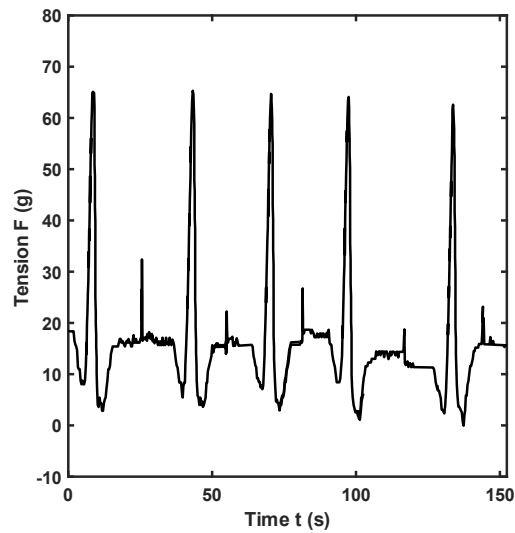
Figure 4.31 Measured cladding radius r_{cl} as a function of the z axis, i.e. longitudinal direction.
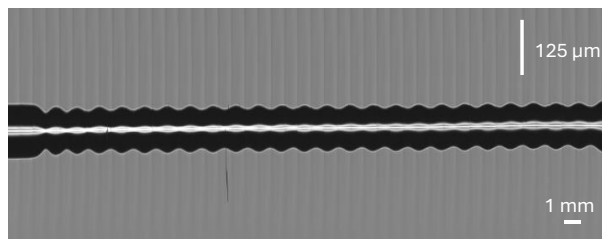
Figure 4.32 Montage of longitudinal micrographs of the fabricated zirconium fluoride LPG.

Broadband characterization of the zirconium fluoride LPGs is performed using the set-up illustrated in Figure 4.34. Light is coupled into a zirconium fluoride optical fiber segment aligned with the LPG on a triaxial stage, with end facets positioned closely together.
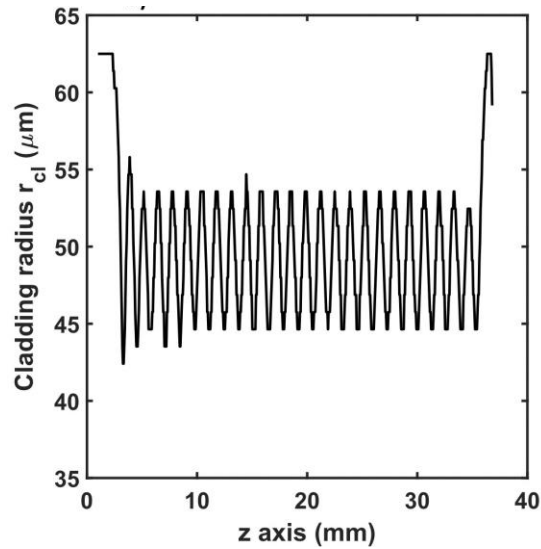
Figure 4.33   Measured cladding radius r_{cl} as a function of the z axis, i.e. longitudinal direction.
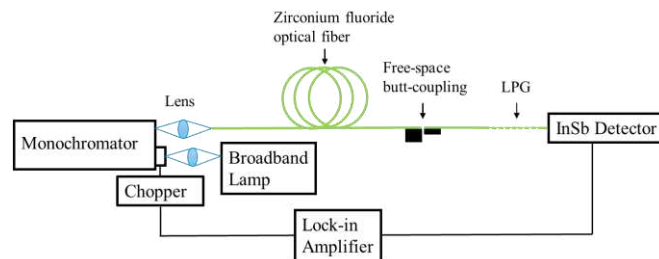
Figure 4.34   Experimental set-up employed for the characterization of the fabricated zirconium fluoride LPGs.

Figure 4.35 shows the normalized transmission spectrum T of the fabricated zirconium fluoride LPG, displaying a transmission dip near $\lambda = 3200\, nm$, in agreement with the numerical results.
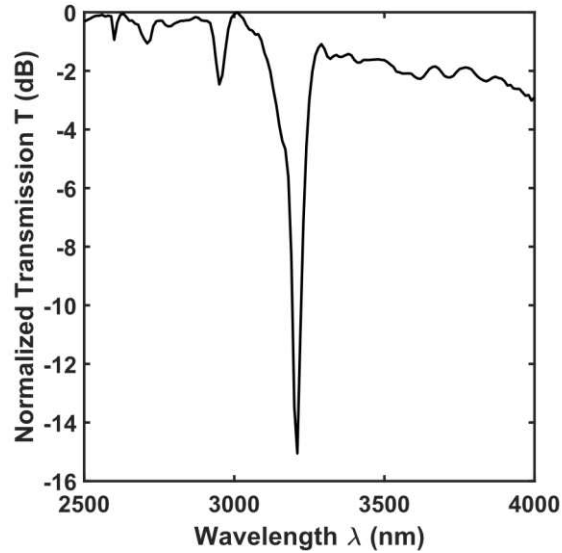
Figure 4.35   Measured normalized transmission spectrum T of the fabricated zirconium fluoride LPG.

4.4.3 Conclusion

The fabrication of LPGs in fluoride optical fibers micro-tapering technique has been investigated. The LPG is composed of 25 micro-tapers with waist diameter $d_w \approx 90\ \mu m$ and grating period $\Lambda \approx 1.36\ mm$. The attenuation of more than $15\ dB$ at the resonant wavelength, about $\lambda = 3200\ nm$, has been obtained. Low-loss LPGs in fluoride optical fibers can be considered a key component in a variety of applications, as they can help avoiding unwanted laser effects in fiber amplifiers/lasers and enable sensing in the Mid-IR range, which is valuable for environmental and biochemical monitoring.

4.5   Mid-infrared interferometry with non-adiabatic- and S-tapered ZBLAN optical fiber

Two different tapering techniques are employed to obtain all-fiber Mach-Zehnder interferometry in fluoride glass: i) non-adiabatic tapering, ii) s-tapering. The design is carried out via 2D-FEM and 3D-BPM. The characterization of the non-adiabatic tapering demonstrates good agreement with the simulation and good potential for the next generation of optical fiber sensors, operating in the Mid-IR. The following paragraphs are organized as follows: Section 4.4.1, the electromagnetic design of the interferometers; Section 4.4.2, the fabrication process and the characterization of the devices in the Mid-IR spectral range; Section 4.4.3, the conclusion and the prospects.

4.5.1 Design

The first device refers to the non-adiabatic taper, sketched in Figure 4.36. The electromagnetic design for the non-adiabatic taper is conducted using the same single-mode ZBLAN optical fiber employed for the LPG fabrication, specifically the ZFG SM [1.95] 6.5/125 from Le Verre Fluoré (Bruz, France). A 3-D BPM simulation is used to compute the sensor output spectrum. The non-adiabatic transition is achieved considering short down-taper and up-taper lengths, both set to $L_{dt} = L_{ut} = 2\,mm$. The waist length is designed to be $L_w \approx 8\,mm$ [221], [222], with simulations reported for $L_w = 8.05\,mm$ based on the fabricated proof of concept and experimental results. The waist diameter is $d_w = 25\,\mu m$. The pathway monitor confirms the excitation of the LP_{02} mode in the down-taper region.

Figure 4.37 illustrates the normalized output power P_{out} as a function of

wavelength λ for different temperature changes. It shows a blueshift in the dips as the temperature increases, with a simulated temperature sensitivity of $S_T = -85.3\,pm/K$ at $\lambda = 3310\,nm$. This result seems counterintuitive given the high positive thermal expansion coefficient α that increases the waist length L [125], [126]. In contrast, for silica tapers, the redshift of the m-th interference dip is typically explained by a positive change in both Δn_{eff} and length L, with the latter being minimal due to the low thermal expansion coefficient α [125], [126]. However, in silica optical fiber SMF-28 at $\lambda = 1550\,nm$, FEM computations show that the positive thermo-optic coefficient dn/dT results in a lower Δn_{eff} with increasing temperature. Thus, a more detailed investigation is conducted to understand this effect better. To explore the theoretical basis for the spectrum shift, a thorough electromagnetic analysis using FEM is performed.
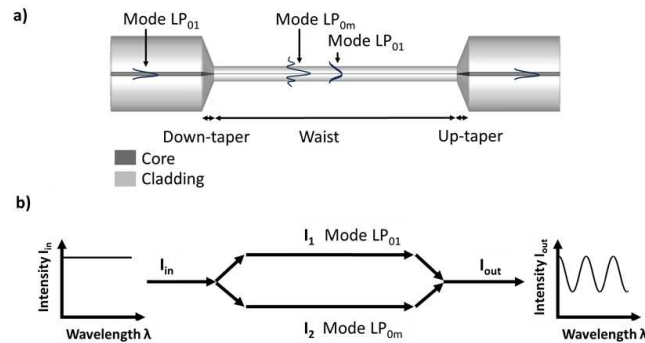
Figure 4.36 (a) Sketch of a non-adiabatic tapered optical fiber, with the down-taper, waist, and up-taper regions. (b) Schematic diagram of a non-adiabatic tapered optical fiber operating as a Mach-Zehnder interferometer [78].
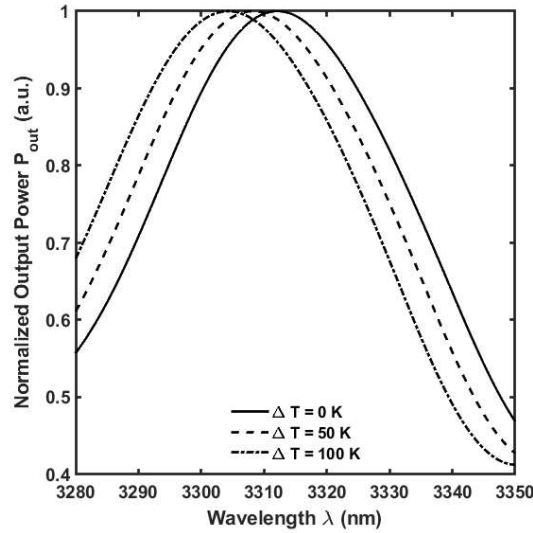
Figure 4.37   Normalized output power P_{out}, simulated via BPM, versus the wavelength λ for different temperature variations ΔT [78].

The 2-D electromagnetic modal analysis is carried out in the waist region of the ZFG SM [1.95] 6.5/125 fiber, with $d_{cl} = d_w = 25\,\mu m$ and $d_{co} = 1.3\,\mu m$, over temperature variations of $\Delta T = 0\,K$, $\Delta T = 50\,K$, $\Delta T = 100\,K$, and wavelengths from $\lambda = 3280\,nm$ to $\lambda = 3350\,nm$. The effective refractive indices n_{eff} of the fundamental LP$_{01}$ mode and the cladding LP$_{02}$ mode are calculated, considering the fluoride glass thermo-optic coefficient $dn/dT = -1.475 \times 10^{-5}\,K^{-1}$ on the core and cladding indices.

Figure 4.38 depicts the effective refractive index difference Δn_{eff} between the LP$_{01}$ and LP$_{02}$ modes versus wavelength λ for various temperature changes. The inset shows the normalized electric field norm E for both polarizations (x and y) of the LP$_{01}$ and LP$_{02}$ modes at $\lambda = 3.34\,\mu m$ and $\Delta T =$

$0\,K$.

Figure 4.39 displays the phase delay ϕ versus wavelength λ, influenced by: i) the variation in the waist region length L, which is affected by the fluoride glass thermal expansion coefficient $\alpha = 1.72 \times 10^{-5}\,K^{-1}$ and ii) the temperature-dependent change in the effective refractive index difference Δn_{eff}. The solution of the eq. $\phi = 2\pi/\lambda \times \Delta n_{eff} \times L$ shifts to shorter wavelengths (blueshift) with increasing temperature T.
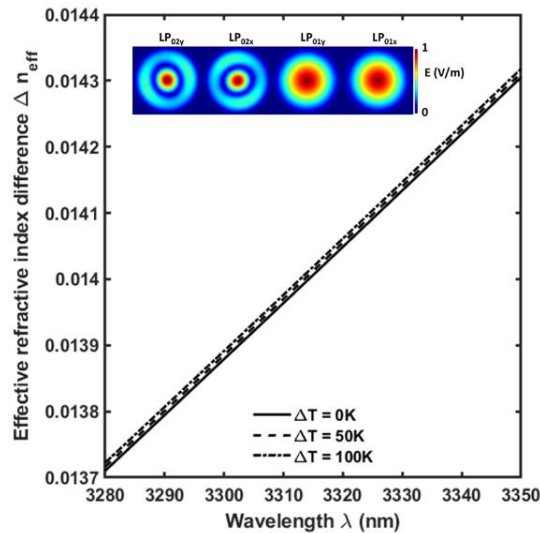
Figure 4.38   Effective refractive index difference Δn_{eff} between the LP01 mode and the LP02 mode, simulated via FEM, versus the wavelength λ for different temperature variations ΔT. In the inset, the normalized electric field norm E is reported for both the polarizations of the LP01 mode and of the LP02 mode at the wavelength $\lambda = 3.34\,\mu$m, for temperature variation ΔT [78].
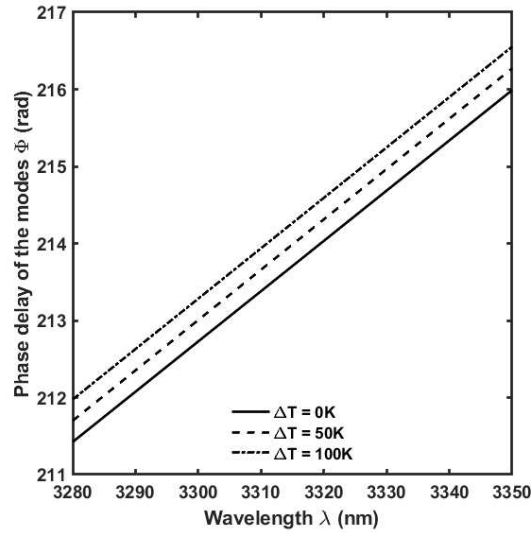
Figure 4.39   Phase delay of the modes ϕ versus the wavelength λ, simulated via FEM, for different temperature variations ΔT [78].

Figure 4.40 shows the cosine of the phase delay ϕ versus wavelength λ for different temperature changes ΔT, confirming the blueshift of the comb-like spectral pattern, due to both the negative thermo-optic coefficient dn/dT and the positive thermal expansion coefficient α of the fluoride glass. The temperature sensitivity, simulated with FEM, is $S_T = -85.3\,pm/K$ at $\lambda = 3310\,nm$ which aligns well with the 3-D BPM simulation results.

In silica optical fiber, the redshift arises from a decrease in Δn_{eff} with increasing temperature (which dominates over the length increase effect due to the small thermal expansion coefficient α). Conversely, in zirconium fluoride optical fiber, both Δn_{eff} and L increase, resulting in a blueshift with rising temperature.
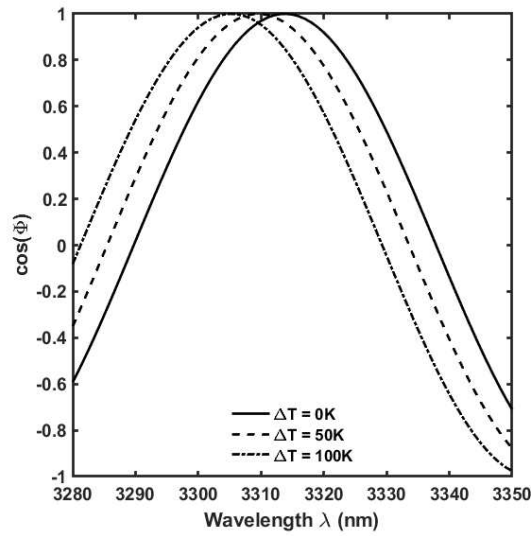
Figure 4.40   Cosine of the phase delay of the modes ϕ versus the wavelength λ, simulated via FEM, for different temperature variations ΔT [78].

The second design is based on S-tapered optical fiber. The same optical fiber is considered. To investigate the light propagation characteristics of the proposed STOF, three-dimensional numerical simulation based on BPM is performed. Three parameters can enable the optimization of the STOF, i.e. taper waist diameter d_w, axial offset h, and tapered region length L_w [195]. The wavelength λ is in the range from $\lambda = 2 \, \mu m$ to $\lambda = 4 \, \mu m$ and the axial offset h is in the range from $h = 50 \, \mu m$ to $h = 250 \, \mu m$. The simulation is repeated for four different waist diameters d_w from $d_w = 50 \, \mu m$ to $d_w = 80 \, \mu m$ with a step $\Delta d_w = 10 \, \mu m$. In every simulation, the tapered region length is set to $L_w = 1.5 \, mm$, feasible with the splicing equipment.

Figure 4.41 reports the surface plots about the total output power guided

by the LP$_{01}$ mode. For small axial offset h, the electromagnetic field is not efficiently coupled with the higher order modes and, thus, the output spectrum does not present the typical spectral interference pattern. On the contrary, when the axial offset h is too large, especially for small waist diameter d_w, the energy can be dissipated in the form of bending loss, and the energy of the fundamental mode and higher-order mode participating in the interference process decreases [196]. Moreover, the insertion loss can be too large, and the detector might not be able to read the signal. Considering the need for a detection with a good level of signal to noise ratio, it is preferrable to avoid blue region where the losses are too high and, at the same time, low value of offset should be avoided because of the inefficient interferometer effect that would be obtained. For this reason, a good trade-off is offered when considering $d_w = 60 \ \mu m$ and axial offset $h = 120 \ \mu m$.
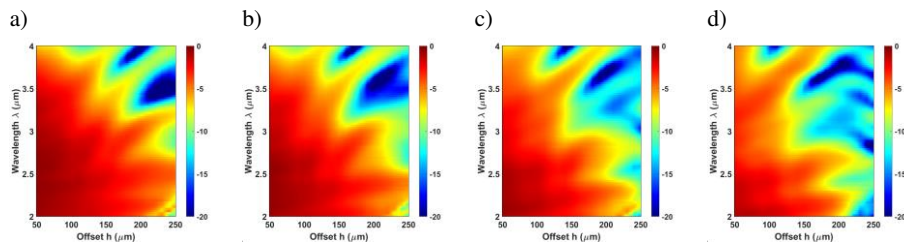
Figure 4.41   Total output power $P(dB)$ of the simulated s-tapered ZBLAN optical fiber with waist length $L_w = 1.5 \ mm$ as a function of offset h and wavelength λ for different waist diameters, a) $d_w = 80 \ \mu m$, b) $d_w = 70 \ \mu m$, c) $d_w = 60 \ \mu m$, d) $d_w = 50 \ \mu m$.

4.5.2 Fabrication and characterization

ZBLAN single-mode optical fiber, i.e. ZFG SM [1.95] 6.5/125, is used to fabricate the non-adiabatic taper. Pre-heating is optimized to prevent optical fiber bending due to gravity.

Figure 4.42 shows micrographs of the fabricated non-adiabatic taper taken with the Vytran GPX-2400 CCD camera, revealing a smooth transition and a good match between the designed and measured sensor geometry. The output power P_{out} is measured during the fabrication process of the non-adiabatic tapered zirconium fluoride optical fiber to prove the fabrication quality. The fiber is excited with Thorlabs HLS635 laser.

Figure 4.43 displays the output power P_{out} and tension F versus drawing time t. The down-taper region is completed at $t \approx 17\,s$, and the non-adiabatic taper at $t \approx 37\,s$. Most losses are attributed to the down-taper, with an insertion loss $IL \approx 0.8\,dB$, indicating good taper quality.
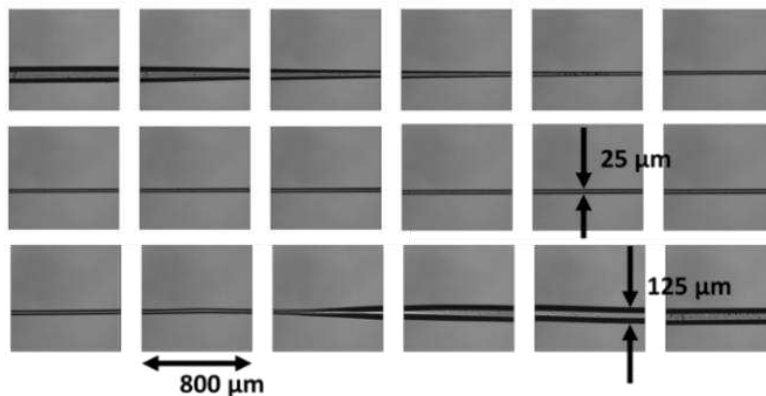
Figure 4.42   Micrographs of the longitudinal section of the non-adiabatic tapered optical fiber, taken with Vytran GPX-2400 CCD camera; each micrograph is long $800\,\mu m$ [78].

The excitation source is the ICL operating at $\lambda = 3.34 \, \mu m$. The sensor is excited using a Bare Fiber Terminator (BFT), and the far-field beam profile is captured with a Pyrocam IIIHR before the down-taper and in the waist region at $\lambda = 3.34 \, \mu m$, confirming the LP_{01} mode has the highest intensity in the waist region, as shown in Figure 4.44 and supported by 3D-BPM simulation.
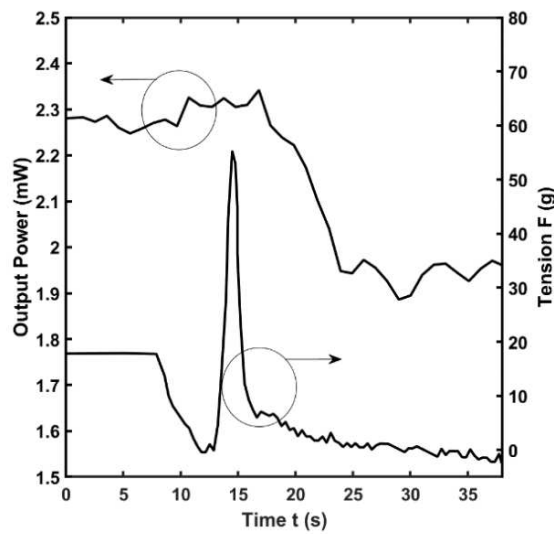
Figure 4.43   Output power Pout at wavelength $\lambda = 635 \, nm$ and tension F measured during the fabrication of the non-adiabatic tapered optical fiber [78].
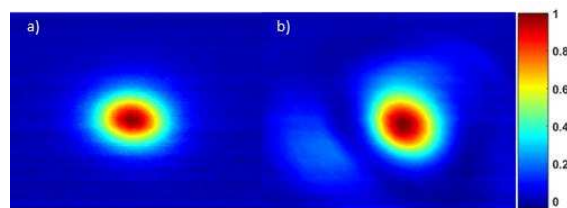
Figure 4.44   Measured farfield beam profile, captured with Pyrocam IIIHR at the wavelength $\lambda = 3.34 \, \mu m$; a) before the down-taper, b) in the waist region [78].

The experimental setup, illustrated in Figure 4.45, is used to demonstrate interferometry between the LP_{01} and LP_{02} modes. Measurements cover wavelengths from $\lambda = 3.00\,\mu m$ to $\lambda = 4.00\,\mu m$ and the cosinusoidal pattern is demonstrated, as illustrated in Figure 4.46.
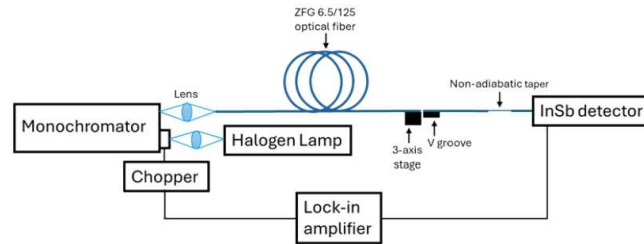
Figure 4.45   Schematic of the experimental set-up used for the spectrum characterization of the non-adiabatic tapered optical fiber [78].
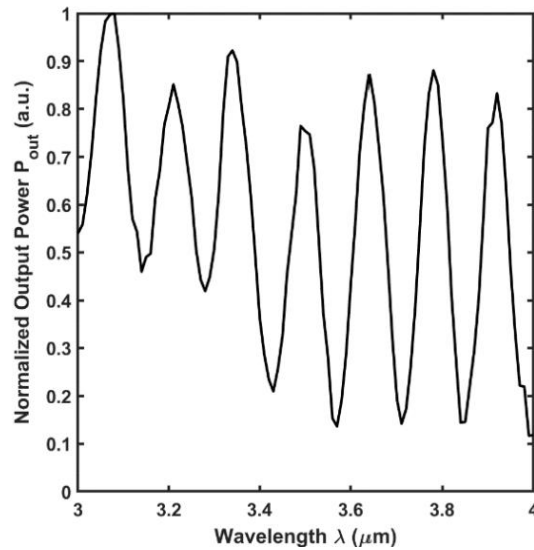
Figure 4.46   Measured normalized output power Pout of the non-adiabatic tapered optical fiber versus the wavelength λ [78].

The STOF is fabricated by applying off-axis pull while tapering the same single-mode zirconium fluoride optical fiber via Vytran GPX-2400. The optical fiber is mounted on the fiber holders and axial offset is provided, as illustrated in Figure 4.47. The longitudinal view of the obtained device is reported in Figure 4.48. In particular, each micrograph covers $800\ \mu m$. When considering soft glasses and especially with fluoride glasses, it is important to pay attention to the eventual presence of a grainy texture that indicates that the glass was over softened, and crystals were formed. The picture reveals a good fabrication. With a code based on image segmentation, the cladding geometric profile of the device is obtained. The core geometric profile is recovered knowing the starting core/cladding diameter ratio. In particular, Figure 4.49 reports the obtained profiles, and the measured waist length is about $d_w = 60\ \mu m$, while the tapered region length is approximately $L_w = 1.5\ mm$.
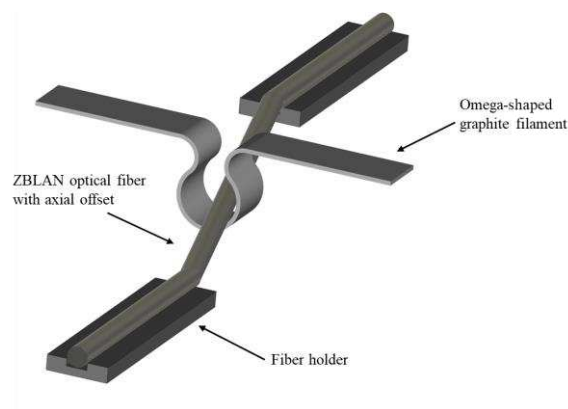
Figure 4.47　Schematic illustration of the fabrication procedure of the S-tapered ZBLAN optical fiber based on resistive filament heating and off-axis pulling.
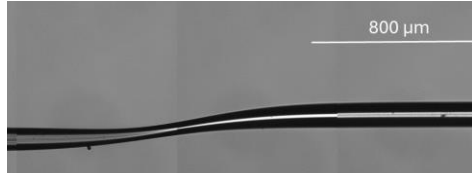
Figure 4.48   Longitudinal view of the fabricated s-tapered ZBLAN optical fiber, taken with Vytran GPX-2400 CCD camera.
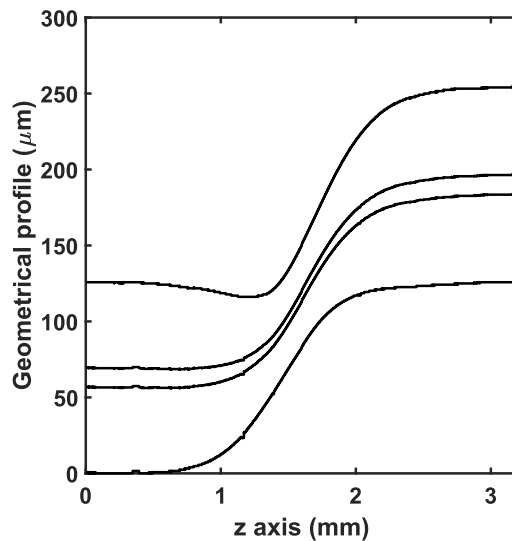
Figure 4.49   Core and cladding geometric profile as a function of the longitudinal direction, i.e. *z* axis.

4.5.3 Conclusion

A single-mode non-adiabatic tapered optical fiber made from zirconium fluoride glass has been designed and fabricated. This cost-effective microdevice is highly attractive for Mid-IR sensing applications. By leveraging the thermo-optic and

thermal expansion properties of zirconium fluoride, and the capability to operate at longer wavelengths, the device demonstrates a temperature sensor with higher sensitivity compared to those made of silica, given the same structure. Characterization is carried out in the Mid-IR by observing the output power variation with temperature. Experimental results align well with simulations. Broadband characterization confirms the predicted comb-like spectral pattern at the output of the non-adiabatic tapered zirconium fluoride optical fiber. Moreover, a S-tapered single-mode optical fiber is fabricated on zirconium fluoride glass. A preliminary numerical model is carried out in 3D-BPM and further work will include the characterization of the device against different surrounding refractive indices.

5 Mid-IR all-fiber sources

This chapter illustrates the results obtained during the Ph.D. research activity with respect to Mid-IR all-fiber CW source, useful for novel communication systems, sensing and medicine applications.

5.1 Design of a High Performance Mid-IR Fiber Laser Based on Pr3+-doped Fluoroindate Glass

A novel continuous wave fiber laser, pumped at $\lambda_p = 1550\ nm$ and emitting at $\lambda_s = 4\ \mu m$, is numerically designed and optimized. The active fluoroindate fiber is characterized by a step-index refractive index profile, with double cladding geometry, and it is doped with praseodymium. Measured spectroscopical parameters have been considered to solve the five-level rate equation model. The best predicted slope efficiency of about $\eta = 33\ \%$ and pump power threshold $P_{th} = 0.007\ W$ have been obtained for a fiber length $L_{fiber} = 0.4\ m$ and output mirror reflectivity $R_{out} = 30\ \%$. These values are very promising with respect to the state of the art. The following paragraphs are organized as follows: Section 5.1.1 reports the electromagnetic design; Section 5.1.2, the prospects and conclusion.

5.1.1 Design

The laser design considers a step-index double-cladding fluoroindate fiber doped with praseodymium, with a concentration $N_{Pr} = 1.6 \times 10^{26} \ ions/m^3$ (8000 ppm), by Le Verre Fluoré.

Figure 5.1 shows the fiber cross-section and the fundamental mode at the signal wavelength. The core diameter is $d_{co} = 7.5 \ \mu m$, the inner cladding diameter is $d_{cl_1} = 125 \ \mu m$ with a 2-D cut at a distance $d = 115 \ \mu m$, and the second cladding diameter $d_{cl_2} = 180 \ \mu m$. The other modeling parameters are listed in Table 5.1. The fiber analysis has been conducted using 2D-FEM modal analysis to determine the signal and pump overlap coefficients, $\Gamma_s = 0.312$ and $\Gamma_p = 0.899$, respectively. The fiber is single mode at the signal wavelength.
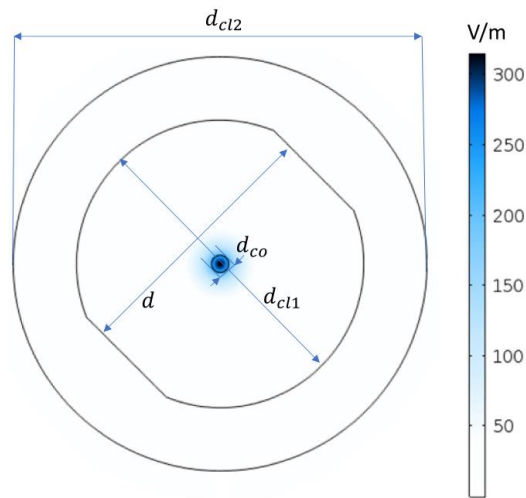
Figure 5.1   Fiber cross-section geometry and electric field norm E of the fundamental mode HE₁₁ at signal wavelength λ_s [161].

Table 5.2 shows the spectroscopical parameters used in the design, found in literature [223], [224], [225], [226], [227], [228].

TABLE 5.1   MODELING PARAMETERS [161].

Symbol	Value	Description
λ_p	$1550\ nm$	Pump wavelength
λ_s	$4000\ nm$	Signal wavelength
R_{in}	95 %	Input mirror reflectivity
R_{out}	$30 \div 80$ %	Output mirror reflectivity
L_{fiber}	$0.3 \div 0.7\ m$	Fiber length
$\alpha(\lambda_p)$	$0.1\ dB/m$	Glass attenuation at pump wavelength
$\alpha(\lambda_s)$	$0.01\ dB/m$	Glass attenuation at signal wavelength
$n_{co}(\lambda_p)$	1.4881	Core refractive index at pump wavelength
$n_{co}(\lambda_s)$	1.4721	Core refractive index at signal wavelength
$n_{cl1}(\lambda_p)$	1.4746	Inner cladding refractive index at pump wavelength
$n_{cl1}(\lambda_s)$	1.4585	Inner cladding refractive index at signal wavelength
$n_{cl2}(\lambda_p)$	1.3872	Outer cladding refractive index at pump wavelength
$n_{cl2}(\lambda_s)$	1.3785	Outer cladding refractive index at signal wavelength

TABLE 5.2   SPECTROSCOPIC PARAMETERS OF PR[3+]-DOPED FLUOROINDATE FIBER [161].

Symbol	Value	Description
$\sigma_{14}(\lambda_p)$	$1.2 \times 10^{-24}\ m^2$	Absorption cross section $H_4 \rightarrow H_5$
$\sigma_{41}(\lambda_p)$	$1.2 \times 10^{-24}\ m^2$	Emission cross section $H_5 \rightarrow H_4$
$\sigma_{25}(\lambda_p)$	$2.0 \times 10^{-25}\ m^2$	Absorption cross section $H_5 \rightarrow G_4$
$\sigma_{52}(\lambda_p)$	$4.8 \times 10^{-25}\ m^2$	Emission cross section $G_4 \rightarrow H_5$
$\sigma_{34}(\lambda_s)$	$6.5 \times 10^{-25}\ m^2$	Absorption cross section $F_2, H_6 \rightarrow F_{4,3}$
$\sigma_{43}(\lambda_s)$	$1.44 \times 10^{-24}\ m^2$	Emission cross section $F_{4,3} \rightarrow F_2, H_6$
τ_5	$2.35\ ms$	G_4 radiative lifetime
τ_4	$2.28\ ms$	$F_{4,3}$ radiative lifetime
τ_3	$57\ ms$	H_6 radiative lifetime
τ_2	$79\ ms$	H_5 radiative lifetime
β_{21}	100%	$H_5 \rightarrow H_4$ branching ratio
β_{31}	62.23%	$H_6 \rightarrow H_4$ branching ratio
β_{32}	37.77%	$H_6 \rightarrow H_5$ branching ratio
β_{41}	63.06%	$F_{4,3} \rightarrow H_4$ branching ratio
β_{42}	27.71%	$F_{4,3} \rightarrow H_5$ branching ratio
β_{43}	9.24%	$F_{4,3} \rightarrow F_2, H_6$ branching ratio
β_{51}	5.81%	$G_4 \rightarrow H_4$ branching ratio
β_{52}	61.26%	$G_4 \rightarrow H_5$ branching ratio
β_{53}	28.34%	$G_4 \rightarrow F_2, H_6$ branching ratio
β_{54}	4.57%	$G_4 \rightarrow F_{4,3}$ branching ratio
W_{NR51}	$14514\ s^{-1}$	Non-radiative rate $G_4 \rightarrow H_4$
W_{NR32}	$6664\ s^{-1}$	Non-radiative rate $H_6 \rightarrow H_5$
W_{NR21}	$499987\ s^{-1}$	Non-radiative rate $H_5 \rightarrow H_4$
W_{CR}	$2.25 \times 10^4\ s^{-1}$	Cross relaxation rate
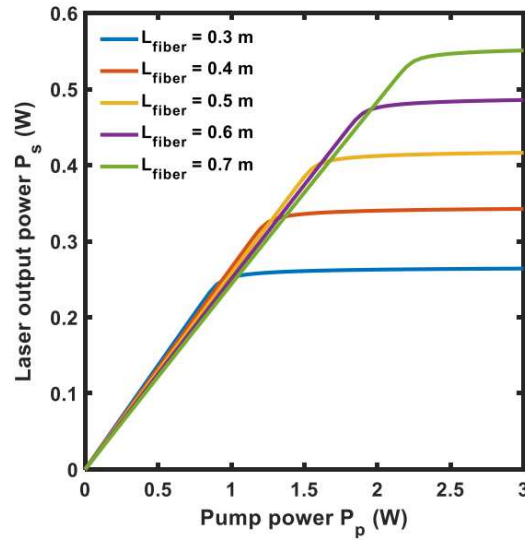
Figure 5.2   Laser output power P_s as a function of the input pump power P_p, for different values of the fiber length L_{fiber}, input mirror reflectivity $R_{in} = 95\%$, output mirror reflectivity $R_{out} = 80\%$ [161].

Simulations examined the laser output power P_s as a function of input pump power for various fiber lengths L_{fiber} and output mirror reflectivities R_{out}. The input mirror reflectivity was fixed at $R_{in} = 95\%$, simulating a high-reflectivity FBG in an all-fiber setup.

Figure 5.2 illustrates the laser output power P_s versus input pump power P_p for different fiber lengths L_{fiber}. The slope efficiency slightly decreases with longer fibers, while the threshold pump power P_{th} rises slightly. The optimal value is $L_{fiber} = 0.4\ m$ with $P_{th} = 0.003\ W$, $P_{sat} = 1.3\ W$, and $P_s = 0.34\ W$, yielding a slope efficiency $\eta = 28\%$.

Figure 5.3 shows P_s as a function of input pump power P_p for varying output mirror reflectivity R_{out}. As R_{out} decreases, the slope efficiency asymptotically increases, reaching $\eta = 32.5\%$ for $R_{out} = 30\%$, while P_{sat} remains relatively constant. The maximum power is $P_s = 0.42W$. P_{th} slightly increases with decreasing R_{out} but remains below $10\ mW$.
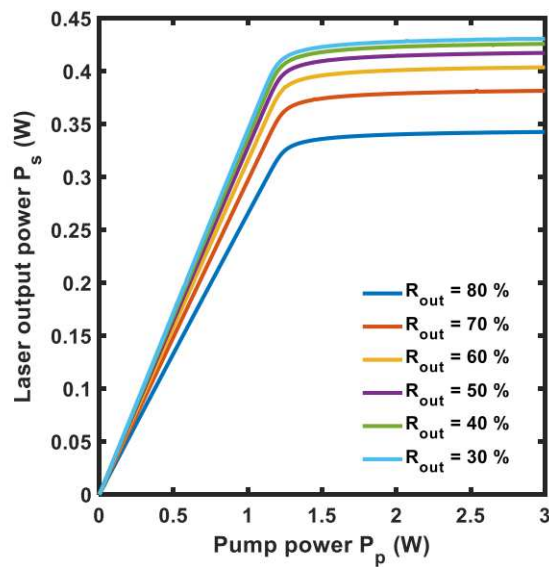
Figure 5.3 Laser output power P_s as a function of the input pump power P_p, for different values of the output mirror reflectivity R_{out}, input mirror reflectivity $R_{in} = 95\%$, fiber length $L_{fiber} = 0.4\ m$ [161].

Figure 5.4 presents the output power P_s versus the output mirror reflectivity R_{out} for different input pump powers P_p. P_s increases gradually for lower R_{out} values, with more noticeable variations at higher P_p. Figure 5.5 depicts P_s as a function of L_{fiber} for various P_p and a saturation can be identified for each P_p.
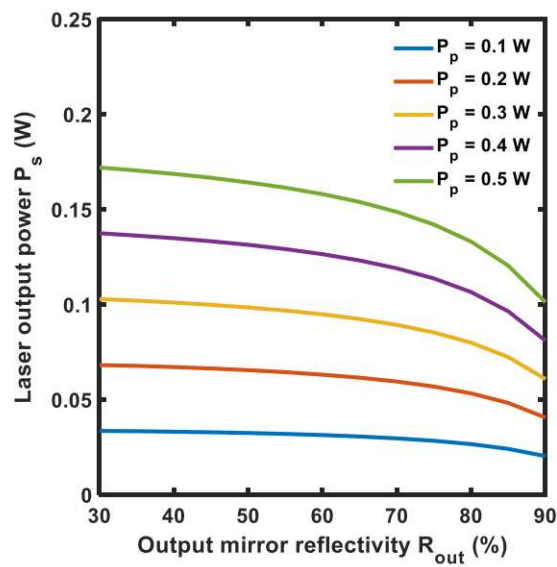
Figure 5.4   Laser output power P_s as a function of the output mirror reflectivity R_{out}, for different values of the input pump power P_p, input mirror reflectivity $R_{in} = 95\%$, fiber length $L_{fiber} = 0.4\ m$ [161].
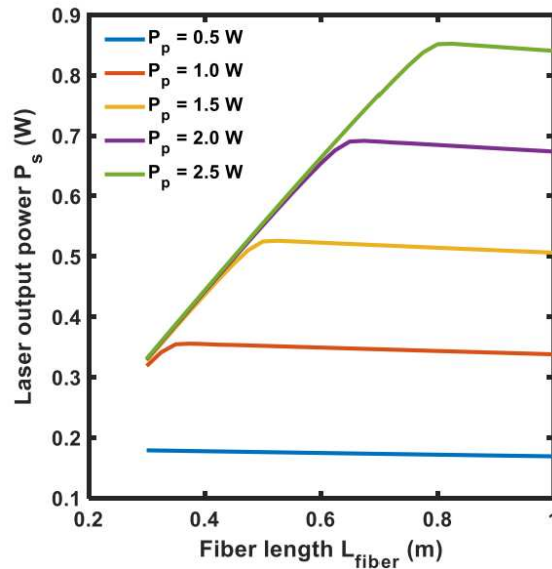
Figure 5.5 Laser output power P_s as a function of the fiber length L_{fiber}, for different values of the input pump power P_p, input mirror reflectivity $R_{in} = 95\%$, output mirror reflectivity $R_{out} = 30\%$ [161].

5.1.2 Conclusion

For the first time, a fiber laser based on praseodymium-doped fluoroindate glass, emitting at $\lambda_s = 4\mu m$ when pumped at $\lambda_p = 1550\ nm$, has been designed and optimized using spectroscopical parameters from literature. The predicted slope efficiency of $\eta = 33\%$ is promising, along with a low input pump threshold P_{th}. NIR pumping could be achieved using an erbium-doped fiber laser spliced with the praseodymium fluoroindate fiber cavity. Future advancements might explore co-doping with ytterbium to achieve multi-wavelength emission at both $\lambda_s = 3.6\ \mu m$ and $\lambda_s = 4\ \mu m$.

Conclusions

In this Ph.D. thesis novel optical fiber sensors, Mid-IR optical fiber components, and optical fiber source, tailored for IoT applications are designed and fabricated.

The key findings related to non-conventional fiber optic sensors based on Bragg gratings for the measurement of strain, temperature, and curvature can be summarized as follows:

- a microstructured flat fiber, for longitudinal and transverse strain sensing within CFRP laminates, has been designed; the relevant advantage introduced by the use of the microstructure close to one eyelet is the different slow and fast y axis sensitivities to transversal stresses $K_{y,f} = 12.89\, pm/MPa$, $K_{y,fm} = 21.06\, pm/MPa$, $K_{y,s} = 5.02\, pm/MPa$, $K_{y,sm} = 7.22\, pm/MPa$, leading to high sensitivity triaxial strain detection; moreover, the embedding of the flat fiber in CFRP has different advantages compared to standard circular optical fibers.

- an all-glass ultra-thin flexible silica planar Bragg grating-based sensor has been designed, fabricated, and experimentally characterized for high curvature monitoring up to $\pm\, 33\, m^{-1}$; the shift of the resonant wavelength for different curvatures is explained by means of modal analysis and coupled mode theory; there is a good agreement of the numerical results with the experiment.

- a novel approach for bending monitoring through flexible photonics Bragg grating-based sensor has been theoretically investigated and

experimentally demonstrated; the approach considers, at the same time, both the power level of the reflected fundamental mode power and of the reflected higher-order mode power and the Bragg wavelength shift; the proposed flexible sensor can withstand very high curvatures up to $110\ m^{-1}$ with Bragg wavelength shift sensitivities $K_{\lambda,fun} = -2.4\ pm/m - 1$, $K_{\lambda,hom} = -2.1\ pm/m^{-1}$ and ratiometric power sensitivity $K_{PR} = -0.78\ dB/mm$.

The main results regarding the design, fabrication, and characterization of Mid-IR optical fiber components based on soft glasses, exploitable for novel communication systems and spectroscopical applications, are reported in the following:

- the design, fabrication and characterization of a 3×1 fluoroindate combiner for the Mid-IR wavelength range is made for the first time by means of commercial glass processing workstation; the characterization at the wavelength $\lambda = 1.55\ \mu m$ demonstrates a maximum per-port net transmission efficiency of $\eta_{m,net} = 80.6\ \%$ in agreement with simulations; the broadband characterization demonstrates a flat behaviour of the efficiency from $\lambda = 1.0\ \mu m$ to $\lambda = 5.0\ \mu m$

- the design, fabrication, and characterization of different low-loss optical fiber couplers based on indium fluoride optical fibers within the mid-infrared spectral range have been demonstrated; for instance, the measured coupling ratio for a few-mode fiber-based coupler is $CR = 72.2 : 27.8$, with an excess loss $EL = 0.88\ dB$ at the wavelength $\lambda = 3.34\ \mu m$.

- the design, fabrication, and characterization of a mode-group selective photonic lantern based on indium fluoride optical fibers for the mid-infrared spectral range have been demonstrated; the device is based on the

use of different starting optical fibers to achieve the possibility of selectively excitation of the LP_{01} and of the LP_{11} mode at the multi-mode end of the device, with an insertion loss $IL < 2\ dB$.

- the design, fabrication, and characterization of sensors based on zirconium fluoride optical fibers for the mid-infrared spectral range have been demonstrated; LPGs have been demonstrated via micro-tapering technique, achieving $15\ dB$ attenuation at the coupling wavelength between the LP_{01} and the LP_{02} mode $\lambda = 3.2\ \mu m$; interferometers based on non-adiabatic tapers and S-tapers have been fabricated and will be employed for environmental sensing, exploiting the shift of the output comb-spectrum.

The design and optimization of a Mid-IR CW laser has been also addressed because it is an essential part of most communication and detection schemes. Moreover, novel Mid-IR CW sources may benefit of the demonstrated optical fiber components, improving the power-level (combiner), eliminating spurious emission (LPG), coupling different pump wavelengths (coupler), etc.

- A fiber laser based on praseodymium-doped fluoroindate glass pumped at $\lambda_p = 1550\ nm$ and emitting at $\lambda_s = 4\ \mu m$ has been designed and optimized using realistic spectroscopical parameters, with a promising slope efficiency $\eta = 33\%$ and a low input pump threshold.

As listed in the next paragraph, the obtained results have been published in International Journals and presented at National and International Conferences.

List of publications

International Journals:

[j1] F. Anelli, A. Annunziato, A. Erario, C. Holmes, C. Ciminelli, and F. Pruden-zano, "Design of Microstructured Flat Optical Fiber for Multiaxial Strain Monitoring in Composite Materials," *J. Light. Technol.*, vol. 40, no. 17, pp. 5986–5994, Sep. 2022, doi: 10.1109/JLT.2022.3186912.

[j2] A. Annunziato, F. Anelli, P. L. P. Du Teilleul, S. Cozic, S. Poulain, and F. Prudenzano, "Fused optical fiber combiner based on indium fluoride glass: perspectives for mid-IR applications," *Opt. Express*, vol. 30, no. 24, p. 44160, Nov. 2022, doi: 10.1364/OE.471090.

[j3] V. Portosi, A. M. Loconsole, A. Campana, F. Anelli, and F. Prudenzano, "A Novel L-Shaped Metalens for Ultra-Wide Band (UWB) Antenna Gain Improvement," *Appl. Sci.*, vol. 13, no. 8, p. 4802, Apr. 2023, doi: 10.3390/app13084802.

[j4] F. Anelli, A. Annunziato, M. Godfrey, A. M. Loconsole, C. Holmes, and F. Prudenzano, "Effects of Curvature on Flexible Bragg Grating in Off-Axis Core: Theory and Experiment," *J. Light. Technol.*, vol. 41, no. 9, pp. 2904–2910, May 2023, doi: 10.1109/JLT.2023.3238427.

[j5] A. M. Loconsole, V. Portosi, V.V. Francione, F. Anelli, A. Annunziato, M.C. Falconi, and F. Prudenzano "Optimization of a wideband antipodal Vivaldi antenna with metalenses," *Int. J. Microw. Wirel. Technol.*, pp. 1–8, Oct. 2023, doi: 10.1017/S1759078723001022.

[j6] F. Anelli, A. Annunziato, A. M. Loconsole, V. Portosi, S. Cozic, P. Le Pays du Teilleul, S. Venck, S. Poulain, and F. Prudenzano, "Low-Loss Fluoride Optical Fiber Coupler for Mid-Infrared Applications," *J. Light. Technol.*, vol. 42, no. 7, pp. 2457–2463, Apr. 2024, doi: 10.1109/JLT.2023.3337603.

[j7] A. Annunziato, M. Godfrey, F. Anelli, J. Dulieu-Barton, C. Holmes, and F. Prudenzano, "Flexible Photonic Sensors: Investigation of an Approach Based on

Ratiometric Power in Few-Mode Waveguides for Bending Measurement," *IEEE Access*, vol. 12, pp. 29166–29174, 2024, doi: 10.1109/ACCESS.2024.3368885.

[j8] A. M. Loconsole, V. V. Francione, A. Annunziato, F. Anelli, and F. Prudenzano, "Design of a High Performance Mid-IR Fiber Laser Based on Pr 3+ -Doped Fluoroindate Glass," *J. Light. Technol.*, vol. 42, no. 7, pp. 2488–2493, Apr. 2024, doi: 10.1109/JLT.2023.3338139.

[j9] F. Anelli, A. Annunziato, A. M. Loconsole, V.V. Francione, S. Cozic, S. Poulain, and F. Prudenzano, "Mid-infrared interferometry with non-adiabatic tapered ZBLAN optical fiber," *Opt. Express*, vol. 32, no. 11, p. 18944, May 2024, doi: 10.1364/OE.521239.

[j10] F. Anelli, A. Annunziato, A. M. Loconsole, S. Venck, S. Cozic, S. Poulain, and F. Prudenzano, "Mode-Group Selective Photonic Lantern based on Indium Fluoride Optical Fibers for Mid-Infrared," *J. Light. Technol.*, 2024, doi: 10.1109/JLT.2024.3450115.

[j11] F. Anelli, A. Annunziato, A. M. Loconsole, P. L. P. Du Teilleul, S. Cozic, and F. Prudenzano, "LPG in Fluoride Optical Fiber via Micro-Tapering Technique: Mid-IR Mode Coupling," *J. Light. Technol.*, doi: 10.1109/JLT.2024.3496501.

[j12] A.M. Loconsole, V.V. Francione, F. Anelli, S. Taccheo, and F. Prudenzano, "Mid-IR Amplification based on a Pr^{3+}:InF_3 Optical Fiber in the Range $3.8 - 4.2$ μm," submitted for publication on international journal.

[j13] L. Melchiorre, F. Anelli, G. Menduni, A. Annunziato, L. Bodin, S. Cozic, G. Magno, A. Sampaolo, F. Prudenzano, V. Spagnolo, "Dual-gas quartz-enhanced photoacoustic spectroscopy sensor exploiting two fiber-combined interband cascade lasers," submitted for publication on international journal.

[j14] F. Anelli, A. M. Loconsole, V.V. Francione, Md.I. Khan, F. Prudenzano, "Low-Cost Wideband Fabry-Pérot Resonator Antenna via Conductive Inkjet Printing and Additive Manufacturing," submitted for publication on international journal.

Proceedings of SPIE (* = presenter):

[sp1] F. Anelli (*), A. Annunziato, A. M. Loconsole, V.V. Francione, S. Cozic, S. Poulain, and F. Prudenzano "A temperature sensor based on all-fiber mach-zender interferometer with indium fluoride glass," in *Fiber Lasers and Glass Photonics: Materials through Applications IV*, S. Taccheo, M. R. Cicconi, and M. L. Jäger, Eds., Strasbourg, France: SPIE, Jun. 2024, p. 39. doi: 10.1117/12.3017496.

[sp2] A. Annunziato, F. Anelli (*), A. M. Loconsole, V.V. Francione, S. Cozic, S. Venck, S. Poulain, and F. Prudenzano, "Single-mode fluoroindate coupler for mid-IR applications," in *Fiber Lasers and Glass Photonics: Materials through Applications IV*, S. Taccheo, M. R. Cicconi, and M. L. Jäger, Eds., Strasbourg, France: SPIE, Jun. 2024, p. 29. doi: 10.1117/12.3017514.

[sp3] A. Annunziato, A. M. Loconsole, V.V. Francione, F. Anelli, L. Ressa, F. Pisani, G. Galzerano, and F. Prudenzano, "Design of in-band pumped dysprosium-doped ZBLAN fiber amplifier for mid-IR wavelength range," in *Fiber Lasers and Glass Photonics: Materials through Applications IV*, S. Taccheo, M. R. Cicconi, and M. L. Jäger, Eds., Strasbourg, France: SPIE, Jun. 2024, p. 14. doi: 10.1117/12.3017508.

[sp4] A. M. Loconsole, V.V. Francione, A. Annunziato, F. Anelli, Md. I. Khan, S. Taccheo, and F. Prudenzano, "Design of a mid-IR optical fiber amplifier based on a Pr3+:InF3 glass," in *Fiber Lasers and Glass Photonics: Materials through Applications IV*, S. Taccheo, M. R. Cicconi, and M. L. Jäger, Eds., Strasbourg, France: SPIE, Jun. 2024, p. 27. doi: 10.1117/12.3017504.

Proceedings of International Conferences (* = presenter):

[c1] F. Anelli (*), V. Portosi, A.M. Loconsole, A. Lacatena, A. Quatela, D. Laneve, A. Diaferia, F. Prudenzano, "Design of Electromagnetic Shielding for Food Pasteurization via Corrugated Waveguide and Graphite Rings," in *2022 Microwave Mediterranean Symposium (MMS)*, Pizzo Calabro, Italy: IEEE, May 2022, pp. 1–5. doi: 10.1109/MMS55062.2022.9825598.

[c2] A. M. Loconsole, V. Portosi, V. V. Francione, G. Roberto, F. Anelli, and F. Prudenzano, "Wideband antipodal Vivaldi antenna with metalenses for GPR applications," in *2022 Microwave Mediterranean Symposium (MMS)*, Pizzo Calabro, Italy: IEEE, May 2022, pp. 1–5. doi: 10.1109/MMS55062.2022.9825608.

[c3] F. Anelli (*), A. Annunziato, V. Portosi, S. Cozic, P. Le Pays Du Teilleul, and F. Prudenzano, "Multimode Fluoroindate Optical Fiber Coupler," in *2023 Conference on Lasers and Electro-Optics Europe & European Quantum Electronics Conference (CLEO/Europe-EQEC)*, Munich, Germany: IEEE, Jun. 2023, pp. 01–01. doi: 10.1109/CLEO/Europe-EQEC57999.2023.10232700.

[c4] C. Holmes, S. Zahertar, B. Moog, M. Godfrey, T. Lee, A. Annunziato, F. Anelli, B. Shi, M. Beresna, M. Whitaker, F. Prudenzano, R. Day, and J. Dulieu-Barton "Fabrication of Externally Microstructured Flat Optical Fibre for In-process Monitoring of Laminated Composite Structures," in *2023 Conference on Lasers and Electro-Optics Europe & European Quantum Electronics Conference (CLEO/Europe-EQEC)*, Munich, Germany: IEEE, Jun. 2023, pp. 1–1. doi: 10.1109/CLEO/Europe-EQEC57999.2023.10232169.

[c5] F. Anelli, A. Annunziato, A.M. Loconsole, V. Portosi, V.V. Francione, M.C. Falconi, P. Le Pays Du Teilleul, S. Cozic, S. Poulain, and F. Prudenzano, "Fabrication of Tapered Devices with Fluoride and Chalcogenide Optical Fibers for Mid-IR Applications," in *2023 23rd International Conference on Transparent Optical Networks (ICTON)*, Bucharest, Romania: IEEE, Jul. 2023, pp. 1–4. doi: 10.1109/ICTON59386.2023.10207517.

[c6] A. Annunziato, F. Anelli, A.M. Loconsole, M.C. Falconi, V. Portosi, V.V. Francione, and F. Prudenzano, "Optical Combining in Medium Infrared Wavelength Range and Its Applications," in *2023 23rd International Conference on Transparent Optical Networks (ICTON)*, Bucharest, Romania: IEEE, Jul. 2023, pp. 1–4. doi: 10.1109/ICTON59386.2023.10207305, invited paper.

[c7] A. M. Loconsole, A. Annunziato, F. Anelli, V.V. Francione, V. Portosi, M.C. Falconi, and F. Prudenzano, "Design of a Pr 3+ :InF 3 Fiber Laser Pumped in near-IR and Emitting at 4 micron Wavelength," in *2023 23rd International Conference*

on Transparent Optical Networks (ICTON), Bucharest, Romania: IEEE, Jul. 2023, pp. 1–4. doi: 10.1109/ICTON59386.2023.10207386.

[c8] F. Anelli (*), A. M. Loconsole, V. Portosi, A. Annunziato, V. V. Francione, and F. Prudenzano, "A Wideband Flexible Fabry-Perot Resonator Antenna: Inkjet-printing on Ultrathin PET Layers," in *2023 IEEE Conference on Antenna Measurements and Applications (CAMA)*, Genoa, Italy: IEEE, Nov. 2023, pp. 972–976. doi: 10.1109/CAMA57522.2023.10352659.

[c9] A. M. Loconsole, A. Mahmoud, F. Anelli, M. Ettorre, and F. Prudenzano, "Design of a V-band Slotted Antenna Array in Substrate Integrated Waveguide Technology," in *2023 IEEE Conference on Antenna Measurements and Applications (CAMA)*, Genoa, Italy: IEEE, Nov. 2023, pp. 968–971. doi: 10.1109/CAMA57522.2023.10352742.

[c10] F. Anelli, A. M. Loconsole, A. Annunziato, V. V. Francione, and F. Prudenzano, "Design and Characterization of a Flexible Fabry-Perot Antenna Fabricated using Conductive Inkjet Printing," in *2024 18th European Conference on Antennas and Propagation (EuCAP)*, Glasgow, United Kingdom: IEEE, Mar. 2024, pp. 1–5. doi: 10.23919/EuCAP60739.2024.10501739.

[c11] A. M. Loconsole, A. Mahmoud, F. Anelli, V. V. Francione, M. Ettorre, and F. Prudenzano, "Feasibility Investigation on a Low-Cost Air-Filled Substrate Integrated Waveguide Array Antenna in V-Band," in *2024 18th European Conference on Antennas and Propagation (EuCAP)*, Glasgow, United Kingdom: IEEE, Mar. 2024, pp. 1–5. doi: 10.23919/EuCAP60739.2024.10501173.

[c12] F. Anelli (*), A. Annunziato, A.M. Loconsole, V.V. Francione, Md. I. Khan, S. Cozic, S. Poulain, and F. Prudenzano, "Enhancing Sensing Capabilities: Fabrication of Tapered Optical Fiber Sensors in Fluoride Glasses," in *2024 24th International Conference on Transparent Optical Networks (ICTON)*, Bari, Italy: IEEE, Jul. 2024, pp. 1–4. doi: 10.1109/ICTON62926.2024.10648162.

[c15] F. Anelli (*), A. Annunziato, A.M. Loconsole, V.V. Francione, Md. I. Khan, S. Cozic, S. Poulain, and F. Prudenzano "Indium Fluoride Optical Fiber End-Pump Combiner for High-Power All-Fiber Sources," in *2024 24th International Conference on Transparent Optical Networks (ICTON)*, Bari, Italy: IEEE, Jul. 2024, pp. 1–4. doi: 10.1109/ICTON62926.2024.10647810.

[c13] Md. I. Khan, F. Anelli, A. M. Loconsole, V. V. Francione, and F. Prudenzano, "Ultra-Thin Metasurface for High Gain and Beam Steering at 5G Millimeter Wave Applications," in *2024 24th International Conference on Transparent Optical Networks (ICTON)*, Bari, Italy: IEEE, Jul. 2024, pp. 1–4. doi: 10.1109/ICTON62926.2024.10648279.
[c14] A. M. Loconsole, V.V. Francione, A. Annunziato, F. Anelli, Md. I. Khan, S. Taccheo, and F. Prudenzano, "Design of a praseodymium-doped fluoroindate fiber amplifier for medium infrared wavelength range applications," in *2024 24th International Conference on Transparent Optical Networks (ICTON)*, Bari, Italy: IEEE, Jul. 2024, pp. 1–4. doi: 10.1109/ICTON62926.2024.10648150.

International Conferences (* = presenter):

[i1] M. C. Falconi, A. M. Loconsole, A. Annunziato, F. Anelli, Yuchen Wang, G. Galzerano, and F. Prudenzano, "Simulation of a Dy3+:ZBLAN fiber laser passively Q-switched with a SESAM," in *Photoluminescence in Rare Earths:Photonic Materials Workshop (PRE'22-Poland)*, Szczawnica, Poland 11-14 September 2022.
[i2] F. Anelli (*), A. Annunziato, V. Portosi, P. Le Pays Du Teilleul, S. Cozic, S. Poulain, and F. Prudenzano, "Indium Fluoride Optical Fiber Coupler For Mid-Infrared Applications," in *3rd International Conference on Dielectric Photonic Devices and System Beyond Visible, D-Photon 2023*, Bari, 11-13 July 2023.
[i3] F. Anelli (*), V. Portosi, A. M. Loconsole, V. V. Francione, A. Annunziato, and F. Prudenzano, "A Wideband Inkjet-Printed Antenna On Flexible Pet Substrate," in *3rd International Conference on Dielectric Photonic Devices and System Beyond Visible, D-Photon 2023, Bari*, 11-13 July 2023.
[i4] A. Annunziato, F. Anelli, V. V. Francione, V. Portosi, A. M. Loconsole, C. Holmes, M. Godfrey, J. Dulieu-Barton, and F. Prudenzano, "Flexible Photonic Sensor For Bending Monitoring," in *3rd International Conference on Dielectric Photonic Devices and System Beyond Visible, D-Photon 2023*, Bari, 11-13 July 2023.

[i5] A. Annunziato, F. Anelli, V. V. Francione, A. M. Loconsole, V. Portosi, and F. Prudenzano, "Mid-IR Optical Combiners For All-In-Fiber Laser," in *3rd International Conference on Dielectric Photonic Devices and System Beyond Visible, D-Photon 2023*, Bari, 11-13 July 2023.

[i6] A. M. Loconsole, A. Mahmoud, F. Anelli, M. Ettorre, and F. Prudenzano, "Feasibility Investigation On An Air-Filled Substrate Integrated Waveguide Slot Antenna In V-Band", in *3rd International Conference on Dielectric Photonic Devices and System Beyond Visible, D-Photon 2023*, Bari, 11-13 July 2023.

[i7] A. M. Loconsole, A. Annunziato, M. C. Falconi, F. Anelli, V. V. Francione, V. Portosi, and F. Prudenzano, "Investigation On A Mid-Ir Laser Based On A Praseodymium-Doped Fluoroindate Fiber," in *3rd International Conference on Dielectric Photonic Devices and System Beyond Visible, D-Photon 2023*, Bari, 11-13 July 2023.

[i8] F. P. Pallotta, V. Portosi, A. M. Loconsole, V.V. Francione, F. Anelli, A. Annunziato, A. Crudele, and F. Prudenzano, "A Metalens For Non-In- vasive Microwave Hyperthermia In Cancer Treatment," in *3rd International Conference on Dielectric Photonic Devices and System Beyond Visible, D-Photon 2023*, Bari, 11-13 July 2023.

[i9] C. Holmes, S. Zahertar, B. Moog, M. Godfrey, T. Lee, A. Annunziato, F. Anelli, B. Shi, M. Beresna, M. Whitaker, F. Prudenzano, R. Day, and J. Dulieu-Barton, "Flexible Glass Photonics and Applications for Aerospace," in *3rd International Conference on Dielectric Photonic Devices and System Beyond Visible, D-Photon 2023*, Bari, 11-13 July 2023.

[i10] F. Anelli (*), A. Annunziato, A. M. Loconsole, M. C. Falconi, V. Portosi, V. V. Francione, and F. Prudenzano, "Fabrication of Mid-IR Tapered Devices Using Fluoride and Chalcogenide Optical Fibers," in *Conference on Photonics for Advanced Spectroscopy and Sensing (C-PASS)*, Castellaneta Marina, 3-8 September 2023.

[i11] A. Annunziato, F. Anelli, V. Portosi, V. V. Francione, A. M. Loconsole, M. C. Falconi, and F. Prudenzano, "Optical Fiber Couplers Based on Indium Fluoride Optical Fibers," in *Conference on Photonics for Advanced Spectroscopy and Sensing (C-PASS)*, Castellaneta Marina, 3-8 September 2023.

[i12] A. M. Loconsole, M. C. Falconi, A. Annunziato, F. Anelli, V. Portosi, V. V. Francione, and F. Prudenzano, "Investigation on a 4-μm emitting laser based on a fluoroindate fiber doped with praseodymium," in *Conference on Photonics for Advanced Spectroscopy and Sensing (C- PASS)*, Castellaneta Marina, 3-8 September 2023.

[i13] F. Anelli (*), A. Annunziato, A. M. Loconsole, S. Cozic, P. Du Teilleul, S. Venck, S. Poulain, and F. Prudenzano, "Fabrication of medium infrared optical fiber devices based on fluoride glass", in *Fifty Years of Fluoride glasses (50YFG)*, Rennes, France, 11-13 March 2024.

[i14] F. Anelli, A. M. Loconsole, V. V. Francione, A. Annunziato, M. I. Khan, and F. Prudenzano, "Recent advances on fiber devices for Mid-IR wavelength range", in *Photoluminescence in Rare Earths:Photonic Materials Workshop (PRE'24-Poland)*, Trento, Italy, 13-15 May 2024, invited paper.

National Conferences (= presenter)*:

[n1] M. C. Falconi, A. M. Loconsole, A. Annunziato, F. Anelli, and F. Prudenzano, "Design of An Erbium-Doped Fluoroindate Fiber Laser Pumped at 635 nm," in *Italian Conference on Optics and Photonics (ICOP)*, Trento, June 15-17, 2022.

[n2] A. M. Loconsole, V. Portosi, F. Anelli, A. Annunziato, V. V. Francione, M. C. Falconi, and F. Prudenzano, "Low-Profile Antipodal Vivaldi Antenna (Ava) for Ground Penentrating Radar Applications," in *XXIV RiNEm, Riunione Nazionale di Elettromagnetismo*, Catania, 18-21 September 2022.

[n3] M. C. Falconi, A. M. Loconsole, A. Annunziato, F. Anelli, Y. Wang, G. Galzerano, and F. Prudenzano, "Modeling of a Sesam-Based Dysprosium-Doped Zblan Fiber Laser Operating in Q-Switching Regime," in *XXIV RiNEm, Riunione Nazionale di Elettromagnetismo*, Catania, 18-21 September 2022.

[n4] F. Anelli (*), A. Annunziato, A. M. Loconsole, V.V. Francione, Md. I. Khan, and F. Prudenzano, "Towards Optical Fiber Sensing with Fluoride Glasses", in *Italian Conference on Optics and Photonics (ICOP)*, Florence, June 17-19, 2022.

[n5] F. Anelli (*), V.V. Francione, Md. I. Khan, and A. M. Loconsole, "Fabrication and Characterization of Micro-Tapered Long Period Gratings on Zirconium Fluoride Optical Fiber for Mid-Infrared Applications", in *XXV RiNEm, Riunione Nazionale di Elettromagnetismo*, Viareggio, September 2024.

[n6] A.M. Loconsole, V.V. Francione, F. Anelli, Md. I. Khan, A. Mahmoud, M. Ettorre, and F. Prudenzano, "Design and Fabrication of an Air-Filled Substrate Integrated Waveguide Antenna Array", in *XXV RiNEm, Riunione Nazionale di Elettromagnetismo*, Viareggio, September 2024.

References

[1] N. S. Prasad, "Optical Communications in the mid-wave IR spectral band," in *Free-Space Laser Communications*, New York, NY: Springer New York, 2005, pp. 347–391. doi: 10.1007/978-0-387-28677-8_8.

[2] M. Seminara *et al.*, "Characterization of noise regimes in mid-IR free-space optical communication based on quantum cascade lasers," *Opt. Express*, vol. 30, no. 25, p. 44640, Dec. 2022, doi: 10.1364/OE.470031.

[3] A. Fuerbach, G. Bharathan, and M. Ams, "Grating Inscription Into Fluoride Fibers: A Review," *IEEE Photonics J.*, vol. 11, no. 5, pp. 1–11, Oct. 2019, doi: 10.1109/JPHOT.2019.2940249.

[4] Y. Liu *et al.*, "Integrated near-infrared QEPAS sensor based on a 28 kHz quartz tuning fork for online monitoring of CO_2 in the greenhouse," *Photoacoustics*, vol. 25, p. 100332, Mar. 2022, doi: 10.1016/j.pacs.2022.100332.

[5] A. Séguin, R. I. Becerra-Deana, S. Virally, C. Boudoux, and N. Godbout, "Fabrication and characterization of indium fluoride multimode fused fiber couplers for the mid-infrared," *Opt. Express*, vol. 31, no. 20, p. 33670, Sep. 2023, doi: 10.1364/OE.501849.

[6] R. Bartlome and M. W. Sigrist, "Laser-based human breath analysis: D/H isotope ratio increase following heavy water intake," *Opt. Lett.*, vol. 34, no. 7, p. 866, Apr. 2009, doi: 10.1364/OL.34.000866.

[7] S. Dupont, C. Petersen, J. Thøgersen, C. Agger, O. Bang, and S. R. Keiding, "IR microscopy utilizing intense supercontinuum light source," *Opt. Express*, vol. 20, no. 5, p. 4887, Feb. 2012, doi: 10.1364/OE.20.004887.

[8] F. Tavakoli, A. Rekik, and M. Rochette, "Broadband and Wavelength-Dependent Chalcogenide Optical Fiber Couplers," *IEEE Photonics Technol. Lett.*, vol. 29, no. 9, pp. 735–738, May 2017, doi: 10.1109/LPT.2017.2682821.

[9]   D. Cai, Y. Xie, X. Guo, P. Wang, and L. Tong, "Chalcogenide Glass Microfibers for Mid-Infrared Optics," *Photonics*, vol. 8, no. 11, p. 497, Nov. 2021, doi: 10.3390/photonics8110497.

[10]   M. Saad, "Fluoride glass fiber: state of the art," presented at the SPIE Defense, Security, and Sensing, E. Udd, H. H. Du, and A. Wang, Eds., Orlando, Florida, USA, May 2009, p. 73160N. doi: 10.1117/12.824112.

[11]   É. Ducharme, S. Virally, R. I. Becerra-Deana, C. Boudoux, and N. Godbout, "Viscosity of fluoride glass fibers for fused component fabrication," *Appl. Opt.*, vol. 61, no. 17, p. 5031, Jun. 2022, doi: 10.1364/AO.455528.

[12]   C. Florea, J. Sanghera, L. Busse, B. Shaw, F. Miklos, and I. Aggarwal, "Reduced Fresnel losses in chalcogenide fibers obtained through fiber-end microstructuring," *Appl. Opt.*, vol. 50, no. 1, p. 17, Jan. 2011, doi: 10.1364/AO.50.000017.

[13]   M. Saad, R. Pafchek, P. Foy, Z. Jiang, D. Gardner, and P. Hawkins, "Indium Fluoride Glass Fibers for Mid-Infrared applications," in *Workshop on Specialty Optical Fibers and Their Applications*, Hong Kong: OSA, 2015, p. WW4A.3. doi: 10.1364/WSOF.2015.WW4A.3.

[14]   R. Kashyap, *Fiber Bragg gratings*, 2nd ed. Burlington, MA: Academic Press, 2010.

[15]   G. C. Kahandawa, J. Epaarachchi, H. Wang, and K. T. Lau, "Use of FBG Sensors for SHM in Aerospace Structures," *Photonic Sens.*, vol. 2, no. 3, pp. 203–214, Sep. 2012, doi: 10.1007/s13320-012-0065-4.

[16]   D. Luo, Z. Ismail, and Z. Ibrahim, "Added advantages in using a fiber Bragg grating sensor in the determination of early age setting time for cement pastes," *Measurement*, vol. 46, no. 10, pp. 4313–4320, Dec. 2013, doi: 10.1016/j.measurement.2013.06.036.

[17]   D. Grobnic, C. Hnatovsky, S. Dedyulin, R. B. Walker, H. Ding, and S. J. Mihailov, "Fiber Bragg Grating Wavelength Drift in Long-Term High Temperature Annealing," *Sensors*, vol. 21, no. 4, p. 1454, Feb. 2021, doi: 10.3390/s21041454.

[18]   C. V. N. Bhaskar, S. Pal, and P. K. Pattnaik, "Recent advancements in fiber Bragg gratings based temperature and strain measurement," *Results Opt.*, vol. 5, p. 100130, Dec. 2021, doi: 10.1016/j.rio.2021.100130.

[19]   T. C. Buck, M. S. Müller, and A. W. Koch, "Theoretical Assessment of an All-Optical Temporal Low-Pass Filter for Dynamic Fiber Bragg Grating Signals," *J. Sens.*, vol. 2011, pp. 1–5, 2011, doi: 10.1155/2011/302380.

[20]   D. Kinet, P. Mégret, K. Goossen, L. Qiu, D. Heider, and C. Caucheteur, "Fiber Bragg Grating Sensors toward Structural Health Monitoring in Composite Materials: Challenges and Solutions," *Sensors*, vol. 14, no. 4, pp. 7394–7419, Apr. 2014, doi: 10.3390/s140407394.

[21]   D. S. Vijayan, A. Sivasuriyan, P. Devarajan, A. Stefańska, Ł. Wodzyński, and E. Koda, "Carbon Fibre-Reinforced Polymer (CFRP) Composites in Civil Engineering Application—A Comprehensive Review," *Buildings*, vol. 13, no. 6, p. 1509, Jun. 2023, doi: 10.3390/buildings13061509.

[22]   I. A. Popan, N. Balc, and A. I. Popan, "Avoiding carbon fibre reinforced polymer delamination during abrasive water jet piercing: a new piercing method," *Int. J. Adv. Manuf. Technol.*, vol. 119, no. 1–2, pp. 1139–1152, Mar. 2022, doi: 10.1007/s00170-021-08294-7.

[23]   C. Sonnenfeld *et al.*, "Microstructured Optical Fiber Sensors Embedded in a Laminate Composite for Smart Material Applications," *Sensors*, vol. 11, no. 3, pp. 2566–2579, Feb. 2011, doi: 10.3390/s110302566.

[24]   T. Vella *et al.*, "Full-spectrum interrogation of fiber Bragg gratings at 100 kHz for detection of impact loading," *Meas. Sci. Technol.*, vol. 21, no. 9, p. 094009, Sep. 2010, doi: 10.1088/0957-0233/21/9/094009.

[25]   H.-P. Wang, Y.-Q. Ni, J.-G. Dai, and M.-D. Yuan, "Interfacial debonding detection of strengthened steel structures by using smart CFRP-FBG composites," *Smart Mater. Struct.*, vol. 28, no. 11, p. 115001, Nov. 2019, doi: 10.1088/1361-665X/ab3add.

[26]   S. Takeda, Y. Okabe, and N. Takeda, "Monitoring of Delamination Growth in CFRP Laminates using Chirped FBG Sensors," *J. Intell. Mater. Syst. Struct.*, vol. 19, no. 4, pp. 437–444, Apr. 2008, doi: 10.1177/1045389X06074085.

[27]   S. Takeda, Y. Okabe, and N. Takeda, "Delamination detection in CFRP laminates with embedded small-diameter fiber Bragg grating sensors," *Compos. Part Appl. Sci. Manuf.*, vol. 33, no. 7, pp. 971–980, Jul. 2002, doi: 10.1016/S1359-835X(02)00036-2.

[28]   A. Rajabzadeh, R. Heusdens, R. C. Hendriks, and R. M. Groves, "Characterisation of Transverse Matrix Cracks in Composite Materials Using Fibre Bragg Grating Sensors," *J. Light. Technol.*, vol. 37, no. 18, pp. 4720–4727, Sep. 2019, doi: 10.1109/JLT.2019.2919339.

[29]   J. Frieden, J. Cugnoni, J. Botsis, and T. Gmür, "Low energy impact damage monitoring of composites using dynamic strain signals from FBG sensors – Part II: Damage identification," *Compos. Struct.*, vol. 94, no. 2, pp. 593–600, Jan. 2012, doi: 10.1016/j.compstruct.2011.08.025.

[30]   Z.-S. Guo, "Strain and Temperature Monitoring of Asymmetric Composite Laminate using FBG Hybrid Sensors," *Struct. Health Monit.*, vol. 6, no. 3, pp. 191–197, Sep. 2007, doi: 10.1177/1475921707006003020.

[31]   F. Bosia, P. Giaccari, J. Botsis, M. Facchini, H. G. Limberger, and R. P. Salathé, "Characterization of the response of fibre Bragg grating sensors subjected to a two-dimensional strain field," *Smart Mater. Struct.*, vol. 12, no. 6, pp. 925–934, Dec. 2003, doi: 10.1088/0964-1726/12/6/009.

[32]   G. Luyckx, E. Voet, N. Lammens, W. De Waele, and J. Degrieck, "Residual strain-induced birefringent FBGs for multi-axial strain monitoring of CFRP composite laminates," *NDT E Int.*, vol. 54, pp. 142–150, Mar. 2013, doi: 10.1016/j.ndteint.2012.11.008.

[33]   K. D. Dambul *et al.*, "Fabrication and characterization of Ge-doped flat fibres," *J. Mod. Opt.*, vol. 66, no. 11, pp. 1219–1225, Jun. 2019, doi: 10.1080/09500340.2019.1610518.

[34]   F. R. M. Adikan *et al.*, "Direct UV Written Optical Waveguides in Flexible Glass Flat Fiber Chips," *IEEE J. Sel. Top. Quantum Electron.*, vol. 18, no. 5, pp. 1534–1539, Sep. 2012, doi: 10.1109/JSTQE.2011.2171921.

[35]   T. H. Loutas, A. Panopoulou, D. Roulias, and V. Kostopoulos, "Intelligent health monitoring of aerospace composite structures based on dynamic

strain measurements," *Expert Syst. Appl.*, vol. 39, no. 9, pp. 8412–8422, Jul. 2012, doi: 10.1016/j.eswa.2012.01.179.

[36]   A. Propst *et al.*, "Assessment of damage in composite laminates through dynamic, full-spectral interrogation of fiber Bragg grating sensors," *Smart Mater. Struct.*, vol. 19, no. 1, p. 015016, Jan. 2010, doi: 10.1088/0964-1726/19/1/015016.

[37]   A. Papantoniou, G. Rigas, and N. D. Alexopoulos, "Assessment of the strain monitoring reliability of fiber Bragg grating sensor (FBGs) in advanced composite structures," *Compos. Struct.*, vol. 93, no. 9, pp. 2163–2172, Aug. 2011, doi: 10.1016/j.compstruct.2011.03.001.

[38]   E. Voet, G. Luyckx, W. De Waele, and J. Degrieck, "Multi-axial strain transfer from laminated CFRP composites to embedded Bragg sensor: II. Experimental validation," *Smart Mater. Struct.*, vol. 19, no. 10, p. 105018, Oct. 2010, doi: 10.1088/0964-1726/19/10/105018.

[39]   G. Luyckx, E. Voet, N. Lammens, and J. Degrieck, "Strain Measurements of Composite Laminates with Embedded Fibre Bragg Gratings: Criticism and Opportunities for Research," *Sensors*, vol. 11, no. 1, pp. 384–408, Dec. 2010, doi: 10.3390/s110100384.

[40]   F. Anelli, A. Annunziato, A. Erario, C. Holmes, C. Ciminelli, and F. Prudenzano, "Design of Microstructured Flat Optical Fiber for Multiaxial Strain Monitoring in Composite Materials," *J. Light. Technol.*, vol. 40, no. 17, pp. 5986–5994, Sep. 2022, doi: 10.1109/JLT.2022.3186912.

[41]   C. Holmes *et al.*, "Fabrication of Externally Microstructured Flat Optical Fibre for In-process Monitoring of Laminated Composite Structures," in *2023 Conference on Lasers and Electro-Optics Europe & European Quantum Electronics Conference (CLEO/Europe-EQEC)*, Munich, Germany: IEEE, Jun. 2023, pp. 1–1. doi: 10.1109/CLEO/Europe-EQEC57999.2023.10232169.

[42]   A. Annunziato, F. Anelli, M. Godfrey, J. M. Barton, C. Holmes, and F. Prudenzano, "Design of Flat Optical Fiber Sensor for Triaxial Strain Monitoring in Composite Laminates," in *2021 AEIT International Annual Conference (AEIT)*, Milan, Italy: IEEE, Oct. 2021, pp. 1–6. doi: 10.23919/AEIT53387.2021.9626867.

[43]   J. Ge, A. E. James, L. Xu, Y. Chen, K.-W. Kwok, and M. P. Fok, "Bidirectional Soft Silicone Curvature Sensor Based on Off-Centered Embedded Fiber Bragg Grating," *IEEE Photonics Technol. Lett.*, vol. 28, no. 20, pp. 2237–2240, Oct. 2016, doi: 10.1109/LPT.2016.2590984.

[44]   M. Rosenberger, H. Pauer, M. Girschikofsky, H. Woern, B. Schmauss, and R. Hellmann, "Flexible Polymer Shape Sensor Based on Planar Waveguide Bragg Gratings," *IEEE Photonics Technol. Lett.*, vol. 28, no. 17, pp. 1898–1901, Sep. 2016, doi: 10.1109/LPT.2016.2574889.

[45]   G. Macrelli, A. K. Varshneya, and J. C. Mauro, "Ultra-thin glass as a substrate for flexible photonics," *Opt. Mater.*, vol. 106, p. 109994, Aug. 2020, doi: 10.1016/j.optmat.2020.109994.

[46]   D. Feng, X. Qiao, and J. Albert, "Off-axis ultraviolet-written fiber Bragg gratings for directional bending measurements," *Opt. Lett.*, vol. 41, no. 6, p. 1201, Mar. 2016, doi: 10.1364/OL.41.001201.

[47]   W. Bao, Q. Rong, F. Chen, and X. Qiao, "All-fiber 3D vector displacement (bending) sensor based on an eccentric FBG," *Opt. Express*, vol. 26, no. 7, p. 8619, Apr. 2018, doi: 10.1364/OE.26.008619.

[48]   X. Chen, C. Zhang, D. J. Webb, K. Kalli, and G.-D. Peng, "Highly Sensitive Bend Sensor Based on Bragg Grating in Eccentric Core Polymer Fiber," *IEEE Photonics Technol. Lett.*, vol. 22, no. 11, pp. 850–852, Jun. 2010, doi: 10.1109/LPT.2010.2046482.

[49]   L.-Y. Shao, L. Xiong, C. Chen, A. Laronche, and J. Albert, "Directional Bend Sensor Based on Re-Grown Tilted Fiber Bragg Grating," *J. Light. Technol.*, vol. 28, no. 18, pp. 2681–2687, Sep. 2010, doi: 10.1109/JLT.2010.2064158.

[50]   Y. X. Jin, C. C. Chan, X. Y. Dong, and Y. F. Zhang, "Temperature-independent bending sensor with tilted fiber Bragg grating interacting with multimode fiber," *Opt. Commun.*, vol. 282, no. 19, pp. 3905–3907, Oct. 2009, doi: 10.1016/j.optcom.2009.06.058.

[51]   I. M. Nascimento, G. Chesini, J. M. Baptista, C. M. B. Cordeiro, and P. A. S. Jorge, "LPG-based sensor for curvature and vibration," presented at the Sixth European Workshop on Optical Fibre Sensors (EWOFS'2016), E. Lewis, Ed., Limerick, Ireland, May 2016, p. 99162D. doi: 10.1117/12.2237041.

[52] X. Wang *et al.*, "Seven-core fiber embedded ultra-long period grating for curvature, torsion or temperature sensing," *Opt. Commun.*, vol. 536, p. 129351, Jun. 2023, doi: 10.1016/j.optcom.2023.129351.

[53] Y. Liu, J. Dong, L. Huang, X. Song, and B. Li, "Investigations on seven-core fiber based interferometric all-fiber sensor for curvature and temperature measurements," *Optik*, vol. 254, p. 168638, Mar. 2022, doi: 10.1016/j.ijleo.2022.168638.

[54] O. Frazão *et al.*, "All-fiber Mach-Zehnder curvature sensor based on multimode interference combined with a long-period grating," *Opt. Lett.*, vol. 32, no. 21, p. 3074, Nov. 2007, doi: 10.1364/OL.32.003074.

[55] M. Cano-Contreras *et al.*, "All-Fiber Curvature Sensor Based on an Abrupt Tapered Fiber and a Fabry–Pérot Interferometer," *IEEE Photonics Technol. Lett.*, vol. 26, no. 22, pp. 2213–2216, Nov. 2014, doi: 10.1109/LPT.2014.2349979.

[56] M. Hou *et al.*, "Two-dimensional vector bending sensor based on seven-core fiber Bragg gratings," *Opt. Express*, vol. 26, no. 18, p. 23770, Sep. 2018, doi: 10.1364/OE.26.023770.

[57] A. Zafeiropoulou, A. Masoudi, A. Zdagkas, L. Cooper, and G. Brambilla, "Curvature sensing with a D-shaped multicore fibre and Brillouin optical time-domain reflectometry," *Opt. Express*, vol. 28, no. 2, p. 1291, Jan. 2020, doi: 10.1364/OE.383096.

[58] D. Zheng, J. Madrigal, H. Chen, D. Barrera, and S. Sales, "Multicore fiber-Bragg-grating-based directional curvature sensor interrogated by a broadband source with a sinusoidal spectrum," *Opt. Lett.*, vol. 42, no. 18, p. 3710, Sep. 2017, doi: 10.1364/OL.42.003710.

[59] F. Khan, A. Denasi, D. Barrera, J. Madrigal, S. Sales, and S. Misra, "Multi-Core Optical Fibers With Bragg Gratings as Shape Sensor for Flexible Medical Instruments," *IEEE Sens. J.*, vol. 19, no. 14, pp. 5878–5884, Jul. 2019, doi: 10.1109/JSEN.2019.2905010.

[60] F. Anelli, A. Annunziato, M. Godfrey, A. M. Loconsole, C. Holmes, and F. Prudenzano, "Effects of Curvature on Flexible Bragg Grating in Off-Axis

Core: Theory and Experiment," *J. Light. Technol.*, vol. 41, no. 9, pp. 2904–2910, May 2023, doi: 10.1109/JLT.2023.3238427.

[61]   A. Annunziato, M. Godfrey, F. Anelli, J. Dulieu-Barton, C. Holmes, and F. Prudenzano, "Flexible Photonic Sensors: Investigation of an Approach Based on Ratiometric Power in Few-Mode Waveguides for Bending Measurement," *IEEE Access*, vol. 12, pp. 29166–29174, 2024, doi: 10.1109/AC-CESS.2024.3368885.

[62]   M. Poulain, M. Poulain, and J. Lucas, "Verres fluores au tetrafluorure de zirconium proprietes optiques d'un verre dope au Nd3+," *Mater. Res. Bull.*, vol. 10, no. 4, pp. 243–246, Apr. 1975, doi: 10.1016/0025-5408(75)90106-3.

[63]   M. Poulain, "Crystallization in fluoride glasses," *Thermochim. Acta*, vol. 280–281, pp. 343–351, Jul. 1996, doi: 10.1016/0040-6031(95)02652-5.

[64]   M. Robinson, "Processing and purification techniques of heavy metal fluoride glass (HMFG)," *J. Cryst. Growth*, vol. 75, no. 1, pp. 184–194, May 1986, doi: 10.1016/0022-0248(86)90240-X.

[65]   S. Cozic, S. Boivinet, C. Pierre, J. Boulet, S. Poulain, and M. Poulain, "Splicing fluoride glass and silica optical fibers," *EPJ Web Conf.*, vol. 215, p. 04003, 2019, doi: 10.1051/epjconf/201921504003.

[66]   O. Benderov *et al.*, "Broadband mid-IR chalcogenide fiber couplers," *Appl. Opt.*, vol. 58, no. 26, p. 7222, Sep. 2019, doi: 10.1364/AO.58.007222.

[67]   R. R. Gattass *et al.*, "Infrared Fiber $N \times 1$ Multimode Combiner," *IEEE Photonics J.*, vol. 5, no. 5, pp. 7100905–7100905, Oct. 2013, doi: 10.1109/JPHOT.2013.2281611.

[68]   B. Stepanov, O. Benderov, T. Tebeneva, G. Snopatin, M. Spiridonov, and I. Scripachev, "Chalcogenide optical fiber couplers made by FBT method," *J. Non-Cryst. Solids*, vol. 480, pp. 23–27, Jan. 2018, doi: 10.1016/j.jnon-crysol.2017.09.020.

[69]   R. R. Gattass, R. Thapa, F. H. Kung, L. E. Busse, L. B. Shaw, and J. S. Sanghera, "Review of infrared fiber-based components," *Appl. Opt.*, vol. 54, no. 31, p. F25, Nov. 2015, doi: 10.1364/AO.54.000F25.

[70]   D. T. Schaafsma, J. A. Moon, J. S. Sanghera, and I. D. Aggarwal, "Fused taper infrared optical fiber couplers in chalcogenide glass," *J. Light. Technol.*, vol. 15, no. 12, pp. 2242–2245, Dec. 1997, doi: 10.1109/50.643548.

[71]   F. Anelli *et al.*, "Low-Loss Fluoride Optical Fiber Coupler for Mid-Infrared Applications," *J. Light. Technol.*, vol. 42, no. 7, pp. 2457–2463, Apr. 2024, doi: 10.1109/JLT.2023.3337603.

[72]   M. Rezaei, G. T. Zeweldi, M. H. M. Shamim, and M. Rochette, "Single-mode optical fiber couplers made of fluoride glass," *Opt. Express*, vol. 31, no. 17, p. 27183, Aug. 2023, doi: 10.1364/OE.495464.

[73]   A. Annunziato, F. Anelli, P. L. P. Du Teilleul, S. Cozic, S. Poulain, and F. Prudenzano, "Fused optical fiber combiner based on indium fluoride glass: perspectives for mid-IR applications," *Opt. Express*, vol. 30, no. 24, p. 44160, Nov. 2022, doi: 10.1364/OE.471090.

[74]   S. Magnan-Saucier *et al.*, "Fuseless side-pump combiner for efficient fluoride-based double-clad fiber pumping," *Opt. Lett.*, vol. 45, no. 20, p. 5828, Oct. 2020, doi: 10.1364/OL.409174.

[75]   L. She *et al.*, "Mid-infrared fluoroindate glass long-period fiber grating by femtosecond laser inscription," *Infrared Phys. Technol.*, vol. 116, p. 103808, Aug. 2021, doi: 10.1016/j.infrared.2021.103808.

[76]   M. Heck, S. Nolte, A. Tünnermann, R. Vallée, and M. Bernier, "Femtosecond-written long-period gratings in fluoride fibers," *Opt. Lett.*, vol. 43, no. 9, p. 1994, May 2018, doi: 10.1364/OL.43.001994.

[77]   G. Bharathan, R. I. Woodward, M. Ams, D. D. Hudson, S. D. Jackson, and A. Fuerbach, "Direct inscription of Bragg gratings into coated fluoride fibers for widely tunable and robust mid-infrared lasers," *Opt. Express*, vol. 25, no. 24, p. 30013, Nov. 2017, doi: 10.1364/OE.25.030013.

[78]   F. Anelli *et al.*, "Mid-infrared interferometry with non-adiabatic tapered ZBLAN optical fiber," *Opt. Express*, vol. 32, no. 11, p. 18944, May 2024, doi: 10.1364/OE.521239.

[79]   K. Goya, Y. Koyama, Y. Nishijima, S. Tokita, R. Yasuhara, and H. Uehara, "A fluoride fiber optics in-line sensor for mid-IR spectroscopy based on

a side-polished structure," *Sens. Actuators B Chem.*, vol. 351, p. 130904, Jan. 2022, doi: 10.1016/j.snb.2021.130904.

[80]   J. P. Koplow, S. W. Moore, and D. A. V. Kliner, "A new method for side pumping of double-clad fiber sources," *IEEE J. Quantum Electron.*, vol. 39, no. 4, pp. 529–540, Apr. 2003, doi: 10.1109/JQE.2003.809336.

[81]   A. Kosterin, V. Temyanko, M. Fallahi, and M. Mansuripur, "Tapered fiber bundles for combining high-power diode lasers," *Appl. Opt.*, vol. 43, no. 19, p. 3893, Jul. 2004, doi: 10.1364/AO.43.003893.

[82]   C. Jauregui, S. Böhme, G. Wenetiadis, J. Limpert, and A. Tünnermann, "Side-pump combiner for all-fiber monolithic fiber lasers and amplifiers," *J. Opt. Soc. Am. B*, vol. 27, no. 5, p. 1011, May 2010, doi: 10.1364/JOSAB.27.001011.

[83]   T. Theeg, H. Sayinc, J. Neumann, L. Overmeyer, and D. Kracht, "Pump and signal combiner for bi-directional pumping of all-fiber lasers and amplifiers," *Opt. Express*, vol. 20, no. 27, p. 28125, Dec. 2012, doi: 10.1364/OE.20.028125.

[84]   T. A. Birks, I. Gris-Sánchez, S. Yerolatsitis, S. G. Leon-Saval, and R. R. Thomson, "The photonic lantern," *Adv. Opt. Photonics*, vol. 7, no. 2, p. 107, Jun. 2015, doi: 10.1364/AOP.7.000107.

[85]   P. M. Krummrich and S. Akhtari, "Selection of energy optimized pump concepts for multi core and multi mode erbium doped fiber amplifiers," *Opt. Express*, vol. 22, no. 24, p. 30267, Dec. 2014, doi: 10.1364/OE.22.030267.

[86]   S. G. Leon-Saval, A. Argyros, and J. Bland-Hawthorn, "Photonic lanterns: a study of light propagation in multimode to single-mode converters," *Opt. Express*, vol. 18, no. 8, p. 8430, Apr. 2010, doi: 10.1364/OE.18.008430.

[87]   P. Baer, P. Cebeci, M. Giesberts, and O. Fitzau, "Design and fabrication of a fused 7×1 35/50 μm into 125/250 μm fiber combiner," *OSA Contin.*, vol. 2, no. 4, p. 1106, Apr. 2019, doi: 10.1364/OSAC.2.001106.

[88]   F. Min, L. Zhixian, W. Zefeng, C. Zilun, and X. Xiaojun, "Research on a 4×1 fiber signal combiner with high beam quality at a power level of 12kW," *Opt. Express*, vol. 29, no. 17, p. 26658, Aug. 2021, doi: 10.1364/OE.433047.

[89] Y. Liu *et al.*, "5-kW-Level Bi-Directional High-Efficiency Pump and Signal Combiner With Negligible Beam Quality Degradation," *IEEE Photonics J.*, vol. 14, no. 1, pp. 1–6, Feb. 2022, doi: 10.1109/JPHOT.2021.3140004.

[90] N. K. Fontaine, R. Ryf, J. Bland-Hawthorn, and S. G. Leon-Saval, "Geometric requirements for photonic lanterns in space division multiplexing," *Opt. Express*, vol. 20, no. 24, p. 27123, Nov. 2012, doi: 10.1364/OE.20.027123.

[91] T. Theeg, H. Sayinc, J. Neumann, L. Overmeyer, and D. Kracht, "Side pumping scheme for all-fiber counter-pumping of high power single-frequency fiber amplifiers," in *2013 Conference on Lasers & Electro-Optics Europe & International Quantum Electronics Conference CLEO EUROPE/IQEC*, Munich, Germany: IEEE, May 2013, pp. 1–1. doi: 10.1109/CLEOE-IQEC.2013.6801294.

[92] M. Rezaei and M. Rochette, "All-chalcogenide ring fiber laser," *Opt. Fiber Technol.*, vol. 71, p. 102900, Jul. 2022, doi: 10.1016/j.yofte.2022.102900.

[93] I. Tugendhaft, "Directional multimode fiber couplers in the mid-infrared," *Opt. Eng.*, vol. 34, no. 10, p. 2846, Oct. 1995, doi: 10.1117/12.210769.

[94] M. Rezaei, M. H. M. Shamim, M. El Amraoui, Y. Messaddeq, and M. Rochette, "Nonlinear chalcogenide optical fiber couplers," *Opt. Express*, vol. 30, no. 12, p. 20288, Jun. 2022, doi: 10.1364/OE.458767.

[95] G. Stevens and T. Woodbridge, "Mid-IR fused fiber couplers," presented at the SPIE LASE, A. L. Glebov and P. O. Leisher, Eds., San Francisco, California, United States, Apr. 2016, p. 973007. doi: 10.1117/12.2203450.

[96] A. Annunziato *et al.*, "Single-mode fluoroindate coupler for mid-IR applications," in *Fiber Lasers and Glass Photonics: Materials through Applications IV*, S. Taccheo, M. R. Cicconi, and M. L. Jäger, Eds., Strasbourg, France: SPIE, Jun. 2024, p. 29. doi: 10.1117/12.3017514.

[97] F. Anelli *et al.*, "Multimode Fluoroindate Optical Fiber Coupler," in *2023 Conference on Lasers and Electro-Optics Europe & European Quantum Electronics Conference (CLEO/Europe-EQEC)*, Munich, Germany: IEEE, Jun. 2023, pp. 01–01. doi: 10.1109/CLEO/Europe-EQEC57999.2023.10232700.

[98] J. M. P. Coelho, M. C. Nespereira, M. Abreu, and J. M. Rebordão, "Modeling refractive index change in writing long-period fiber gratings using mid-

infrared laser radiation," *Photonic Sens.*, vol. 3, no. 1, pp. 67–73, Mar. 2013, doi: 10.1007/s13320-012-0084-1.

[99]   G. Rego, P. V. S. Marques, J. L. Santos, and H. M. Salgado, "Arc-Induced Long-Period Gratings," *Fiber Integr. Opt.*, vol. 24, no. 3–4, pp. 245–259, May 2005, doi: 10.1080/01468030590922975.

[100]   A. M. Vengsarkar, P. J. Lemaire, J. B. Judkins, V. Bhatia, T. Erdogan, and J. E. Sipe, "Long-period fiber gratings as band-rejection filters," *J. Light. Technol.*, vol. 14, no. 1, pp. 58–65, Jan. 1996, doi: 10.1109/50.476137.

[101]   I. K. Hwang, S. H. Yun, and B. Y. Kim, "Long-period fiber gratings based on periodic microbends," *Opt. Lett.*, vol. 24, no. 18, p. 1263, Sep. 1999, doi: 10.1364/OL.24.001263.

[102]   W. J. Bock, J. Chen, P. Mikulic, T. Eftimov, and M. Korwin-Pawlowski, "Pressure sensing using periodically tapered long-period gratings written in photonic crystal fibres," *Meas. Sci. Technol.*, vol. 18, no. 10, pp. 3098–3102, Oct. 2007, doi: 10.1088/0957-0233/18/10/S08.

[103]   C. E. Chryssou, "Gain-equalizing filters for wavelength division multiplexing optical communication systems: a comparison of notch and long-period grating filters for integrated optoelectronics," *Opt. Commun.*, vol. 184, no. 5–6, pp. 375–384, Oct. 2000, doi: 10.1016/S0030-4018(00)00956-1.

[104]   I. Navruz and A. Altuncu, "Optimization of Phase Shifted Long-Period Fiber Gratings for Multiband Rejection Filters," *J. Light. Technol.*, vol. 26, no. 14, pp. 2155–2161, Jul. 2008, doi: 10.1109/JLT.2008.922297.

[105]   B. Lee, "Review of the present status of optical fiber sensors," *Opt. Fiber Technol.*, vol. 9, no. 2, pp. 57–79, Apr. 2003, doi: 10.1016/S1068-5200(02)00527-8.

[106]   H. Tsuda and K. Urabe, "Characterization of Long-period Grating Refractive Index Sensors and Their Applications," *Sensors*, vol. 9, no. 6, pp. 4559–4571, Jun. 2009, doi: 10.3390/s90604559.

[107]   I. Navruz, F. Ari, M. Bilsel, and Z. A. AL-Mashhadani, "Enhancing refractive index sensitivity using micro-tapered long-period fiber grating inscribed in biconical tapered fiber," *Opt. Fiber Technol.*, vol. 45, pp. 201–207, Nov. 2018, doi: 10.1016/j.yofte.2018.07.018.

[108]   Y. Wang, "Review of long period fiber gratings written by CO2 laser," *J. Appl. Phys.*, vol. 108, no. 8, p. 081101, Oct. 2010, doi: 10.1063/1.3493111.

[109]   G. Yin, J. Tang, C. Liao, and Y. Wang, "Automatic arc discharge technology for inscribing long period fiber gratings," *Appl. Opt.*, vol. 55, no. 14, p. 3873, May 2016, doi: 10.1364/AO.55.003873.

[110]   L.-Y. Shao, J. Zhao, X. Dong, H. Y. Tam, C. Lu, and S. He, "Long-period grating fabricated by periodically tapering standard single-mode fiber," *Appl. Opt.*, vol. 47, no. 10, p. 1549, Apr. 2008, doi: 10.1364/AO.47.001549.

[111]   W. Yang *et al.*, "A phase-shifted long period fiber grating based on filament heating method for simultaneous measurement of strain and temperature," *J. Opt.*, vol. 17, no. 7, p. 075801, Jul. 2015, doi: 10.1088/2040-8978/17/7/075801.

[112]   D. D. Davis, T. K. Gaylord, E. N. Glytsis, S. G. Kosinski, S. C. Mettler, and A. M. Vengsarkar, "Long-period fibre grating fabrication with focused CO2 laser pulses," *Electron. Lett.*, vol. 34, no. 3, p. 302, 1998, doi: 10.1049/el:19980239.

[113]   Y.-P. Wang, D. N. Wang, W. Jin, Y.-J. Rao, and G.-D. Peng, "Asymmetric long period fiber gratings fabricated by use of CO2 laser to carve periodic grooves on the optical fiber," *Appl. Phys. Lett.*, vol. 89, no. 15, p. 151105, Oct. 2006, doi: 10.1063/1.2360253.

[114]   Min-Seok Yoon, Sangoh Park, and Young-Geun Han, "Simultaneous Measurement of Strain and Temperature by Using a Micro-Tapered Fiber Grating," *J. Light. Technol.*, vol. 30, no. 8, pp. 1156–1160, Apr. 2012, doi: 10.1109/JLT.2011.2170552.

[115]   Y. Zhao, L. Cai, and H.-F. Hu, "Fiber-Optic Refractive Index Sensor Based on Multi-Tapered SMS Fiber Structure," *IEEE Sens. J.*, vol. 15, no. 11, pp. 6348–6353, Nov. 2015, doi: 10.1109/JSEN.2015.2458893.

[116]   P. Wang *et al.*, "Enhanced Refractometer Based on Periodically Tapered Small Core Singlemode Fiber," *IEEE Sens. J.*, vol. 13, no. 1, pp. 180–185, Jan. 2013, doi: 10.1109/JSEN.2012.2216865.

[117]   G. Rego, O. Okhotnikov, E. Dianov, and V. Sulimov, "High-temperature stability of long-period fiber gratings produced using an electric arc," *J. Light. Technol.*, vol. 19, no. 10, pp. 1574–1579, Oct. 2001, doi: 10.1109/50.956145.

[118]   G. Humbert and A. Malki, "Characterizations at very high temperature of electric arc-induced long-period fiber gratings," *Opt. Commun.*, vol. 208, no. 4–6, pp. 329–335, Jul. 2002, doi: 10.1016/S0030-4018(02)01632-2.

[119]   A. D. Yablon *et al.*, "Refractive index perturbations in optical fibers resulting from frozen-in viscoelasticity," *Appl. Phys. Lett.*, vol. 84, no. 1, pp. 19–21, Jan. 2004, doi: 10.1063/1.1638883.

[120]   W. J. Bock, J. Chen, P. Mikulic, and T. Eftimov, "A Novel Fiber-Optic Tapered Long-Period Grating Sensor for Pressure Monitoring," *IEEE Trans. Instrum. Meas.*, vol. 56, no. 4, pp. 1176–1180, Aug. 2007, doi: 10.1109/TIM.2007.899904.

[121]   M. Heck, J.-C. Gauthier, A. Tünnermann, R. Vallée, S. Nolte, and M. Bernier, "Long period fiber gratings for the mitigation of parasitic laser effects in mid-infrared fiber amplifiers," *Opt. Express*, vol. 27, no. 15, p. 21347, Jul. 2019, doi: 10.1364/OE.27.021347.

[122]   H. Lu, R. Adams, M. Saad, P. Orsini, R. Burga, and L. R. Chen, "Mechanically induced long period gratings in ZBLAN fibers," in *2011 ICO International Conference on Information Photonics*, Ottawa, ON, Canada: IEEE, May 2011, pp. 1–2. doi: 10.1109/ICO-IP.2011.5953784.

[123]   P. Lu, L. Men, K. Sooley, and Q. Chen, "Tapered fiber Mach–Zehnder interferometer for simultaneous measurement of refractive index and temperature," *Appl. Phys. Lett.*, vol. 94, no. 13, p. 131110, Mar. 2009, doi: 10.1063/1.3115029.

[124]   W. Zhang *et al.*, "Advances in Tapered Optical Fiber Sensor Structures: From Conventional to Novel and Emerging," *Biosensors*, vol. 13, no. 6, p. 644, Jun. 2023, doi: 10.3390/bios13060644.

[125]   X. Fu *et al.*, "A temperature sensor based on the splicing of a core offset multi-mode fiber with two single mode fiber," *Optoelectron. Lett.*, vol. 11, no. 6, pp. 434–437, Nov. 2015, doi: 10.1007/s11801-015-5155-2.

[126]   T. Zhou, Y. Zhang, B. Han, A. Zhang, and D. Fu, "Low cost non-adia-batic tapered fiber for high-sensitive temperature sensing," *Opt. Fiber Technol.*, vol. 45, pp. 53–57, Nov. 2018, doi: 10.1016/j.yofte.2018.06.004.

[127]   R. Yang *et al.*, "S-Tapered Fiber Sensors for Highly Sensitive Measurement of Refractive Index and Axial Strain," *J. Light. Technol.*, vol. 30, no. 19, pp. 3126–3132, Oct. 2012, doi: 10.1109/JLT.2012.2210997.

[128]   M. Lakomski, B. Guzowski, and A. Wozniak, "Fabrication of ultra-long tapered optical fibers," *Microelectron. Eng.*, vol. 221, p. 111193, Jan. 2020, doi: 10.1016/j.mee.2019.111193.

[129]   N. A. Razak, B. A. Hamida, N. Irawati, and M. H. Habaebi, "Fabricate Optical Microfiber by Using Flame Brushing Technique and Coated with Polymer Polyaniline for Sensing Application," *IOP Conf. Ser. Mater. Sci. Eng.*, vol. 210, p. 012041, Jun. 2017, doi: 10.1088/1757-899X/210/1/012041.

[130]   H. Liu *et al.*, "Relative Humidity Sensor Based on S-Taper Fiber Coated With SiO_2 Nanoparticles," *IEEE Sens. J.*, vol. 15, no. 6, pp. 3424–3428, Jun. 2015, doi: 10.1109/JSEN.2015.2389519.

[131]   R. Yang, Y.-S. Yu, Y. Xue, C. Chen, Q.-D. Chen, and H.-B. Sun, "Single S-tapered fiber Mach–Zehnder interferometers," *Opt. Lett.*, vol. 36, no. 23, p. 4482, Dec. 2011, doi: 10.1364/OL.36.004482.

[132]   F. Shi, J. Wang, Y. Zhang, Y. Xia, and L. Zhao, "Refractive Index Sensor Based on S-Tapered Photonic Crystal Fiber," *IEEE Photonics Technol. Lett.*, vol. 25, no. 4, pp. 344–347, Feb. 2013, doi: 10.1109/LPT.2013.2238623.

[133]   J. Li *et al.*, "Long-Period Fiber Grating Cascaded to an S Fiber Taper for Simultaneous Measurement of Temperature and Refractive Index," *IEEE Photonics Technol. Lett.*, vol. 25, no. 9, pp. 888–891, May 2013, doi: 10.1109/LPT.2013.2255035.

[134]   S.-C. Yan, Y. Zhao, M.-Q. Chen, and Q. Liu, "Optical fiber strain sensor with double S-tapers," *Instrum. Sci. Technol.*, vol. 49, no. 3, pp. 313–326, May 2021, doi: 10.1080/10739149.2020.1840387.

[135]   W.-M. Zhao and Q. Wang, "A high sensitivity refractive index sensor based on three-level gradient structure S-tapered fiber mode-mode

interferometer," *Measurement*, vol. 139, pp. 49–60, Jun. 2019, doi: 10.1016/j.measurement.2019.03.018.

[136] Y. Zhao *et al.*, "Relative humidity sensor of S fiber taper based on graphene oxide film," *Opt. Commun.*, vol. 450, pp. 147–154, Nov. 2019, doi: 10.1016/j.optcom.2019.05.072.

[137] Z. Lv, P. Niu, J. Jiang, S. Wang, Y. Liu, and T. Liu, "Reflective SFT-FBG Hybrid Micro-Probe for Simultaneous Measurement of Relative Humidity and Temperature," *IEEE Photonics J.*, vol. 14, no. 1, pp. 1–6, Feb. 2022, doi: 10.1109/JPHOT.2021.3136677.

[138] X. Hu, H. Zhang, W. Lin, T. Liu, and B. Liu, "Light-Controlled Asymmetric Dual-S-Taper Fiber Interferometer Integrated With Ethyl Orange Solution Under 473 nm Laser Illumination," *IEEE Sens. J.*, vol. 21, no. 21, pp. 24149–24156, Nov. 2021, doi: 10.1109/JSEN.2021.3113567.

[139] M. Deng, D. Liu, and D. Li, "Magnetic field sensor based on asymmetric optical fiber taper and magnetic fluid," *Sens. Actuators Phys.*, vol. 211, pp. 55–59, May 2014, doi: 10.1016/j.sna.2014.02.014.

[140] S. Duan *et al.*, "Hydrophobin HGFI–based fibre-optic biosensor for detection of antigen–antibody interaction," *Nanophotonics*, vol. 9, no. 1, pp. 177–186, Jan. 2020, doi: 10.1515/nanoph-2019-0370.

[141] L. Zhang, F. Guan, L. Zhang, and Y. Jiang, "Next generation mid-infrared fiber: fluoroindate glass fiber," *Opt. Mater. Express*, vol. 12, no. 4, p. 1683, Apr. 2022, doi: 10.1364/OME.454418.

[142] Q. Luo *et al.*, "Remote sensing of pollutants using femtosecond laser pulse fluorescence spectroscopy," *Appl. Phys. B*, vol. 82, no. 1, pp. 105–109, Jan. 2006, doi: 10.1007/s00340-005-2008-x.

[143] K. Wang, D.-W. Sun, and H. Pu, "Emerging non-destructive terahertz spectroscopic imaging technique: Principle and applications in the agri-food industry," *Trends Food Sci. Technol.*, vol. 67, pp. 93–105, Sep. 2017, doi: 10.1016/j.tifs.2017.06.001.

[144] K. Sharma, M. Srivastava, D. Venkitesh, and S. Bhattacharya, "Design and modeling of tunable mid-IR fiber laser using Thulium doped fibers," in

International Conference on Fibre Optics and Photonics, Chennai: OSA, 2012, p. T3C.4. doi: 10.1364/PHOTONICS.2012.T3C.4.

[145] L. G. Holmen *et al.*, "Tunable holmium-doped fiber laser with multiwatt operation from 2025 nm to 2200 nm," *Opt. Lett.*, vol. 44, no. 17, p. 4131, Sep. 2019, doi: 10.1364/OL.44.004131.

[146] M. R. Majewski, R. I. Woodward, and S. D. Jackson, "Dysprosium-doped ZBLAN fiber laser tunable from 28 μm to 34 μm, pumped at 17 μm," *Opt. Lett.*, vol. 43, no. 5, p. 971, Mar. 2018, doi: 10.1364/OL.43.000971.

[147] V. Fortin, F. Jobin, M. Larose, M. Bernier, and R. Vallée, "10-W-level monolithic dysprosium-doped fiber laser at 324 μm," *Opt. Lett.*, vol. 44, no. 3, p. 491, Feb. 2019, doi: 10.1364/OL.44.000491.

[148] O. Henderson-Sapir, S. D. Jackson, and D. J. Ottaway, "Versatile and widely tunable mid-infrared erbium doped ZBLAN fiber laser," *Opt. Lett.*, vol. 41, no. 7, p. 1676, Apr. 2016, doi: 10.1364/OL.41.001676.

[149] J. Zhang *et al.*, "33.8 W Mid-infrared 2.8 μm Er-doped fiber laser with high optical efficiency," *Results Phys.*, vol. 55, p. 107172, Dec. 2023, doi: 10.1016/j.rinp.2023.107172.

[150] Y. Ososkov, J. Lee, T. T. Fernandez, A. Fuerbach, and S. D. Jackson, "High-efficiency fluoroindate glass fiber laser," *Opt. Lett.*, vol. 48, no. 10, p. 2664, May 2023, doi: 10.1364/OL.486318.

[151] R. Wang *et al.*, "Watt-level fluoroindate based glass fibre laser operating around 3 μm," *J. Lumin.*, vol. 256, p. 119626, Apr. 2023, doi: 10.1016/j.jlumin.2022.119626.

[152] S. Yonezawa, S. Nishibu, M. Leblanc, and M. Takashima, "Preparation and properties of rare-earth containing oxide fluoride glasses," *J. Fluor. Chem.*, vol. 128, no. 4, pp. 438–447, Apr. 2007, doi: 10.1016/j.jfluchem.2006.12.002.

[153] F. Maes *et al.*, "Room-temperature fiber laser at 392 μm," *Optica*, vol. 5, no. 7, p. 761, Jul. 2018, doi: 10.1364/OPTICA.5.000761.

[154] F. Zhou, J. Li, H. Luo, F. Quellette, and Y. Liu, "Numerical Analysis of 3.92 μm Dual-Wavelength Pumped Heavily-Holmium-Doped Fluoroindate Fiber Lasers," *J. Light. Technol.*, vol. 39, no. 2, pp. 633–645, Jan. 2021, doi: 10.1109/JLT.2020.3033335.

[155] A. M. Loconsole, M. C. Falconi, V. Portosi, and F. Prudenzano, "Numerical Design of a Gain-Switched Pulsed Laser at 3.92 μm Wavelength Based on a Ho^{3+}-Doped Fluoroindate Fiber," *J. Light. Technol.*, vol. 39, no. 10, pp. 3276–3283, May 2021, doi: 10.1109/JLT.2021.3064764.

[156] R. M. Percival, S. F. Carter, D. Szebesta, S. T. Davey, and W. A. Stallard, "Thulium-doped monomode fluoride fibre laser broadly tunable from 2.25 to 2.5 μm," *Electron. Lett.*, vol. 27, no. 21, p. 1912, 1991, doi: 10.1049/el:19911187.

[157] E. Poppe, B. Srinivasan, and R. K. Jain, "980 nm diode-pumped continuous wave mid-IR (2.7 [micro sign]m) fibre laser," *Electron. Lett.*, vol. 34, no. 24, p. 2331, 1998, doi: 10.1049/el:19981582.

[158] S. Crawford, D. D. Hudson, and S. D. Jackson, "High-Power Broadly Tunable 3- $\mu\hbox{m}$ Fiber Laser for the Measurement of Optical Fiber Loss," *IEEE Photonics J.*, vol. 7, no. 3, pp. 1–9, Jun. 2015, doi: 10.1109/JPHOT.2015.2430012.

[159] K. S. Wu, D. Ottaway, J. Munch, D. G. Lancaster, S. Bennetts, and S. D. Jackson, "Gain-switched holmium-doped fibre laser," *Opt. Express*, vol. 17, no. 23, p. 20872, Nov. 2009, doi: 10.1364/OE.17.020872.

[160] J. Li, Y. Yang, D. D. Hudson, Y. Liu, and S. D. Jackson, "A tunable *Q*-switched Ho^{3+}-doped fluoride fiber laser," *Laser Phys. Lett.*, vol. 10, no. 4, p. 045107, Apr. 2013, doi: 10.1088/1612-2011/10/4/045107.

[161] A. M. Loconsole, V. V. Francione, A. Annunziato, F. Anelli, and F. Prudenzano, "Design of a High Performance Mid-IR Fiber Laser Based on Pr^{3+}-Doped Fluoroindate Glass," *J. Light. Technol.*, vol. 42, no. 7, pp. 2488–2493, Apr. 2024, doi: 10.1109/JLT.2023.3338139.

[162] W.-P. Huang, "Coupled-mode theory for optical waveguides: an overview," *J. Opt. Soc. Am. A*, vol. 11, no. 3, p. 963, Mar. 1994, doi: 10.1364/JOSAA.11.000963.

[163] G. P. Agrawal, *Fiber-optic communication systems*, 3rd ed. in Wiley series in microwave and optical engineering. New York: Wiley-Interscience, 2002.

[164] H. Kogelnik, "Theory of Optical Waveguides," in *Guided-Wave Optoelectronics*, vol. 26, T. Tamir, Ed., in Springer Series in Electronics and

Photonics, vol. 26. , Berlin, Heidelberg: Springer Berlin Heidelberg, 1988, pp. 7–88. doi: 10.1007/978-3-642-97074-0_2.

[165] H. Kogelnik, "Theory of Dielectric Waveguides," in *Integrated Optics*, vol. 7, T. Tamir, Ed., in Topics in Applied Physics, vol. 7. , Berlin, Heidelberg: Springer Berlin Heidelberg, 1975, pp. 13–81. doi: 10.1007/978-3-662-43208-2_2.

[166] T. Erdogan and J. E. Sipe, "Tilted fiber phase gratings," *J. Opt. Soc. Am. A*, vol. 13, no. 2, p. 296, Feb. 1996, doi: 10.1364/JOSAA.13.000296.

[167] T. Erdogan, "Fiber grating spectra," *J. Light. Technol.*, vol. 15, no. 8, pp. 1277–1294, Aug. 1997, doi: 10.1109/50.618322.

[168] L. Mescia, "Design of long-period gratings in cladding-pumped micro-structured optical fiber," *J. Opt. Soc. Am. B*, vol. 25, no. 11, p. 1833, Nov. 2008, doi: 10.1364/JOSAB.25.001833.

[169] T. Erdogan, "Cladding-mode resonances in short- and long-period fiber grating filters," *J. Opt. Soc. Am. A*, vol. 14, no. 8, p. 1760, Aug. 1997, doi: 10.1364/JOSAA.14.001760.

[170] W. Scarcia, G. Palma, M. Falconi, F. De Leonardis, V. Passaro, and F. Prudenzano, "Electromagnetic Modelling of Fiber Sensors for Low-Cost and High Sensitivity Temperature Monitoring," *Sensors*, vol. 15, no. 12, pp. 29855–29870, Nov. 2015, doi: 10.3390/s151229770.

[171] H. Alemohammad, "Opto-Mechanical Modeling of Fiber Bragg Grating Sensors," in *Opto-Mechanical Fiber Optic Sensors*, Elsevier, 2018, pp. 1–26. doi: 10.1016/B978-0-12-803131-5.00001-5.

[172] J. F. Nye, *Physical properties of crystals: their representation by tensors and matrices*, 1st published in pbk. with corrections, 1984. Oxford [Oxfordshire] : New York: Clarendon Press ; Oxford University Press, 1984.

[173] K.-S. Kim, Y. Ismail, and G. S. Springer, "Measurements of Strain and Temperature with Embedded Intrinsic Fabry-Perot Optical Fiber Sensors," *J. Compos. Mater.*, vol. 27, no. 17, pp. 1663–1677, Dec. 1993, doi: 10.1177/002199839302701702.

[174] K.-S. Kim, L. Kollár, and G. S. Springer, "A Model of Embedded Fiber Optic Fabry-Perot Temperature and Strain Sensors," *J. Compos. Mater.*, vol. 27, no. 17, pp. 1618–1662, Dec. 1993, doi: 10.1177/002199839302701701.

[175] A. Taghipour, A. Rostami, M. Bahrami, H. Baghban, and M. Dolatyari, "Comparative study between LPFG- and FBG-based bending sensors," *Opt. Commun.*, vol. 312, pp. 99–105, Feb. 2014, doi: 10.1016/j.optcom.2013.09.020.

[176] Y. Cardona Maya, N. Gómez Cardona, and P. I. Torres Trujillo, "Low cost heat-and-pull rig for manufacturing adiabatic optical fiber tapers," *Rev. Fac. Ing. Univ. Antioquia*, no. 70, pp. 167–172, Feb. 2014, doi: 10.17533/udea.redin.14820.

[177] T. A. Birks and Y. W. Li, "The shape of fiber tapers," *J. Light. Technol.*, vol. 10, no. 4, pp. 432–438, Apr. 1992, doi: 10.1109/50.134196.

[178] R. P. Kenny, T. A. Birks, and K. P. Oakley, "Control of optical fibre taper shape," *Electron. Lett.*, vol. 27, no. 18, p. 1654, 1991, doi: 10.1049/el:19911034.

[179] Y. Shestopalov, Y. Smirnov, and E. Smolkin, *Optical Waveguide Theory: Mathematical Models, Spectral Theory and Numerical Analysis*, vol. 237. in Springer Series in Optical Sciences, vol. 237. Singapore: Springer Singapore, 2022. doi: 10.1007/978-981-19-0584-1.

[180] J. D. Love, W. M. Henry, W. J. Stewart, R. J. Black, S. Lacroix, and F. Gonthier, "Tapered single-mode fibres and devices. Part 1: Adiabaticity criteria," *IEE Proc. J Optoelectron.*, vol. 138, no. 5, p. 343, 1991, doi: 10.1049/ip-j.1991.0060.

[181] M. Rezaei and M. Rochette, "All-chalcogenide single-mode optical fiber couplers," *Opt. Lett.*, vol. 44, no. 21, p. 5266, Nov. 2019, doi: 10.1364/OL.44.005266.

[182] I. Yokohama, K. Chida, and J. Noda, "Low excess loss conditions of polarization-maintaining fiber couplers," *Appl. Opt.*, vol. 27, no. 23, p. 4807, Dec. 1988, doi: 10.1364/AO.27.004807.

[183] Y. Lu *et al.*, "High-Power Orbital Angular Momentum Beam Generation Using Adaptive Control System Based on Mode Selective Photonic Lantern," *J. Light. Technol.*, vol. 41, no. 17, pp. 5607–5613, Sep. 2023, doi: 10.1109/JLT.2023.3266255.

[184] S. G. Leon-Saval, T. A. Birks, J. Bland-Hawthorn, and M. Englund, "Multimode fiber devices with single-mode performance," *Opt. Lett.*, vol. 30, no. 19, p. 2545, Oct. 2005, doi: 10.1364/OL.30.002545.

[185] J. Bland-Hawthorn *et al.*, "A complex multi-notch astronomical filter to suppress the bright infrared sky," *Nat. Commun.*, vol. 2, no. 1, p. 581, Dec. 2011, doi: 10.1038/ncomms1584.

[186] S. G. Leon-Saval, N. K. Fontaine, and R. Amezcua-Correa, "Photonic lantern as mode multiplexer for multimode optical communications," *Opt. Fiber Technol.*, vol. 35, pp. 46–55, Feb. 2017, doi: 10.1016/j.yofte.2016.08.005.

[187] B. Huang *et al.*, "All-fiber mode-group-selective photonic lantern using graded-index multimode fibers," *Opt. Express*, vol. 23, no. 1, p. 224, Jan. 2015, doi: 10.1364/OE.23.000224.

[188] S. G. Leon-Saval, N. K. Fontaine, J. R. Salazar-Gil, B. Ercan, R. Ryf, and J. Bland-Hawthorn, "Mode-selective photonic lanterns for space-division multiplexing," *Opt. Express*, vol. 22, no. 1, p. 1036, Jan. 2014, doi: 10.1364/OE.22.001036.

[189] S. Sunder and A. Sharma, "Engineering Adiabaticity for Efficient Design of Photonic Lanterns," *IEEE Photonics J.*, vol. 13, no. 2, pp. 1–13, Apr. 2021, doi: 10.1109/JPHOT.2021.3058361.

[190] S. G. Leon-Saval, A. Argyros, and J. Bland-Hawthorn, "Photonic lanterns," *Nanophotonics*, vol. 2, no. 5–6, pp. 429–440, Dec. 2013, doi: 10.1515/nanoph-2013-0035.

[191] C. H. Betters, J. Bland-Hawthorn, S. Sukkarieh, I. Gris-Sanchez, and S. G. Leon-Saval, "A Multi-Core Fibre Photonic Lantern-Based Spectrograph for Raman Spectroscopy," *IEEE Photonics Technol. Lett.*, vol. 32, no. 7, pp. 395–398, Apr. 2020, doi: 10.1109/LPT.2020.2976599.

[192] D. H. McMahon, "Efficiency limitations imposed by thermodynamics on optical coupling in fiber-optic data links*," *J. Opt. Soc. Am.*, vol. 65, no. 12, p. 1479, Dec. 1975, doi: 10.1364/JOSA.65.001479.

[193] M. I. Zibaii, H. Latifi, M. Karami, M. Gholami, S. M. Hosseini, and M. H. Ghezelayagh, "Non-adiabatic tapered optical fiber sensor for measuring the interaction between α-amino acids in aqueous carbohydrate solution," *Meas. Sci.*

Technol., vol. 21, no. 10, p. 105801, Oct. 2010, doi: 10.1088/0957-0233/21/10/105801.

[194] L. Xiao *et al.*, "Development and stability analysis of an S-tapered optical fiber-based sensor structure," *Appl. Opt.*, vol. 62, no. 16, p. E37, Jun. 2023, doi: 10.1364/AO.483335.

[195] J. Jiang *et al.*, "S-Taper Fiber Based Moisture Sensing in Power Transformer Oil," *IEEE Trans. Instrum. Meas.*, vol. 72, pp. 1–8, 2023, doi: 10.1109/TIM.2023.3246474.

[196] H. Liu *et al.*, "Temperature-Insensitive Label-Free Sensors for Human IgG Based on S-Tapered Optical Fiber Sensors," *IEEE Access*, vol. 9, pp. 116286–116293, 2021, doi: 10.1109/ACCESS.2021.3106343.

[197] K. Tian, M. Zhang, G. Farrell, R. Wang, E. Lewis, and P. Wang, "Highly sensitive strain sensor based on composite interference established within S-tapered multimode fiber structure," *Opt. Express*, vol. 26, no. 26, p. 33982, Dec. 2018, doi: 10.1364/OE.26.033982.

[198] K. Kalli *et al.*, "Flat fibre and femtosecond laser technology as a novel photonic integration platform for optofluidic based biosensing devices and lab-on-chip applications: Current results and future perspectives," *Sens. Actuators B Chem.*, vol. 209, pp. 1030–1040, Mar. 2015, doi: 10.1016/j.snb.2014.12.003.

[199] G.-D. Peng, Ed., *Handbook of optical fibers*. in Springer reference. Singapore: Springer, 2019.

[200] T. Martynkien *et al.*, "Highly birefringent microstructured fibers with enhanced sensitivity to hydrostatic pressure," *Opt. Express*, vol. 18, no. 14, p. 15113, Jul. 2010, doi: 10.1364/OE.18.015113.

[201] T. Geernaert *et al.*, "Transversal Load Sensing With Fiber Bragg Gratings in Microstructured Optical Fibers," *IEEE Photonics Technol. Lett.*, vol. 21, no. 1, pp. 6–8, Jan. 2009, doi: 10.1109/LPT.2008.2007915.

[202] A. Annunziato, F. Anelli, J. Gates, C. Holmes, and F. Prudenzano, "Design of Polarization-Maintaining FBGs Using Polyimide Films to Improve Strain-Temperature Sensing in CFRP Laminates," *IEEE Photonics J.*, vol. 13, no. 2, pp. 1–15, Apr. 2021, doi: 10.1109/JPHOT.2021.3063172.

[203] Y. Okabe, S. Yashiro, T. Kosaka, and N. Takeda, "Detection of transverse cracks in CFRP composites using embedded fiber Bragg grating sensors," *Smart Mater. Struct.*, vol. 9, no. 6, pp. 832–838, Dec. 2000, doi: 10.1088/0964-1726/9/6/313.

[204] R. Potluri, "Mechanical properties evaluation of T800 carbon fiber reinforced hybrid composite embedded with silicon carbide microparticles: A micromechanical approach," *Multidiscip. Model. Mater. Struct.*, vol. 14, no. 3, pp. 589–608, Aug. 2018, doi: 10.1108/MMMS-09-2017-0106.

[205] M. Rodríguez, J. M. Molina-Aldareguía, C. González, and J. LLorca, "A methodology to measure the interface shear strength by means of the fiber push-in test," *Compos. Sci. Technol.*, vol. 72, no. 15, pp. 1924–1932, Oct. 2012, doi: 10.1016/j.compscitech.2012.08.011.

[206] L. St-Pierre, N. J. Martorell, and S. T. Pinho, "Stress redistribution around clusters of broken fibres in a composite," *Compos. Struct.*, vol. 168, pp. 226–233, May 2017, doi: 10.1016/j.compstruct.2017.01.084.

[207] H. R. Sørensen, J. Canning, J. Lægsgaard, K. Hansen, and P. Varming, "Liquid filling of photonic crystal fibres for grating writing," *Opt. Commun.*, vol. 270, no. 2, pp. 207–210, Feb. 2007, doi: 10.1016/j.optcom.2006.09.009.

[208] T. Geernaert *et al.*, "Bragg Grating Inscription in GeO -Doped Microstructured Optical Fibers," *J. Light. Technol.*, vol. 28, no. 10, pp. 1459–1467, May 2010, doi: 10.1109/JLT.2010.2043414.

[209] T. Mawatari and D. Nelson, "A multi-parameter Bragg grating fiber optic sensor and triaxial strain measurement," *Smart Mater. Struct.*, vol. 17, no. 3, p. 035033, Jun. 2008, doi: 10.1088/0964-1726/17/3/035033.

[210] C. Sonnenfeld *et al.*, "Microstructured optical fiber Bragg grating as an internal three-dimensional strain sensor for composite laminates," *Smart Mater. Struct.*, vol. 24, no. 5, p. 055003, May 2015, doi: 10.1088/0964-1726/24/5/055003.

[211] G. Luyckx *et al.*, "Three-dimensional strain and temperature monitoring of composite laminates," *Insight - Non-Destr. Test. Cond. Monit.*, vol. 49, no. 1, pp. 10–16, Jan. 2007, doi: 10.1784/insi.2007.49.1.10.

[212] C. Holmes, M. Godfrey, D. J. Bull, and J. Dulieu-Barton, "Real-time through-thickness and in-plane strain measurement in carbon fibre reinforced polymer composites using planar optical Bragg gratings," *Opt. Lasers Eng.*, vol. 133, p. 106111, Oct. 2020, doi: 10.1016/j.optlaseng.2020.106111.

[213] C. Liu, X. Yang, F. Laurell, and M. Fokine, "Fabrication of a widely tunable fiber Bragg grating filter using fused deposition modeling 3D printing," *Opt. Mater. Express*, vol. 9, no. 11, p. 4409, Nov. 2019, doi: 10.1364/OME.9.004409.

[214] J. Kong, X. Ouyang, A. Zhou, H. Yu, and L. Yuan, "Pure Directional Bending Measurement With a Fiber Bragg Grating at the Connection Joint of Eccentric-Core and Single-Mode Fibers," *J. Light. Technol.*, vol. 34, no. 14, pp. 3288–3292, Jul. 2016, doi: 10.1109/JLT.2016.2565540.

[215] M. Jang, J. S. Kim, S. H. Um, S. Yang, and J. Kim, "Ultra-high curvature sensors for multi-bend structures using fiber Bragg gratings," *Opt. Express*, vol. 27, no. 3, p. 2074, Feb. 2019, doi: 10.1364/OE.27.002074.

[216] H. Haus, W. Huang, S. Kawakami, and N. Whitaker, "Coupled-mode theory of optical waveguides," *J. Light. Technol.*, vol. 5, no. 1, pp. 16–23, 1987, doi: 10.1109/JLT.1987.1075416.

[217] C. Holmes, M. Godfrey, P. L. Mennea, S. Zahertar, and J. M. Dulieu-Barton, "Flexible photonics in low stiffness doped silica for use in fibre reinforced polymer composite materials," *Opt. Mater.*, vol. 134, p. 113133, Dec. 2022, doi: 10.1016/j.optmat.2022.113133.

[218] I. H. Malitson, "Interspecimen Comparison of the Refractive Index of Fused Silica*,†," *J. Opt. Soc. Am.*, vol. 55, no. 10, p. 1205, Oct. 1965, doi: 10.1364/JOSA.55.001205.

[219] F. Anelli, A. Annunziato, A. M. Loconsole, S. Venck, S. Cozic, and F. Prudenzano, "Mode-Group Selective Photonic Lantern based on Indium Fluoride Optical Fibers for Mid-Infrared," *J. Light. Technol.*, pp. 1–8, 2024, doi: 10.1109/JLT.2024.3450115.

[220] F. Gan, "Optical properties of fluoride glasses: a review," *J. Non-Cryst. Solids*, vol. 184, pp. 9–20, May 1995, doi: 10.1016/0022-3093(94)00592-3.

[221] X. Leng and S. S.-H. Yam, "Mode Interference in Non-Adiabatic Fiber Taper With a Long Uniform Region," *IEEE Photonics Technol. Lett.*, vol. 31, no. 18, pp. 1491–1494, Sep. 2019, doi: 10.1109/LPT.2019.2934343.

[222] Y. Liu and D. N. Wang, "Fiber In-Line Fabry-Perot Interferometer With Offset Splicing for Strain Measurement With Enhanced Sensitivity," *IEEE Photonics J.*, vol. 10, no. 1, pp. 1–8, Feb. 2018, doi: 10.1109/JPHOT.2017.2739198.

[223] H. He, Z. Jia, Y. Ohishi, W. Qin, and G. Qin, "Efficient ~4 µm emission from Pr $^{3+}$ /Yb $^{3+}$ co-doped fluoroindate glass," *Opt. Lett.*, vol. 46, no. 22, p. 5607, Nov. 2021, doi: 10.1364/OL.440635.

[224] D. Manzani, D. Pabœuf, S. J. L. Ribeiro, P. Goldner, and F. Bretenaker, "Orange emission in Pr3+-doped fluoroindate glasses," *Opt. Mater.*, vol. 35, no. 3, pp. 383–386, Jan. 2013, doi: 10.1016/j.optmat.2012.09.030.

[225] A. Remillieux *et al.*, "Upconversion mechanisms of a praseodymium-doped fluoride fibre amplifier," *J. Phys. Appl. Phys.*, vol. 29, no. 4, pp. 963–974, Apr. 1996, doi: 10.1088/0022-3727/29/4/004.

[226] L. Gomes and S. D. Jackson, "Spectroscopic properties of ytterbium, praseodymium-codoped fluorozirconate glass for laser emission at 36 µm," *J. Opt. Soc. Am. B*, vol. 30, no. 6, p. 1410, Jun. 2013, doi: 10.1364/JOSAB.30.001410.

[227] R. Pappalardo, "Calculated quantum yields for photon-cascade emission (PCE) for Pr3+ and Tm3+ in fluoride hosts," *J. Lumin.*, vol. 14, no. 3, pp. 159–193, Jan. 1976, doi: 10.1016/S0022-2313(76)90592-5.

[228] R. S. Quimby and B. Zheng, "New excited-state absorption measurement technique and application to Pr3+ doped fluorozirconate glass," *Appl. Phys. Lett.*, vol. 60, no. 9, pp. 1055–1057, Mar. 1992, doi: 10.1063/1.106442.

Acknowledgements